EXCLUSIVE RARE B DECAYS TO TWO LIGHT PSEUDOSCALAR MESONS.

A Dissertation

Presented to the Faculty of the Graduate School

of Cornell University

in Partial Fulfillment of the Requirements for the Degree of

Doctor of Philosophy

by

Petr Borisovich Gaidarev

August 1997

EXCLUSIVE RARE B DECAYS TO TWO LIGHT PSEUDOSCALAR MESONS.

Petr Borisovich Gaidarev, Ph.D.

Cornell University 1997

Using the data sample of 3.3×10^6 $B\bar{B}$ events taken with the CLEO II detector, we have searched for rare B decays into $K\pi$ and $\pi\pi$ final states. We have made the first observation of the decay $B^0 \to K^+\pi^-$ and measured its branching fraction to be $(1.5^{+0.5+0.1}_{-0.4-0.1} \pm 0.1) \times 10^{-5}$. We set 90% confidence level upper limits of 1.5×10^{-5} and 0.43×10^{-5} for $B^0 \to \pi^+\pi^-$ and $B^0 \to K^+K^-$ respectively.

We have also observed the decay $B^+ \to \pi^+K^0$. The measured branching fraction is $(2.3^{+1.1+0.3}_{-1.0-0.3} \pm 0.2) \times 10^{-5}$ and we set a 90% C.L. upper limit of 2.1×10^{-5} for the $B^+ \to K^+K^0$ decay mode.

We have found strong evidence for the decays $B^+ \to h^+\pi^0$, where h^+ stands for a charged kaon or pion. We have measured the combined branching fraction of $(1.6^{+0.6+0.3}_{-0.5-0.2} \pm 0.1) \times 10^{-5}$ and set 90% C.L. upper limits of 1.6×10^{-5} and 2.0×10^{-5} for $B^+ \to K^+\pi^0$ and $B^+ \to \pi^+\pi^0$ respectively.

We have searched for the decays $B^0 \to K^0\pi^0$ and $B^0 \to \pi^0\pi^0$ and set 90% C.L. upper limits of 4.1×10^{-5} and 0.93×10^{-5} respectively.

The importance of this class of decays for the studies of CP violation in B mesons is discussed, in particular their use to measure the angle γ of the unitarity triangle.

BIOGRAPHICAL SKETCH

Peter Gaidarev was born on October 11, 1965 in Novokuznetsk, midsize industrial town in West Siberia, Russia (then Soviet Union). He was mainly interested in chemistry in junior high school and with the help and encouragement from his high school teacher he eventually moved to the Science Magnet School, run by the Novosibirsk State University. There he quickly realized that he doesn't know much about math, physics and even chemistry. While catching up, it became clear that physics is much more interesting and he still thinks this is true.

In 1982 Peter became a student in the Physics Department of the Novosibirsk State University. His interests started to gravitate towards the High Energy Physics at this time and he was about to start his undergraduate research at the Budker Institute of Nuclear Physics, when the Soviet Army came knocking at his door. After spending two not so eventful years in the Soviet Army as a sergeant, he got back to his classes and research, graduating in June of 1989 with a Diploma in Physics. For the next three years Peter worked as a junior researcher in the Budker Institute, building the CsI calorimeter for the KEDR experiment.

In 1992 Peter was accepted into Cornell graduate school and moved to Ithaca, NY, where he still lives. He joined CLEO in 1993 and worked on the Silicon Vertex Detector and search for rare decays of the B meson, defending his thesis on July 25, 1997. He is going to do more or less the same for the next three years as a

Cornell Research Associate.

Peter is married to Tatyana Pyntikova, whom he met in 1986 in Novosibirsk and married in 1995 in Ithaca.

ACKNOWLEDGEMENTS

I would like to thank my advisor, Jim Alexander. He gave me all the freedom I could have, but I never felt abandoned or forgotten. Many thanks go to my committee members, Karl Berkelman, Kurt Gottfried, and Peter Lepage, who made my experience with graduate studies challenging but pleasant.

Special thanks to the Rare B group members: Karen Lingel, Frank Wüerthwein, Peter Kim, Jim Smith, Jim Fast, Chris Jones, Bill Ford, Ahren Sadoff and many others. Frank and Peter, discussions with you, whether in person or through videoconferencing, were as good as they get.

Thanks to my classmates at Cornell, especially Geoff, long time housemate, neighbor, and good friend. You helped me to get used to the life in the U.S., and I hope I gave something back.

I am indebted to everyone I worked with at Novosibirsk, especially to my undergraduate advisor, Simon Eidelman, who nudged me towards the High Energy physics, when I had my doubts. I learned a lot from Boris Shwartz, Alex Bondar, and Sasha Kuzmin. It was a great fun to hang out at the second floor of "pristroika" with Tanya(s), Volodya(s), Andrei, Misha, Valera, Kolya, Lenya, Vitya(s), Sasha, Sergei(s), Edik and everyone else.

My fascination with physics started in the high school and my teacher, Boris Khazin, was the main reason. Thanks for showing us that physics is not just a collection of formulas.

Tatyana, thanks for being who you are - loving and understanding wife. And I won't forget the flowers, champagne, and cute stuffed penguin you gave me right after the defense. And I don't know how to express my gratitude to Mom and Dad - thanks for supporting me in all my endeavors and believing in me.

TABLE OF CONTENTS

LIST OF TABLES

LIST OF FIGURES

CHAPTER 1

THEORY

1.1 Introduction

Through the experimental work done in the last hundred years or so, we now know that more than two hundred elementary particles exist. Some of them, like electron, neutrino, proton and neutron are found in great abundance, constituting the building blocks of the matter in the universe. Most of the remaining particles are much more elusive, living for a tiny fraction of a second and are found only in the cosmic rays or produced at the accelerators. According to the modern theory of particle physics, known as Standard Model [1], a rich spectrum of observed particles can be explained in terms of the truly fundamental building blocks:

$$\begin{array}{ccc} & leptons & \\ \begin{pmatrix} \nu_e \\ e \end{pmatrix} & \begin{pmatrix} \nu_\mu \\ \mu \end{pmatrix} & \begin{pmatrix} \nu_\tau \\ \tau \end{pmatrix} \end{array} \qquad \begin{array}{ccc} & quarks & \\ \begin{pmatrix} u \\ d \end{pmatrix} & \begin{pmatrix} c \\ s \end{pmatrix} & \begin{pmatrix} t \\ b \end{pmatrix} \end{array}$$

plus corresponding antiparticles.

While leptons can be easily observed in the lab, quarks are "confined" to the hadrons they form: baryons and mesons. Baryons contain 3 quarks, while mesons are made of quark and antiquark pair. The rich spectrum of observed hadrons is then explained by the combinations of the six basic quark "flavors".

It is worthwhile to note that fundamental fermions as listed above are quite naturally arranged into three families. While only the first family

$$\begin{pmatrix} \nu_e \\ e \end{pmatrix} \qquad \begin{pmatrix} u \\ d \end{pmatrix}$$

is needed to describe the ordinary matter our world is made of, the reason for the existence of extra families remains unknown.

The picture of the elementary particles world is not complete without the forces, or interactions, and gauge bosons, which are the "carriers" of the force.

Force	Gauge Boson
Gravity	???
Electromagnetic	γ
Strong	g_1, ..., g_8
Weak	Z^0, W^+, W^-

The most familiar force, gravitation, turns out to be not important in particle physics, since the masses of the particles are so small. Electromagnetic interaction, mediated by the photon(γ) involves particles carrying electric charge and is responsible for binding electrons and nuclei into atoms. The strong force holds together quarks inside hadrons. Each quark flavor comes in 3 different "colors", and you need 8 massless gluons $g_1 ... g_8$ to describe strong forces between quarks (leptons do not participate in strong interactions). Finally, the weak interaction is mediated by the $W^{\pm}$ and Z^0 bosons and is responsible for radioactive nuclear decay in particular and for flavor-changing quark and lepton transitions in general. One of the major achievements of the SM was to demonstrate unification of the weak and electromagnetic forces.

While the SM remains extremely successful in explaining all existing experimental data, there are several facts about it which remain unclear. First, there is the Higgs mechanism which gives masses to all particles in the model, but also requires the existence of a fundamental scalar known as the Higgs boson. Discovery of the Higgs boson will probably happen in the not so distant future at one of the experiments currently under construction. Second, there is a problem of CP violation, which was observed so far only in $K^0 - \bar{K}^0$ system [2] and is expected to be seen in B mesons as well. While this single observation can be accommodated in the Standard Model, its exact origin is unclear. We know that the current cosmological model of the Universe's origin , a.k.a the "Big Bang" requires CP violation to produce an excess of matter over antimatter [3]. After all, starting with an equal amount of matter and antimatter in the very beginning, one needs some sort of asymmetry which would let matter prevail and produce the baryon density of the universe we are seeing now. It is interesting to note that at the current level of theoretical knowledge, amount of CP violation present in the Standard Model appears to be insufficient [4]. Assuming that this is the case, motivation to search for CP violation in B decays is quite obvious. By performing a detailed study of CP violation in the B meson system in the near future, we hope to test whether the SM provides an adequate description of the CP violating phenomena. It turns out that rare B meson decays into a pair of light pseudoscalar mesons such as $K\pi$ and $\pi\pi$ will play an important role in these tests.

This concludes the short introduction into the subject of the thesis. In the following sections we review quark-mixing in the SM and describe the CKM mechanism of CP violation. We then proceed to describe the theory of the two-body charmless B decays of interest. We'll briefly describe ways to test the SM picture of CP violation with special attention to the methods involving $B \to K\pi, \pi\pi$ decays. In the end we will discuss possible implications of the physics beyond the SM on our processes.

1.2 Quark mixing

We begin by demonstrating the origin of the quark-mixing matrix. Recall that in the SM fermions receive masses from their Yukawa-like coupling to the Higgs field

$$\mathcal{L}(f,\Phi) = \sum_{j,k=1}^{3} \left\{ \left(h'_q\right)_{jk} \bar{q}_L^j \Phi u_R^k + (h_q)_{jk} \bar{q}_L^j \Phi^c d_R^k \right\} . \tag{1.1}$$

Yukawa coupling constants $(h_q)_{jk}$ and $(h'_q)_{jk}$ are arbitrary complex numbers. After spontaneous symmetry breaking the Higgs field Φ acquires a non-zero vacuum expectation value v

$$\mathcal{L}(f,\phi)^{\mathrm{SSB}} = -\sum_{j,k=1}^{3} \left\{ (m_{jk})_U \bar{u}_L^j u_R^k + (m_{jk})_D \bar{d}_L^j d_R^k \right\} (1 + \frac{1}{v}\phi) + \text{h. c. } , \tag{1.2}$$

where

$$\begin{aligned} (m_{jk})_U &= -(h_q)_{jk} \frac{v}{\sqrt{2}} , \\ (m_{jk})_D &= -\left(h'_q\right)_{jk} \frac{v}{\sqrt{2}} . \end{aligned} \tag{1.3}$$

are the (3×3) quark mass matrices for the up- and down-type quarks. In order to rewrite the Lagrangian in terms of the quark mass eigenstates, we need to diagonalize these mass matrices. It can be done with the help of two unitary matrices (different for up- and down-type quarks):

$$\begin{aligned} (m_{\rm diag.})_U &\equiv V_L^{\rm up} m_U V_R^{\rm up\dagger}, \\ (m_{\rm diag.})_D &\equiv V_L^{\rm down} m_D V_R^{\rm down\dagger} \end{aligned} \tag{1.4}$$

with $V_L^{\rm up\dagger} V_L^{\rm up} = 1$, and so on. It follows then that the physical quark fields are:

$$\begin{aligned} u_L^{i({\rm Phys})} &= \left(V_L^{\rm up} u_L\right)^i, \\ d_L^{i({\rm Phys})} &= \left(V_L^{\rm down} d_L\right)^i, \\ u_R^{i({\rm Phys})} &= \left(V_R^{\rm up} u_R\right)^i, \\ d_R^{i({\rm Phys})} &= \left(V_R^{\rm down} d_R\right)^i. \end{aligned} \tag{1.5}$$

Now we are in a position to discuss the charged current involving quarks. Starting with the flavor eigenstates and transforming them into mass-eigenstates as outlined above, we obtain:

$$\begin{aligned} \mathcal{L}^{CC} &= \frac{e}{\sqrt{2}\sin\theta_W} \sum_{i=1}^{3} \bar{u}_L^i \gamma^\mu W_\mu^+ d_L^i + \text{h.c.} \\ &= \frac{e}{\sqrt{2}\sin\theta_W} \sum_{i=1}^{3} \bar{u}_L^i V_L^{\rm up\dagger} V_L^{\rm up} \gamma^\mu W_\mu^+ V_L^{\rm down\dagger} V_L^{\rm down} d_L^i + \text{h.c.} \\ &= \frac{e}{\sqrt{2}\sin\theta_W} \sum_{i=1}^{3} \left(\bar{u}_L^{\rm Phys}\right)^i \gamma^\mu W_\mu^+ \left(V_L^{\rm up} V_L^{\rm down\dagger}\right)_{ij} \left(d_L^{\rm Phys}\right)^j + \text{h.c.} \end{aligned} \tag{1.6}$$

and the quark charged current takes the form of

$$J_\mu^{CC} = \frac{e}{\sqrt{2}\sin\theta_W}\,(\bar{u},\bar{c},\bar{t})_L\,\gamma_\mu V_{\mathrm{CKM}}\begin{pmatrix} d \\ s \\ b \end{pmatrix}_L . \tag{1.7}$$

Here we introduced the CKM matrix $V_{\mathrm{CKM}} \equiv V_L^{\mathrm{up}} V_L^{\mathrm{down}\dagger}$ which is a (3×3) unitary matrix, first written by Kobayashi and Maskawa [5], which generalizes Cabibbo mixing to three quark families. It is therefore called the Cabibbo-Kobayashi-Maskawa matrix and symbolically is usually written as

$$V_{\mathrm{CKM}} \equiv \begin{pmatrix} V_{ud} & V_{us} & V_{ub} \\ V_{cd} & V_{cs} & V_{cb} \\ V_{td} & V_{ts} & V_{tb} \end{pmatrix}. \tag{1.8}$$

It can be shown that the CKM matrix, being an arbitrary unitary matrix, can be parameterized with three angles and one phase. The original parameterization, written by Kobayashi and Maskawa is

$$V_{\mathrm{KM}} = \begin{pmatrix} c_1 & -s_1c_3 & -s_1s_3 \\ s_1c_2 & c_1c_2c_3 - s_2s_3e^{i\delta} & c_1c_2s_3 + s_2c_3e^{i\delta} \\ s_1s_2 & c_1s_2c_3 + c_2s_3e^{i\delta} & c_1s_2s_3 - c_2c_3e^{i\delta} \end{pmatrix}, \tag{1.9}$$

with $c_i = \cos\theta_i,\ s_i = \sin\theta_i$. Another useful approximate form of the CKM matrix is due to Wolfenstein [6]:

$$V_{\mathrm{Wolfenstein}} = \begin{pmatrix} 1-\frac{1}{2}\lambda^2 & \lambda & A\lambda^3(\rho - i\eta) \\ -\lambda & 1-\frac{1}{2}\lambda^2 & A\lambda^2 \\ A\lambda^3(1-\rho-i\eta) & -A\lambda^2 & 1 \end{pmatrix}. \tag{1.10}$$

One can see that we still have three real parameters (A, λ and ρ) and a "phase" η. The Wolfenstein parameterization demonstrates the hierarchy of the CKM elements very nicely and we will use it extensively in the subsequent discussion.

Unitarity of the CKM matrix implies several triangle relations, of which the most important for B physics is given below.

$$V_{ud}V_{ub}^* + V_{cd}V_{cb}^* + V_{td}V_{tb}^* = 0 \tag{1.11}$$

In the Wolfenstein parameterization it takes the form

$$A\lambda^3(\rho + i\eta) - A\lambda^3 + A\lambda^3(1 - \rho - i\eta) = 0 \tag{1.12}$$

and is usually represented nicely in the (ρ, η) plane as shown in Figure 1.1.

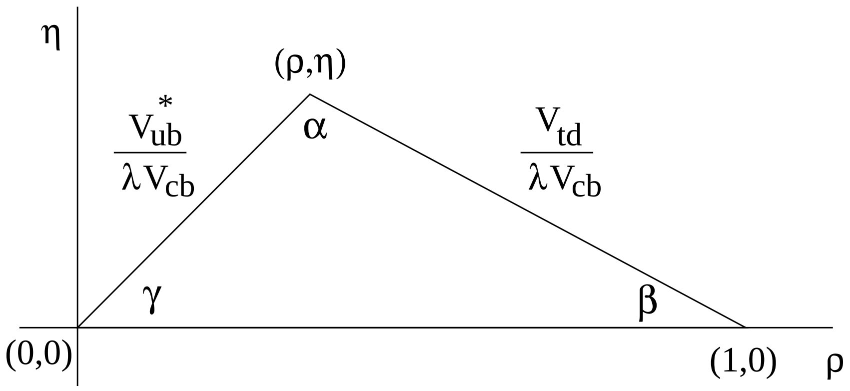

Figure 1.1: Unitarity triangle.

At the moment the only direct experimental evidence for CP violation comes from the K-system, while other measurements constrain the sides of the triangle as can be seen in Figure 1.2 [7]. To further illustrate the need to overconstrain

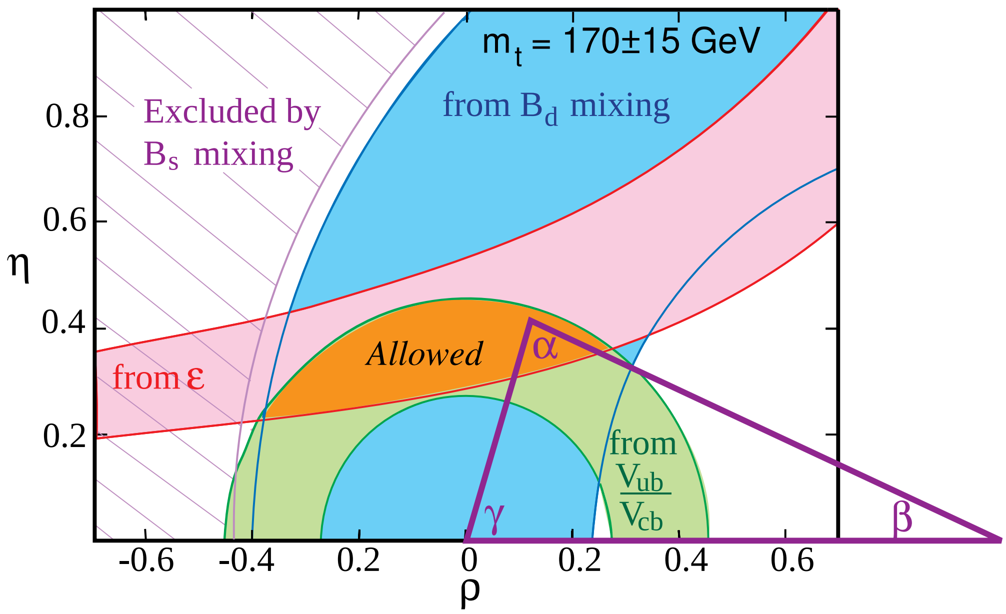

Figure 1.2: Current knowledge of the unitarity triangle.

the unitarity triangle in order to test the SM, we show the "perfect" triangle [8] in Figure 1.3 with all measurements agreeing on the particular value of (ρ, η).

Before we go further discussing the CKM matrix, let's note that it is, along with fermion masses, a parameter of the Standard Model (4 parameters, to be precise) and its origin hopefully will be explained by the SM extensions. At the moment, we are left with the task of measuring the CKM elements experimentally.

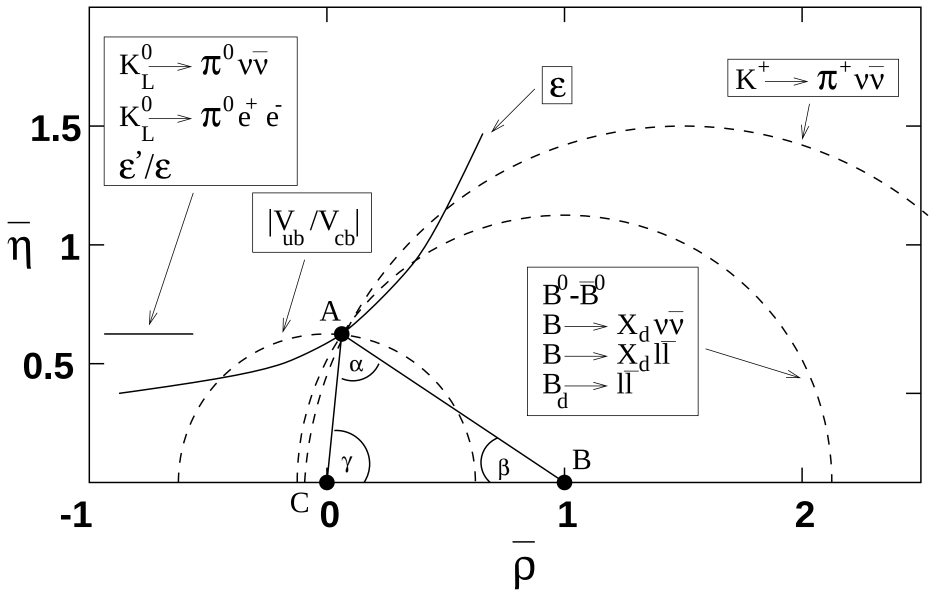

Figure 1.3: "Ideal" unitarity triangle, with agreeing experimental constraints superimposed.

1.3 $B^0 - \bar{B}^0$ mixing and CP violation in the Standard Model

Apart from being responsible for the mixing between quark families, charged current interactions produce particle-antiparticle mixing for the neutral mesons, such as K^0, D^0, B_d^0 and B_s^0. In the SM this mixing is due to box diagrams shown in Figure 1.4. As a result, mass eigenstates are no longer flavor eigenstates, that is

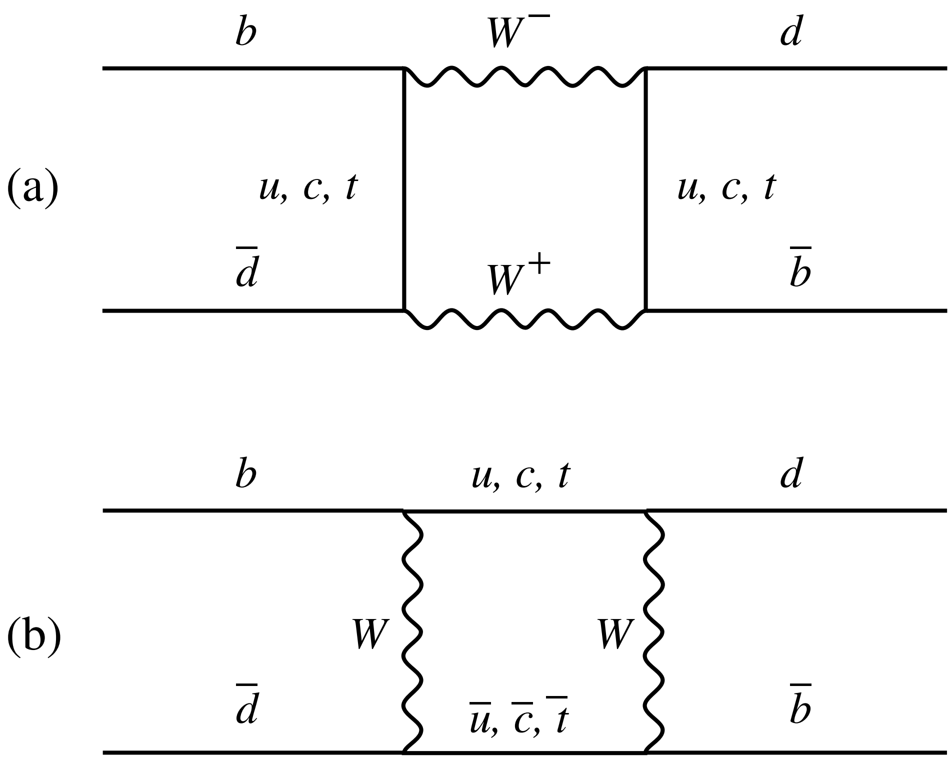

Figure 1.4: Box diagrams responsible for the $B^0 - \bar{B}^0$ mixing.

we have "Light" and "Heavy" eigenstates B_L and B_H

$$|B_L\rangle = p|B^0\rangle + q|\bar{B}^0\rangle \ , \quad |B_H\rangle = p|P^0\rangle - q|\bar{B}^0\rangle \ . \tag{1.13}$$

with masses $m_{L,H}$ and widths $\Gamma_{L,H}$. The Hamiltonian eigenvalue equation has the form

$$\begin{pmatrix} M - \frac{i}{2}\Gamma & M_{12} - \frac{i}{2}\Gamma_{12} \\ M_{12}^* - \frac{i}{2}\Gamma_{12}^* & M - \frac{i}{2}\Gamma \end{pmatrix} \begin{pmatrix} p \\ \pm q \end{pmatrix} = (m_{L,H} - \frac{i}{2}\Gamma_{L,H}) \begin{pmatrix} p \\ \pm q \end{pmatrix} \ . \tag{1.14}$$

Off-diagonal terms in the mass matrix are due to the $B^0 - \bar{B}^0$ transitions caused by box diagrams. Γ_{12} in the decay matrix describes decay channels common to B^0 and $\bar{B}^0$. Solving for q and p yields

$$\frac{q}{p} = \sqrt{\frac{M_{12}^* - \frac{i}{2}\Gamma_{12}^*}{M_{12} - \frac{i}{2}\Gamma_{12}}} = -\frac{2(M_{12}^* - \frac{i}{2}\Gamma_{12}^*)}{\Delta m - \frac{i}{2}\Delta\Gamma} \ , \tag{1.15}$$

where $\Delta m \equiv m_H - m_L, \ \Delta\Gamma \equiv \Gamma_H - \Gamma_L$.

Given that the decay channels common to B^0 and $\bar{B}^0$ typically have branching fractions on the order of 10^{-3} ($Br(B^0 \to J/\Psi K_S^0) = (7.5 \pm 2.1) \times 10^{-4}$) [9] or less, one expects $|\Delta\Gamma|/\Gamma < 10^{-2}$. Combined with the observed $B^0 - \bar{B}^0$ mixing which implies $\Delta M/\Gamma = 0.7$, we conclude that

$$|\Delta\Gamma| \ll \Delta M, \qquad |\Gamma_{12}| \ll |M_{12}| \ . \tag{1.16}$$

This allows us to rewrite 1.15 as

$$\frac{q}{p} \simeq \sqrt{\frac{M_{12}^*}{M_{12}}} \ . \tag{1.17}$$

Deviation of $|q/p|$ from one measures CP violation in $B^0 - \bar{B}^0$ mixing and it is expected to be small in the SM, $1 - |q/p| \sim \mathcal{O}(10^{-3})$ [10]. As we will see later, CP violating asymmetries in B *decays* are much larger than those in the $B^0 - \bar{B}^0$ *mixing*, so we'll assume $|q/p| = 1$ from now on. In this approximation the mixing parameter q/p is a pure phase, given in the case of $B_d^0 - \bar{B}_d^0$ mixing by

$$\frac{q}{p} \simeq \sqrt{\frac{M_{12}^*}{M_{12}}} = \frac{V_{tb}^* V_{td}}{V_{tb} V_{td}^*} = e^{-2i\beta} \ . \tag{1.18}$$

We now proceed to discuss specific aspects of CP violation in the B system.

1.3.1 Direct CP violation

The simplest manifestation of CP violation is the difference in the decay rate between $B \to f$ and $\bar{B} \to \bar{f}$ processes. To avoid complications associated with mixing, let us consider decays of the charged B mesons. In order to get different rates, three conditions have to be met:

- Two amplitudes (A_1, A_2) must contribute;
- The amplitudes should have different weak (CKM) phases ϕ_1 and ϕ_2;
- The amplitudes should have different strong phases δ_1 and δ_2,

$$\begin{aligned} A(B^+ \to f) &= |A_1| e^{i\phi_1} e^{i\delta_1} + |A_2| e^{i\phi_2} e^{i\delta_2} \ , \\ \bar{A}(B^- \to \bar{f}) &= |A_1| e^{-i\phi_1} e^{i\delta_1} + |A_2| e^{-i\phi_2} e^{i\delta_2} \ . \end{aligned} \tag{1.19}$$

If this is the case, then the rate difference will be proportional to

$$|A|^2 - |\bar{A}|^2 = 2|A_1 A_2| \sin(\phi_1 - \phi_2) \sin(\delta_1 - \delta_2) \ . \tag{1.20}$$

The decay $B^+ \to K^+\pi^0$ can serve as an example for this scenario. Figure 1.5 shows Feynman diagrams for the "tree" and "penguin" amplitudes with different weak phases of $\phi_T = \gamma$ and $\phi_P = \pi$. The penguin amplitude can provide the necessary

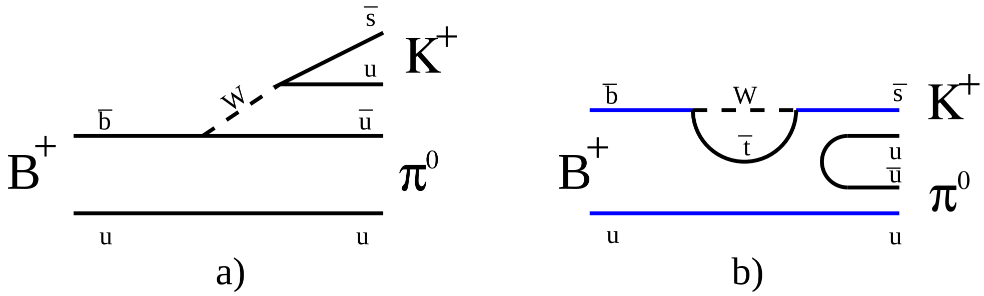

Figure 1.5: Tree a) and penguin b) diagrams for the decay $B^+ \to K^+\pi^0$.

strong phase difference due to the absorptive part of the physical $c\bar{c}$ quark pair in the loop [11]. Several calculations [12] exist for the asymmetry in this decay mode, all suffering from the large theoretical uncertainties.

It is definitely worthwhile to look for CP violation in the charged B decays, but interpretation of the results will be complicated, probably preventing us from reliable measurement of CKM phases using Eq. 1.20 only. There are, however, more elaborate methods allowing CKM phase extraction from charged B decays, which will be described later.

1.3.2 CP violation in the decays of mixed $B^0 - \bar{B}^0$ mesons

As we've just seen, it is essential to have two interfering amplitudes to produce CP violating asymmetry. The $B^0 - \bar{B}^0$ system provides an elegant mechanism for the interference: amplitudes to consider are $B^0 \to f$ and $B^0 \to \bar{B}^0 \to f$. f in general is a final state which is accessible both from B^0 and $\bar{B}^0$. For simplicity, we'll assume that f is a CP eigenstate such as $\pi^+\pi^-$. Time-dependent decay rates to f for the initially pure B^0 and $\bar{B}^0$ are given by

$$\Gamma(B^0(t) \to f) = e^{-\Gamma t}|A|^2 \Big\{ \frac{1 + |\frac{\bar{A}}{A}|^2}{2} + \frac{1 - |\frac{\bar{A}}{A}|^2}{2} \cos(\Delta M t) - Im(\frac{q\bar{A}}{pA}) \sin(\Delta M t) \Big\} , \tag{1.21}$$

$$\Gamma(\bar{B}^0(t) \to f) = e^{-\Gamma t}|A|^2 \Big\{ \frac{1 + |\frac{\bar{A}}{A}|^2}{2} - \frac{1 - |\frac{\bar{A}}{A}|^2}{2} \cos(\Delta M t) + Im(\frac{q\bar{A}}{pA}) \sin(\Delta M t) \Big\} . \tag{1.22}$$

The time-dependent asymmetry is

$$\frac{\Gamma - \bar{\Gamma}}{\Gamma + \bar{\Gamma}} = \frac{(1 - |\frac{\bar{A}}{A}|^2) \cos(\Delta M t) - 2 Im(\frac{q\bar{A}}{pA}) \sin(\Delta M t)}{1 + |\frac{\bar{A}}{A}|^2} . \tag{1.23}$$

In the absence of direct CP violation, that is if only one decay amplitude contributes, or different amplitudes have the same weak phases, $|A| = |\bar{A}|$ and Eq. 1.23 simplifies,

$$a_{CP}(t) = \frac{\Gamma - \bar{\Gamma}}{\Gamma + \bar{\Gamma}} = \mp Im(\frac{q\bar{A}}{pA}) \sin(\Delta M t) , \tag{1.24}$$

allowing extraction of the CKM phases. The overall sign is determined by the CP eigenvalue, ± 1, of the final state f.

Consider for example the decay $B^0 \to J/\Psi K_S^0$. It is dominated by the quark-level transition $\bar{b} \to \bar{c}c\bar{s}$ and, with $CP(J/\Psi K_S^0) = -1$, we get

$$\frac{q\bar{A}}{pA} = \frac{V_{td}V_{tb}^*}{V_{td}^*V_{tb}} \times \frac{V_{cd}^*V_{cs}}{V_{cd}V_{cs}^*} \times \frac{V_{cb}V_{cs}^*}{V_{cb}^*V_{cs}} = e^{-i2\beta} . \tag{1.25}$$

The ratio $\frac{V_{cd}^* V_{cs}}{V_{cd} V_{cs}^*}$ comes from the presence of K_S^0 in the final state. The time-dependent asymmetry is

$$a_{CP}(J/\Psi K_S^0, t) = -\sin(2\beta)\sin(\Delta M t) \tag{1.26}$$

and measurement of $\sin(2\beta)$ becomes possible. This is a very clean way of determining β, since the penguin amplitude, while contributing at some level, has the same weak phase as the dominant tree amplitude and doesn't spoil Eq. 1.26. This is not the case in the next example of the decay $B^0 \to \pi^+\pi^-$. Assuming that decay is dominated by the tree amplitude,

$$\frac{q\bar{A}}{pA} = \frac{V_{td} V_{tb}^*}{V_{td}^* V_{tb}} \times \frac{V_{ub} V_{ud}^*}{V_{ub}^* V_{ud}} = e^{-i2\beta} e^{-i2\gamma} \ , \tag{1.27}$$

and asymmetry is

$$a_{CP}(\pi^+\pi^-, t) = \sin(2(\beta+\gamma))\sin(\Delta M t) = -\sin(2\alpha)\sin(\Delta M t) \ , \tag{1.28}$$

where in the last step we assumed SM relationship between the angles. Eq. 1.28 is one of the advertised ways to measure angle α but as we'll see immediately, it is not as theoretically clean as Eq.1.26. The problem lies in the presence of the penguin amplitude with *different* weak phase and (probably) different strong phase, that is

$$A(B^0 \to \pi^+\pi^-) = A_T + A_P = |A_T| e^{i\gamma} e^{i\delta_T} + |A_P| e^{-i\beta} e^{i\delta_P} \ . \tag{1.29}$$

Coefficients in front of $\cos(\Delta M t)$ and $\sin(\Delta M t)$ terms in Eq. 1.23 are now given [13] by

$$\frac{2Im(\frac{q\bar{A}}{pA})}{1+|\frac{q\bar{A}}{pA}|^2} \simeq -\sin(2(\beta+\gamma)) + |\frac{A_P}{A_T}| \cos(2(\beta+\gamma))\sin(\beta+\gamma)\cos(\delta_T - \delta_P) \ , \tag{1.30}$$

$$\frac{1-|\frac{q\bar{A}}{pA}|^2}{1+|\frac{q\bar{A}}{pA}|^2} \simeq -2|\frac{A_P}{A_T}|\sin(\beta+\gamma)\sin(\delta_T-\delta_P)\ . \tag{1.31}$$

Note that for the case of $\delta_T = \delta_P$ and $\gamma + \beta = \pi/2$ instead of $a_{CP}(\pi^+\pi^-, t) = 0$ one will measure *non-zero* asymmetry $a_{CP}(\pi^+\pi^-, t) = -|\frac{A_P}{A_T}|\sin(\Delta M t)$. In the general case, one must disentangle effects of the penguin amplitude to extract the true value of α. This problem is known as "penguin pollution". There are several methods to control penguin effects in this decay and we'll discuss them in the later section.

We conclude this section with several remarks concerning the experimental aspects of the measurement of the CP violating asymmetries in the B system. Observation of the direct CP violation is straightforward from the experimental point of view, since only the rate measurements are needed. Experiments running at high-luminosity e^+e^- machines will be able to look for direct CP violation in self-tagging B^0 decays such as $B^0 \to K^+\pi^-$ and charged B's ($B^+ \to K^+\pi^0, \eta' K^+$ etc.). Planned experiments at the hadronic colliders are capable of studying direct CP violation as well, although modes with neutrals in the final state will be a problem.

Measurement of time-dependent asymmetries is more complicated. First, one has to know whether B meson decaying into a CP eigenstate started as B^0 or $\bar{B}^0$. At the e^+e^- machines running on the $\Upsilon(4S)$ resonance $B^0\bar{B}^0$ pair is produced in a definite CP-eigenstate and evolves coherently until one of the particles decays. One can use events where one of the B's decayed into a flavor specific final state, while the other decays into CP eigenstate mode. In this case t in the Eq. 1.24

refers to the time between the tagging decay and decay into CP mode of interest. Note that in this scenario time-integrated asymmetry vanishes, which precludes this kind of measurement at the symmetric e^+e^- machine such as CESR. To overcome this obstacle, future B-factories under construction at SLAC and KEK will use asymmetric beam energies, producing boosted B mesons in the lab frame. Therefore it will be possible to measure the sign of t and non-zero a_{CP}.

Hadron machines, on the other hand, do not produce correlated B's and the time t in the above equations refers to the time between production and decay, which is always positive. Tagging is achieved by the methods similar to e^+e^- experiments and also through $B - \pi$ correlated production.

1.4 Theoretical description of B decays

The purpose of this section is to provide a short overview of the theory of exclusive nonleptonic decays of B mesons. The emphasis will be on the theoretical description of the heavy-to-light transitions, that is decays of the $b \to u$ and $b \to s$ kind. The picture of the current theoretical understanding will be painted with very broad brush strokes, without going into technical details but providing as many references as possible to the original work.

1.4.1 Feynman diagrams

All relevant lowest level Feynman diagrams for the processes of interest are shown in Figure 1.6. Table 1.1 lists decomposition of the decay amplitudes for our pro-

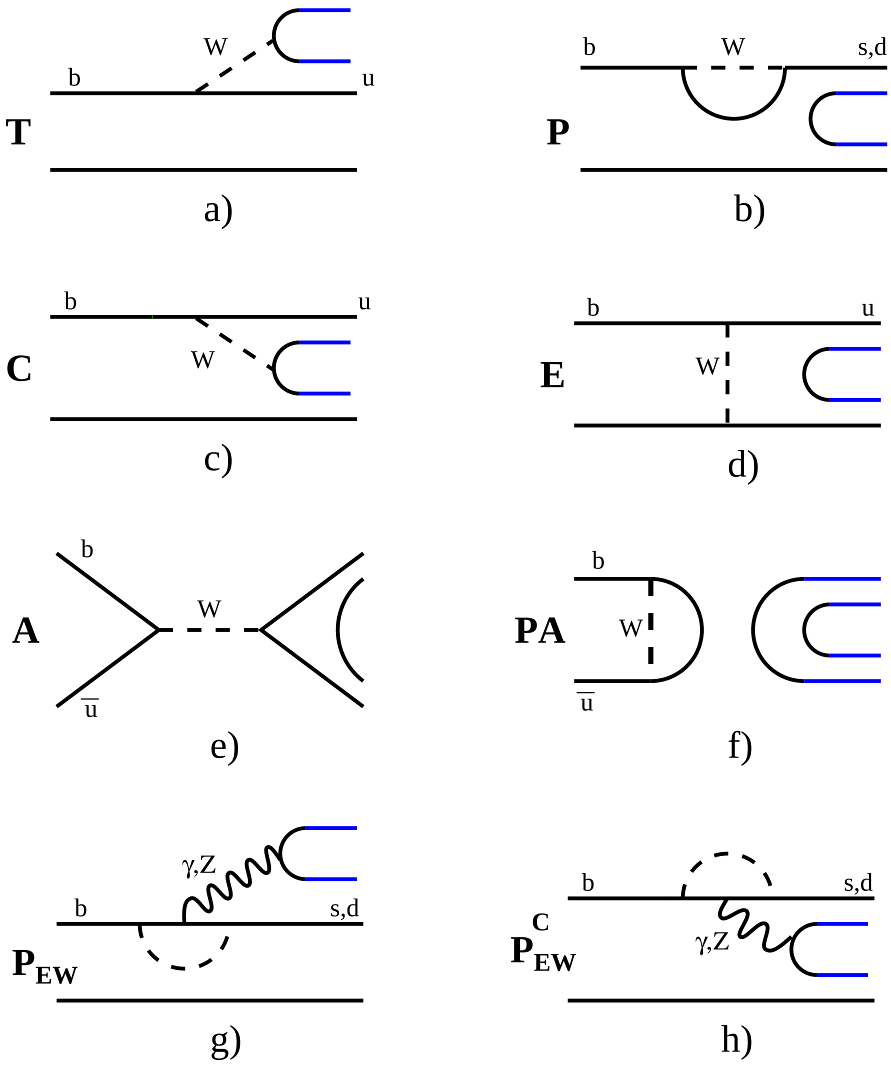

Figure 1.6: Feynman diagrams for $B \to K\pi, \pi\pi$ decays: a) $b \to u$ external W emission, b) $b \to s, d$ gluonic penguin, c) $b \to u$ internal W emission, d) W exchange, e) annihilation, f) penguin annihilation, g) external electroweak penguin, h) internal electroweak penguin.

cesses in terms of Feynman diagrams [14, 15]. Unprimed labels refer to $b \to d$ transitions, while primed are reserved for $b \to s$ decays.

Table 1.1: Decomposition of $B \to K\pi, \pi\pi$ decays in terms of Feynman diagrams.

Decay mode	Normal	EW Penguins
$B^0 \to \pi^+\pi^-$	$-(P+T+E+PA)$	$-c_u P^C_{EW}$
$B^0 \to \pi^0\pi^0$	$-(C-P-E-PA)/\sqrt{2}$	$-((c_u-c_d)P_{EW}+c_d P^C_{EW})/\sqrt{2}$
$B^+ \to \pi^+\pi^0$	$-(T+C)/\sqrt{2}$	$-(c_u-c_d)(P_{EW}+P^C_{EW})/\sqrt{2}$
$B^+ \to K^+\bar{K}^0$	$(P+A)$	$c_d P^C_{EW}$
$B^0 \to K^+\pi^-$	$-(P'+T')$	$-c_u P'^C_{EW}$
$B^0 \to K^0\pi^0$	$-(P'-C')/\sqrt{2}$	$-((c_u-c_d)P'_{EW}-c_d P'^C_{EW})/\sqrt{2}$
$B^+ \to K^+\pi^0$	$-(P'+T'+C'+A)/\sqrt{2}$	$-((c_u-c_d)P'_{EW}+c_u P'^C_{EW})/\sqrt{2}$
$B^+ \to K^0\pi^+$	$P'+A$	$c_d P'^C_{EW}$

To illustrate the relative size of the diagrams we provide the following hierarchy [15] in the Table 1.2. One has to keep in mind that parameter $\lambda \simeq 0.2$ appearing in Table 1.2 has nothing to do with λ we saw in the Wolfenstein parameterization of the CKM matrix. It is simply used as a convenient measure of the approximate relative sizes. For instance, $|C/T| \sim \lambda$ comes from the color suppression, while $|A/T|$ contains the factor $f_B/m_B \simeq 0.05 \sim \lambda^2$. One also should take these hierarchies with a grain of salt, given the large theoretical uncertainties involved. In the

Table 1.2: Relative size of various diagrams.

Relative size	$b \to d$	$b \to s$
1	$\lvert T\rvert$	$\lvert P'\rvert$
$\mathcal{O}(\lambda)$	$\lvert C\rvert, \lvert P\rvert$	$\lvert T'\rvert, \lvert P'_{EW}\rvert$
$\mathcal{O}(\lambda^2)$	$\lvert E\rvert, \lvert A\rvert, \lvert P_{EW}\rvert$	$\lvert C'\rvert, \lvert PA'\rvert, \lvert P'^{C}_{EW}\rvert$
$\mathcal{O}(\lambda^3)$	$\lvert PA\rvert, \lvert P^{C}_{EW}\rvert$	$\lvert E'\rvert, \lvert A'\rvert$

end it is up to experiment to establish the true size of each diagram.

1.4.2 Effective Lagrangians

The basic idea under the theory of the weak decays of the B meson is the effective field theory. In this approach one doesn't deal with the full Hamiltonian of electroweak theory and QCD, but instead replaces it with "effective" Hamiltonian, which has all heavy degrees of freedom (W, Z, top quark) integrated out. This is perfectly justifiable, since we are dealing with the energy scales much less than m_W, m_Z, m_t etc. This is exactly what the Fermi theory of weak decays is, when couplings of the "true" electroweak interaction along with the full W propagator are embedded in the effective constant of the weak interaction G_F. In this picture our effective Hamiltonian for the transition $b \to c\bar{c}s$ is:

$$H_{eff} = \frac{G_F}{\sqrt{2}} V_{cb} V^*_{cs} (\bar{c}b)_{V-A} (\bar{s}c)_{V-A} \tag{1.32}$$

and we can introduce the local (V-A)(V-A) current-current operator Q_2 given by

$$Q_2 = (\bar{c}b)_{V-A}(\bar{s}c)_{V-A} \equiv (\bar{c}\gamma_\mu(1-\gamma_5)b)(\bar{s}\gamma^\mu(1-\gamma_5)c) \ . \tag{1.33}$$

In this sense, when drawing familiar Feynman diagrams describing B decays on the quark level, we are dealing with the full theory containing six quarks, W and Z bosons. By explicitly drawing lines representing W, Z, and top-quark propagators, we describe what happens at the energy scale of the order of $\mathcal{O}(m_W)$. In reality, hadron decay occurs at the energy scale of $\mathcal{O}(m_b)$, and interactions become essentially point-like with effective vertices represented by the local operators.

The presence of other interactions in the SM leads to operators different from Q_2 in their Dirac and color structure. One usually starts at the high energy scale and integrates out the heavy (with respect to μ, characteristic energy scale of the decay) degrees of freedom from explicitly appearing in the problem. These degrees of freedom do not disappear, but become hidden in the effective coupling constants, running masses and in the Wilson coefficient functions $C_i(\mu)$ which describe the "strength" of the operator at a given scale μ. The effective Hamiltonian in this approach takes the form

$$H_{eff} = \frac{G_F}{\sqrt{2}} \sum_i V_{CKM} C_i(\mu) Q_i \ . \tag{1.34}$$

In general, the amplitude for the exclusive decay $M \to F$ is given by

$$A(M \to F) = \frac{G_F}{\sqrt{2}} \sum_i V_{CKM} C_i(\mu) \langle F|Q_i(\mu)|M\rangle \ , \tag{1.35}$$

where M is initial meson, F is the final state, and V_{CKM} are relevant CKM factors. $< Q_i(\mu) >$ are matrix elements of the local operators Q_i which can be classified as follows [16]:

- Current-current operators:

$$\begin{aligned} Q_1^{jq} &= (\bar{q}_\alpha j_\beta)_{\mathrm{V-A}} (\bar{j}_\beta b_\alpha)_{\mathrm{V-A}} \\ Q_2^{jq} &= (\bar{q}_\alpha j_\alpha)_{\mathrm{V-A}} (\bar{j}_\beta b_\beta)_{\mathrm{V-A}} \end{aligned} \tag{1.36}$$

- QCD penguin operators:

$$\begin{aligned} Q_3^q &= (\bar{q}_\alpha b_\alpha)_{\mathrm{V-A}} \sum_{q'} (\bar{q}'_\beta q'_\beta)_{\mathrm{V-A}} \\ Q_4^q &= (\bar{q}_\alpha b_\beta)_{\mathrm{V-A}} \sum_{q'} (\bar{q}'_\beta q'_\alpha)_{\mathrm{V-A}} \\ Q_5^q &= (\bar{q}_\alpha b_\alpha)_{\mathrm{V-A}} \sum_{q'} (\bar{q}'_\beta q'_\beta)_{\mathrm{V+A}} \\ Q_6^q &= (\bar{q}_\alpha b_\beta)_{\mathrm{V-A}} \sum_{q'} (\bar{q}'_\beta q'_\alpha)_{\mathrm{V+A}} \end{aligned} \tag{1.37}$$

- EW penguin operators:

$$\begin{aligned} Q_7^q &= \tfrac{3}{2} (\bar{q}_\alpha b_\alpha)_{\mathrm{V-A}} \sum_{q'} e_{q'} (\bar{q}'_\beta q'_\beta)_{\mathrm{V+A}} \\ Q_8^q &= \tfrac{3}{2} (\bar{q}_\alpha b_\beta)_{\mathrm{V-A}} \sum_{q'} e_{q'} (\bar{q}'_\beta q'_\alpha)_{\mathrm{V+A}} \\ Q_9^q &= \tfrac{3}{2} (\bar{q}_\alpha b_\alpha)_{\mathrm{V-A}} \sum_{q'} e_{q'} (\bar{q}'_\beta q'_\beta)_{\mathrm{V-A}} \\ Q_{10}^q &= \tfrac{3}{2} (\bar{q}_\alpha b_\beta)_{\mathrm{V-A}} \sum_{q'} e_{q'} (\bar{q}'_\beta q'_\alpha)_{\mathrm{V-A}} \end{aligned} \tag{1.38}$$

and $C_i(\mu)$ are Wilson coefficient functions. The essential point of the operator product expansion (OPE) described above is to achieve the separation of the full problem into two distinct parts: long distance effects described by the matrix elements and the short distance physics contained in the Wilson coefficients.

The short distance part can be analyzed with the help of well developed methods of the field theory. $C_i(\mu)$ are evaluated at the m_W scale and then are evolved down to the scale μ using the renormalization group technique [17]. A recent review [18] describes in great detail the calculation of the Wilson coefficients in the

Table 1.3: $\Delta B = 1$ Wilson coefficients at $\mu = \overline{m}_{\rm b}(m_{\rm b}) = 4.40\,\mathrm{GeV}$ for $m_{\rm t} = 170\,\mathrm{GeV}$. NDR and HV refer to different regularization schemes.

	$\Lambda^{(5)}_{\overline{\rm MS}} = 225\,\mathrm{MeV}$			$\Lambda^{(5)}_{\overline{\rm MS}} = 290\,\mathrm{MeV}$		
Scheme	LO	NDR	HV	LO	NDR	HV
C_1	-0.308	-0.185	-0.228	-0.331	-0.198	-0.245
C_2	1.144	1.082	1.105	1.156	1.089	1.114
C_3	0.014	0.014	0.013	0.016	0.016	0.014
C_4	-0.030	-0.035	-0.029	-0.032	-0.038	-0.032
C_5	0.009	0.009	0.009	0.009	0.009	0.010
C_6	-0.038	-0.041	-0.033	-0.041	-0.045	-0.036
C_7/α	0.045	-0.002	0.005	0.047	-0.002	0.005
C_8/α	0.048	0.054	0.060	0.053	0.059	0.065
C_9/α	-1.280	-1.292	-1.283	-1.290	-1.300	-1.293
C_{10}/α	0.328	0.263	0.266	0.352	0.281	0.284

leading logarithmic (LO) and the next-to-leading logarithmic (NLO) approximations. Table 1.3 [8] lists numerical values of the Wilson coefficients.

Evaluation of the operator matrix elements is very difficult, since it deals with low-energy strong interactions. In the majority of cases one uses a factorization approximation, that is the matrix element of the four-quark operator Q is factorized into the product of the current matrix elements as follows ($\bar{B}^0 \to K^-\pi^+$ is given as an example):

$$\langle K^-\pi^+|Q_i|\bar{B}^0\rangle = \langle K^-|(\bar{s}u)_{V-A}|0\rangle\langle\pi^+|(\bar{u}b)_{V-A}|\bar{B}^0\rangle \; . \tag{1.39}$$

Factorization assumes that K^- meson $(s\bar{u})$ in our case is formed from W^- directly and doesn't interact with the other hadron in the decay. Typically the "color transparency" argument due to Bjorken [19] is invoked, that is , when a fast $s\bar{u}$ pair is created from W^-, it travels fast enough to hadronize far away from the interaction point. Inside the interaction region it behaves like a point-like colorless particle. While such a picture is quite plausible for the external tree amplitudes, it is not clear whether it is applicable for the color suppressed tree and/or penguin amplitudes in particular. In the end, the factorization hypothesis should be tested by experiment. Once factorization is assumed, note that current matrix elements appearing above are closely related to the K^+ meson decay constant and the heavy-to-light form factor appearing also in the $b \to u$ semileptonic decays. It is therefore possible to measure them experimentally or use theoretical results from the work on semileptonic B decays.

Over the years several methods of dealing with hadronic form factors have been introduced: lattice calculations [20, 21], QCD sum rules [22], chiral perturbation theory [23, 24], quark models [25–27] etc. Each of the methods has its own advantages and disadvantages. Lattice calculations are rigorous from the QCD point of view, but at the moment can be applied only to the simple cases of the decay constants and form factors. Quark models are easy to use, but their relation to QCD is unclear and they are not a systematic expansion of the fundamental theory in some small parameter. Therefore, a calculation can be correct or not, but its uncertainty can't be reduced by going to the higher orders in the expansion.

1.4.3 Theoretical predictions

We summarized theoretical predictions for the modes of interest in the Table 1.4. Practically all results use the effective Hamiltonian approach described above. Deandrea et al.(DDGFN) [23] used data to estimate form factors for the tree amplitudes, hence the errors in the branching fractions for $\pi\pi$ final states. The large spread in the penguin-dominated modes for DDGFN is due to the full range of the $\cos\gamma$ used. For the oldest paper in our collection, Bauer et al. (uBSW), we quote "updated" results [73], with the same input parameters as used by DDGFN. The BSW model of form factors [25] was the most popular choice, with the exception of Ebert et al. (EFG) [28], who used their own relativistic quark model. Kramer and Palmer (KP) [32], Du and Guo (DG) [29] included electroweak penguins in their calculations. Ebert et al. considered only tree-dominated decays, while Deshpande and Trampetic (DT) [31] performed calculations for the processes dominated by the $b \to sg$ transition. Note the absence of theoretical predictions for the decay $B^0 \to K^+K^-$, which can occur only through W-exchange or W-annihilation diagrams. No reliable estimate for these diagrams exists at this time.

Table 1.4: Theoretical predictions for B decays into the $K\pi, \pi\pi$ final states. Branching fractions are given in 10^{-5} units.

Decay mode	DDGFN	uBSW	CCSYT	DT	KP	EFG	DG
$B^0 \to \pi^+\pi^-$	1.8 ± 0.8	0.71	1.3	–	0.9	0.99	0.8
$B^0 \to \pi^0\pi^0$	0.064 ± 0.032	0.026	0.1	–	0.06	0.028	0.006
$B^+ \to \pi^+\pi^0$	1.4 ± 0.6	0.57	0.6	–	0.8	0.78	0.5
$B^+ \to K^+\bar{K}^0$	–	–	0.1	–	0.13	–	0.07
$B^0 \to K^+\pi^-$	0.65 – 2.4	–	1.7	1.1	1.3	–	1.0
$B^0 \to K^0\pi^0$	0.77 – 0.56	–	0.6	0.5	0.27	–	0.3
$B^+ \to K^0\pi^+$	–	–	1.2	1.1	0.9	–	0.8
$B^+ \to K^+\pi^0$	0.27 – 1.3	–	0.8	0.6	0.94	–	0.7

1.5 Symmetry relations between the amplitudes

In this section we discuss how isospin and SU(3) symmetry can be applied to derive relations between decay amplitudes of the different processes. This approach turns out to be useful for the penguin trapping in $B^0 \to \pi^+\pi^-$ and also can provide a first measurement (estimate) of the angle γ.

1.5.1 Removing penguin pollution in $B^0 \to \pi^+\pi^-$

As it was discussed earlier, the presence of QCD penguins in $B^0 \to \pi^+\pi^-$ decays spoils the clean determination of angle α through Eq. 1.28. Gronau and London [33] proposed to use isospin symmetry to eliminate the penguin contribution, the procedure known as the "penguin trapping".

Consider B^+ and B^0 decays into $\pi\pi$ final states. Since this is a $\bar{b} \to \bar{u}u\bar{d}$ transition, the Hamiltonian has the form

$$H = A_{3/2}\Big|\frac{3}{2},+\frac{1}{2}\Big\rangle + A_{1/2}\Big|\frac{1}{2},+\frac{1}{2}\Big\rangle \ . \tag{1.40}$$

Acting on $|B^+\rangle$ and $|B^0\rangle$ states we get

$$\begin{aligned} H\Big|B^+\Big\rangle &= H\Big|\frac{1}{2},+\frac{1}{2}\Big\rangle \\ &= \sqrt{\frac{3}{4}}A_{3/2}\Big|2,1\Big\rangle + (A_{1/2} - \frac{1}{2}A_{3/2})\Big|1,1\Big\rangle \ , \end{aligned} \tag{1.41}$$

$$\begin{aligned} H\Big|B^0\Big\rangle &= H\Big|\frac{1}{2},-\frac{1}{2}\Big\rangle \\ &= \sqrt{\frac{1}{2}}A_{3/2}\Big|2,0\Big\rangle + \sqrt{\frac{1}{2}}(A_{1/2} + A_{3/2})\Big|1,0\Big\rangle \\ &+ \sqrt{\frac{1}{2}}A_{1/2}\Big|0,0\Big\rangle \ . \end{aligned} \tag{1.42}$$

The final $\pi\pi$ states can be written as

$$\begin{aligned}
\Big| \quad \pi^+\pi^0\Big\rangle &= \Big|2,1\Big\rangle\ , \\
\Big| \quad \pi^+\pi^-\Big\rangle &= \sqrt{\frac{1}{3}}\Big|2,0\Big\rangle + \sqrt{\frac{2}{3}}\Big|0,0\Big\rangle\ , \\
\Big| \quad \pi^0\pi^0\Big\rangle &= \sqrt{\frac{2}{3}}\Big|2,0\Big\rangle - \sqrt{\frac{1}{3}}\Big|0,0\Big\rangle\ .
\end{aligned} \tag{1.43}$$

Note that since there is no final state with $I = 1$, which is prohibited by Bose symmetry, $A_{3/2}$ will produce final states with $I = 2$ only and $A_{1/2}$ will give $I = 0$ final states. That means that three decay amplitudes A^{+0}, A^{+-} and A^{00} defined as

$$A^{ij} \equiv \Big\langle \pi^i\pi^j|H|B^{i+j}\Big\rangle \tag{1.44}$$

can be expressed in terms of only two independent amplitudes , which can be written as

$$A_2 \equiv \frac{1}{2}\sqrt{\frac{1}{3}}A_{3/2,2},\ \ A_0 \equiv \sqrt{\frac{1}{6}}A_{1/2,0}\ . \tag{1.45}$$

We have

$$\begin{aligned}
A^{+0} \quad &= 3A_2\ , \\
\sqrt{\tfrac{1}{2}}A^{+-} \quad &= A_2 - A_0\ , \\
A^{00} \quad &= 2A_2 + A_0
\end{aligned} \tag{1.46}$$

which leads to the triangle relation

$$\sqrt{\frac{1}{2}}A^{+-} = A^{+0} - A^{00}\ . \tag{1.47}$$

A similar triangle can be built for the charge conjugate processes

$$\sqrt{\frac{1}{2}}\bar{A}^{+-} = \bar{A}^{+0} - \bar{A}^{00}\ . \tag{1.48}$$

The crucial point is that penguin diagram doesn't contribute to A_2 and therefore $A^{+0} = \bar{A}^{+0}$ - two triangles share a common base, as can be seen in Figure 1.7. Let's recall that expression for the time-dependent rate asymmetry in the decay

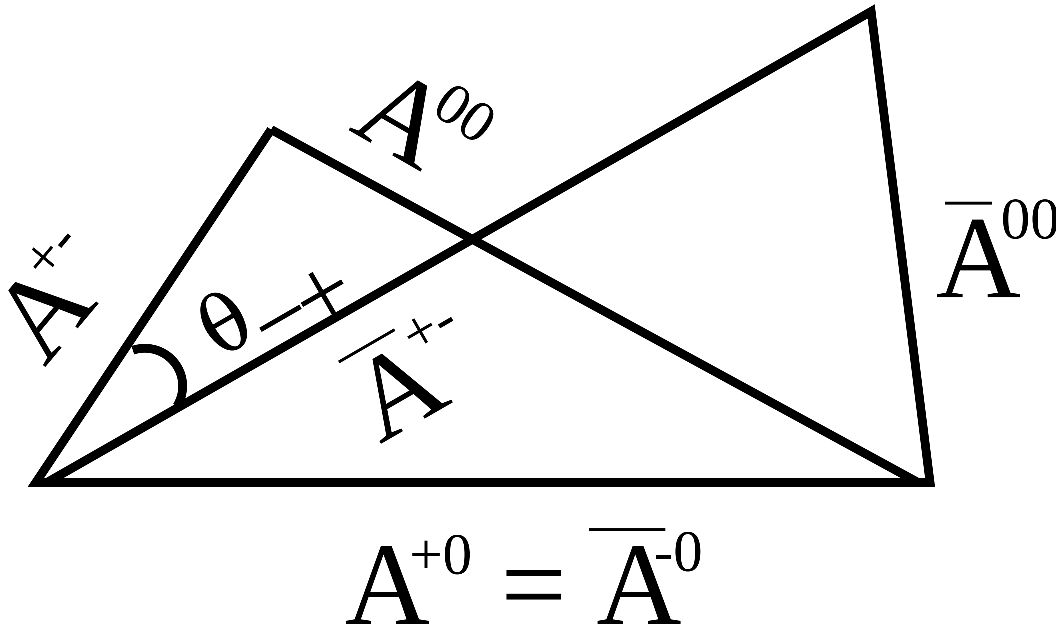

Figure 1.7: Isospin triangles used to resolve the penguin pollution problem in the Gronau-London method.

$B^0 \to \pi^+\pi^-$ contains the term

$$\begin{aligned} -2Im(\frac{q\bar{A}^{+-}}{pA^{+-}})\sin\Delta Mt &= -2Im(exp[-2i(\beta+\gamma)]\frac{\bar{A}^{+-}}{A^{+-}}\sin\Delta Mt \\ &= 2\frac{|\bar{A}^{+-}|}{|A^{+-}|}\sin(2\alpha+\theta_{+-})\sin\Delta Mt\ . \qquad (1.49) \end{aligned}$$

Angle θ_{+-} can be determined from Figure 1.7 after all sides are measured, allowing one to measure α unambiguously.

The major challenge in this method is to measure rates for $B^0 \to \pi^0\pi^0$ and $\bar{B}^0 \to \pi^0\pi^0$. Expected branching fraction for this decay is at most on the order of 10^{-6} and will be very hard to measure.

Besides experimental problems with this method, there is also an additional theoretical complication. We relied on the fact that the QCD penguin is pure $\Delta I = 1/2$ operator, it doesn't contribute to the amplitude A_2 and two triangles share the common base. In other words, it is the absence of direct CP violation in $B^+ \to \pi^+\pi^0$ that allowed us to extract θ_{+-}. However, there are EW penguins which do not respect isospin, since γ and Z couple differently to up- and down-type quarks. The EWP presence changes the orientation of the triangles somewhat, as can be seen in Figure 1.8 [15]. The uncertainty in the α measurement due to EWP presence can be estimated [15] as

$$\Delta\alpha \simeq \frac{1}{2}\Delta\theta \leq \left| \frac{(c_u - c_d)(P_{EW} + P_{EW}^C)}{T + C} \right| \simeq \mathcal{O}(\lambda^2) \qquad (1.50)$$

and can be neglected. Additional discussion of the uncertainties in the extraction of α can be found in the literature [34].

1.5.2 SU(3) symmetry and determination of the angle γ

Given the power of the isospin symmetry as demonstrated above, it is reasonable to ask - can we learn something new by using SU(3) flavor symmetry of the strong interactions [35]. As Gronau, Hernandez, London, and Rosner (GHLR) first pointed out [36], using SU(3) along with several reasonable assumptions, it is possible to derive amplitude relations for B decays into $\pi\pi$, $K\pi$ and KK final states. The

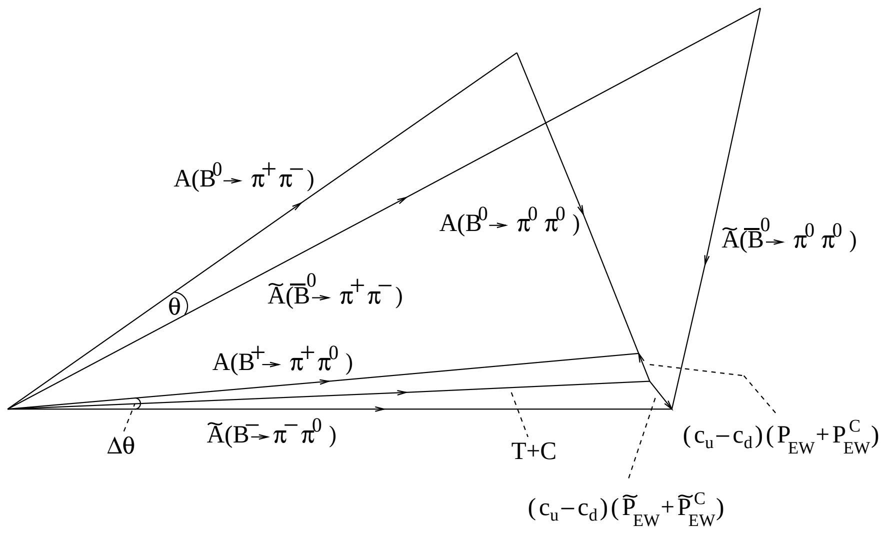

Figure 1.8: Effect of EW penguins on the Gronau-London method of penguin trapping.

attractiveness of these methods is that they may allow measurement of the CKM angle γ using only the decay rates, a quite feasible task for CLEO.

Let us start by describing the original GHRL method [36]. Neglecting the EW penguins for the moment, at quark level there are six different diagrams contributing to $B \to \pi\pi, K\pi, KK$ decays, but they appear in only five independent linear combinations. Furthermore, we will keep only dominant diagrams: "color-allowed" tree (T, T'), "color-suppressed" tree (C, C') and QCD penguins (P, P'). Now, consider decays $B^+ \to \pi^+\pi^0, K^+\pi^0, K^0\pi^+$. Decay amplitudes for these modes can be written as

$$\begin{aligned} \sqrt{2}A(B^+ \to \pi^+\pi^0) &= -(T+C) \ , \\ A(B^+ \to K^0\pi^+) &= P' \ , \qquad (1.51) \\ \sqrt{2}A(B^+ \to K^+\pi^0) &= -(T'+C'+P') \ . \end{aligned}$$

$$(1.52)$$

Using SU(3), we can relate T' and C' to T and C respectively

$$\frac{T'}{T} \simeq \frac{C'}{C} \simeq \lambda \frac{f_K}{f_\pi} \equiv r_u \ , \qquad (1.53)$$

where we took into account factorizable SU(3)-breaking corrections via f_K and f_π. It follows then that decay amplitudes for these processes (and their charge-conjugates) satisfy triangle relations

$$\begin{aligned} \sqrt{2}A(B^+ \to K^+\pi^0) + A(B^+ \to K^0\pi^+) &= r_u\sqrt{2}A(B^+ \to \pi^+\pi^0) \ , \\ -(T'+C'+P') + P' &= -r_u(T+C) \ , \qquad (1.54) \end{aligned}$$

which are drawn in Figure 1.9 and angle γ can be measured. Note that only

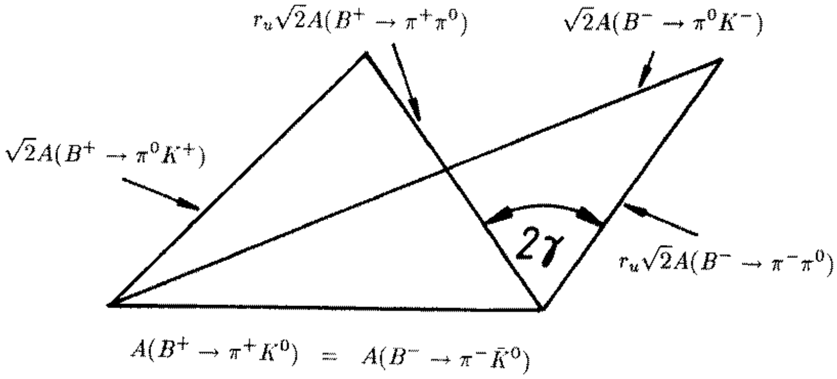

Figure 1.9: The original GHRL method of measuring γ.

charged B decays with relatively large ($\mathcal{O}(10^{-5})$) branching ratios are involved and no time-dependent measurements or tagging are needed.

Despite these attractive features, the GHRL method suffers from theoretical limitations. First, the above relations are not exact and SU(3)-breaking corrections [37] have to be included. While we did introduce factorizable corrections in the form of the ratio of decay constants and form factors, non-factorizable contributions are much harder to estimate at this time. Additionally, EW penguins, which were neglected in the method outlined above, have an important impact on the SU(3) construction, as was first pointed out by Deshpande and He [38]. Taking EW penguins into account, the left side of the Eq. 1.54 becomes [15]

$$-(T' + C' + (c_u - c_d)(P'_{EW} + P'^{C}_{EW})) \ , \tag{1.55}$$

while the right side now is

$$-\lambda(T + C + (c_u - c_d)(P_{EW} + P_{EW}^C)) \;, \tag{1.56}$$

and equality does not hold any longer, since while $T'/T = C'/C \simeq \lambda$, the same is not true for EW penguins: $|P'_{EW}/P_{EW}| = |V_{ts}/V_{td}| \simeq 1/\lambda$

It was proposed in [15] to disentangle EW penguins effects by using additional rare decay modes such as $B_s^0 \to \pi^0\eta$ with branching ratio $\mathcal{O}(10^{-7})$ and quadrangle relations. It is going to be difficult, since B_s^0 mesons are not readily available at e^+e^- machines and hadron collider experiments are not well suited for measurements with neutrals in the final states. Another approach advocated in [39, 40] uses B decays to the $\eta_8 K^+$ final states to construct amplitude quadrangles. Apart from obvious difficulties from $\eta - \eta'$ mixing and SU(3)-breaking corrections, any method using geometrical constructions such as quadrangles will have to deal with discrete ambiguities.

To conclude this section we will mention one more method of fixing γ, originally proposed by Fleischer [41]. Let us consider decays $B_d^0 \to K^+\pi^-, B^+ \to K^0\pi^+$ and their charge-conjugates. For these modes only color-suppressed EW penguins contribute and we'll neglect their contribution. Corresponding decay amplitudes can be written as

$$\begin{aligned} A(B^+ \to K^0\pi^+) &= P' = A(B^- \to K^0\pi^-) \;, \\ A(B_d^0 \to K^+\pi^-) &= -(P' + T') \;, \\ A(\overline{B_d^0} \to K^-\pi^+) &= -(P' + e^{-2i\gamma}T') \end{aligned} \tag{1.57}$$

and imply triangles shown in Figure 1.10. T' can be determined from $B^+ \to \pi^+\pi^0($

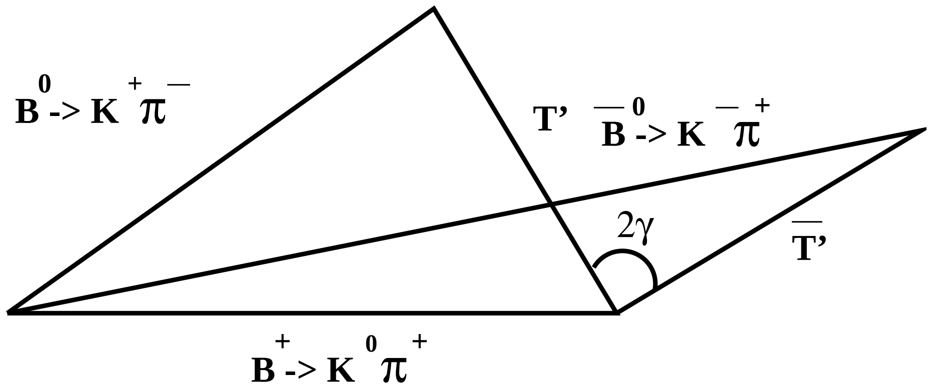

Figure 1.10: Fleischer's method of measuring γ.

see Eq. 1.53) neglecting the color-suppressed amplitude C and taking into account SU(3) breaking. Another alternative is to get $|T'|$ from the lattice calculations. Reliance on the knowledge of $|T'|$ is probably the weakest point of this method, which remains quite attractive otherwise.

1.5.3 How to control EW penguins

Since it is quite obvious that EW penguins play an important role for the class of decays we are dealing with, it is desirable to determine their contributions experimentally. A detailed review of the subject is available [16], here we will simply outline possible approaches.

The decay $B^+ \to \pi^+\phi$ is an interesting possibility, because it is expected to be dominated by the EW penguins [42]. The predicted branching ratio however is of the order of $\mathcal{O}(10^{-8})$ and is unlikely to be measured soon. An alternative approach is to compare decay rates for the processes $B^+ \to K^+\pi^0$ and $B^0 \to K^+\pi^-$ [15].

The amplitudes are given by

$$\sqrt{2}A(B^+ \to K^+\pi^0) \simeq -[T' + P' + (c_u - c_d)P'_{EW}],\ A(B^0 \to K^+\pi^-) \simeq -[T' + P'], \tag{1.58}$$

where color-suppressed amplitudes were dropped. Therefore, deviation of the ratio $2\Gamma(B^+ \to K^+\pi^0)/\Gamma(B^0 \to K^+\pi^-)$ from one will signal significant presence of EW penguins. The ratio $2\Gamma(B^0 \to K^0\pi^0)/\Gamma(B^+ \to K^0\pi^+)$ can be used in the same way.

1.6 New physics

In the previous sections we described how CP violation can be accommodated in the SM. Apart from being interesting in its own, CP violation provides a very promising direction in the search for the new physics beyond the SM.

Given that only one CP violating effect has been observed so far and the CKM phase accounts for CP violation in the SM, existing measurement can only fix (constrain, to be more precise) the value of the phase, but can't prove that this is the only source of CP violation. Meanwhile, there are quite a few arguments that there can (should) be additional sources of CP violation:

- The observed baryonic asymmetry of the Universe or, in other words, mere existence of matter, requires CP violation for dynamic generation. It was widely discussed recently (see [4] for a review) that CKM-based CP violation in the SM produces baryon asymmetry smaller by many orders of amplitude.

On the other hand, many SM extensions produce new sources of CP violation capable of reproducing cosmological observations.

- CP violation can occur in the strong sector of the SM, via the so called θ_{QCD} term. However, extreme fine-tuning of $\theta < 10^{-9}$ is required in order not to violate the current experimental limit on the neutron electric dipole moment [43]. Extending the SM [44, 45] can solve this problem.

- Almost any extension of the SM involves new sources of CP violation. Since there is a pretty good chance that the SM is not the "final" theory, new CP violating effects might disagree with the SM predictions, shedding light on the presence of the new physics.

It is very likely that the SM as we know it is merely an effective theory of a kind, a low energy approximation of the "true", full theory of matter. We don't know the exact nature of this true theory, but we hope that it will manifest itself at the low energy scale through CP violation or a decay rate inconsistent with the SM picture. To discover new physics in rare B decays we have to look for deviations from the SM predictions. Given current large theoretical uncertainties for the rates of the processes, it is safe to assume that only huge deviations from the SM expectations for the decay rates will be a convincing evidence for the new physics. On the other hand, if one finds sizeable CP asymmetries in the decays where the SM doesn't expect them, for instance $B^+ \to \pi^+\pi^0$ or $B^+ \to \pi^+K^0$, this will be a very strong indication of the presence of the non-SM decay amplitudes.

For detailed discussion of CP violation in the B system in different SM extensions see for example recent reviews by Gronau and London [46] or Grossman, Nir and Ratazzi [47].

1.7 Conclusions

In this chapter we presented a brief overview of the rich physics accessible by studies of the rare charmless hadronic decays of the B meson. Future experiments will attempt to probe the CKM angle α via time-dependent measurement of the $B^0 \to \pi^+\pi^-$. This decay mode has not been seen yet and its observation will be an important achievement. Since penguin pollution can pose a serious problem for the clean extraction of α, it is important to obtain experimental information about the size of the penguin amplitude in this decay. We hope to estimate the size and importance of the penguin amplitude through the studies of penguin-dominated modes such as $B^0 \to K^+\pi^-$ and $B^+ \to \pi^+K^0$. In the case when the penguin contribution to $\pi^+\pi^-$ cannot be neglected, it will be necessary to perform an isospin analysis by measuring additional decay rates of $B^+ \to \pi^+\pi^0$ and $B^0 \to \pi^0\pi^0$ and their charge conjugate modes. It is also possible to extend the isospin symmetry argument to the SU(3) case and construct triangle relations between various $B \to K\pi, \pi\pi$ amplitudes, which in principle can allow extraction of the angle γ of the unitarity triangle. These methods are especially attractive to CLEO, since no time-dependent measurements are required. The presence of EW penguins can affect the measurement of γ in this fashion and it's necessary to provide experimental estimates of the size of the EW penguins. It is worthwhile to look for direct CP violation in the modes where it is predicted in the SM ($K^+\pi^0,\ K^+\pi^-$), but also in the modes where it should be absent ($\pi^+\pi^0,\ \pi^+K^0$). Any significant asymmetry in the latter decays will signal the presence of physics beyond the SM.

Finally, exclusive measurements of the charmless non-leptonic decays will provide much needed experimental input for the existing theoretical models.

CHAPTER 2

CLEO AND CESR

Detailed studies of B physics require large number of B mesons. The Cornell Electron Storage Ring (CESR) produces B mesons by running on the $\Upsilon(4S)$ resonance at the center of mass energy of 10.58 GeV(see Fig. 2.1). $\Upsilon(4S)$ is the first res-

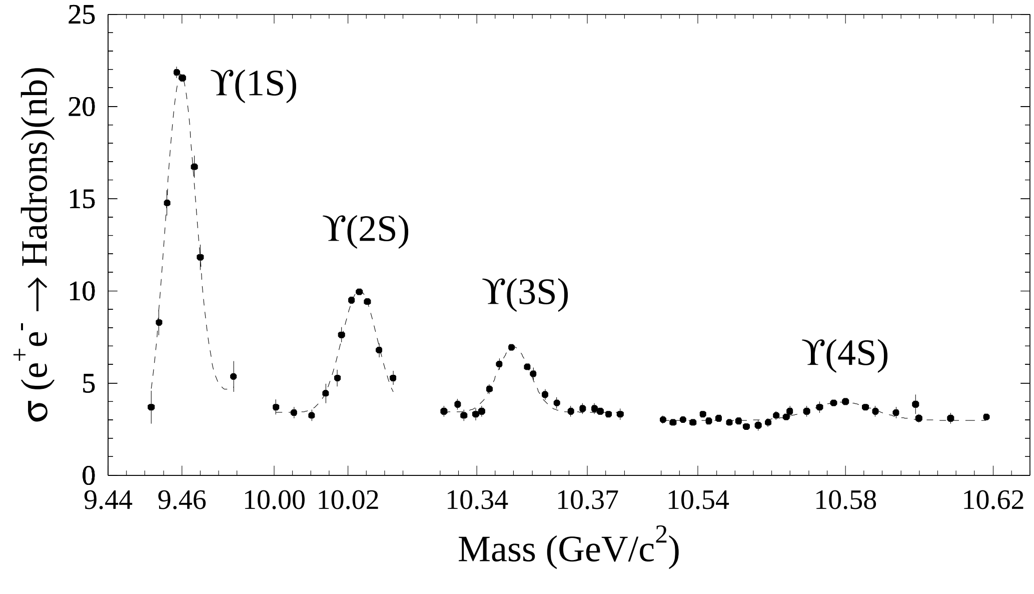

Figure 2.1: Family of the Υ resonances observed in the e^+e^- collisions.

onance above the B meson production threshold, decaying 100% to a pair of B

mesons, B^+B^- and $B^0\overline{B^0}$ in approximately equal proportions. The $B\bar{B}$ production cross-section at the peak of $\Upsilon(4S)$ is 1.07 nb, translating approximately into one million $B\bar{B}$ events for every fb^{-1} of integrated luminosity collected. Thanks to the record luminosity of CESR, CLEO currently has the largest sample of analyzed $B\bar{B}$ events in the world, 3.3×10^6 and growing.

This chapter is organized as follows. We begin with a brief discussion of CESR and continue to describe CLEO II detector. A separate section is devoted to the new detector subsystem installed in 1995 - Silicon Vertex Detector (SVX), which marked the beginning of CLEO II.V era. In the end we'll discuss near and long term prospects for the B physics experiments.

2.1 CESR

CESR is a circular electron-positron collider located on the Cornell University campus. A schematic of CESR is shown in Figure 2.2. Bunches of electrons and positrons travel in opposite directions in the same vacuum chamber, colliding only in one interaction point inside the CLEO detector. The Cornell High Energy Synchrotron Source (CHESS) laboratory uses the synchrotron radiation emitted by electron and positron beams to conduct experiments in physics, biology, chemistry, and materials science.

The major parts of CESR are the linear accelerator, synchrotron, and storage ring. The linear accelerator (linac) produces both electrons and positrons and provides first stage acceleration. Electrons are emitted from the cathode, grouped into

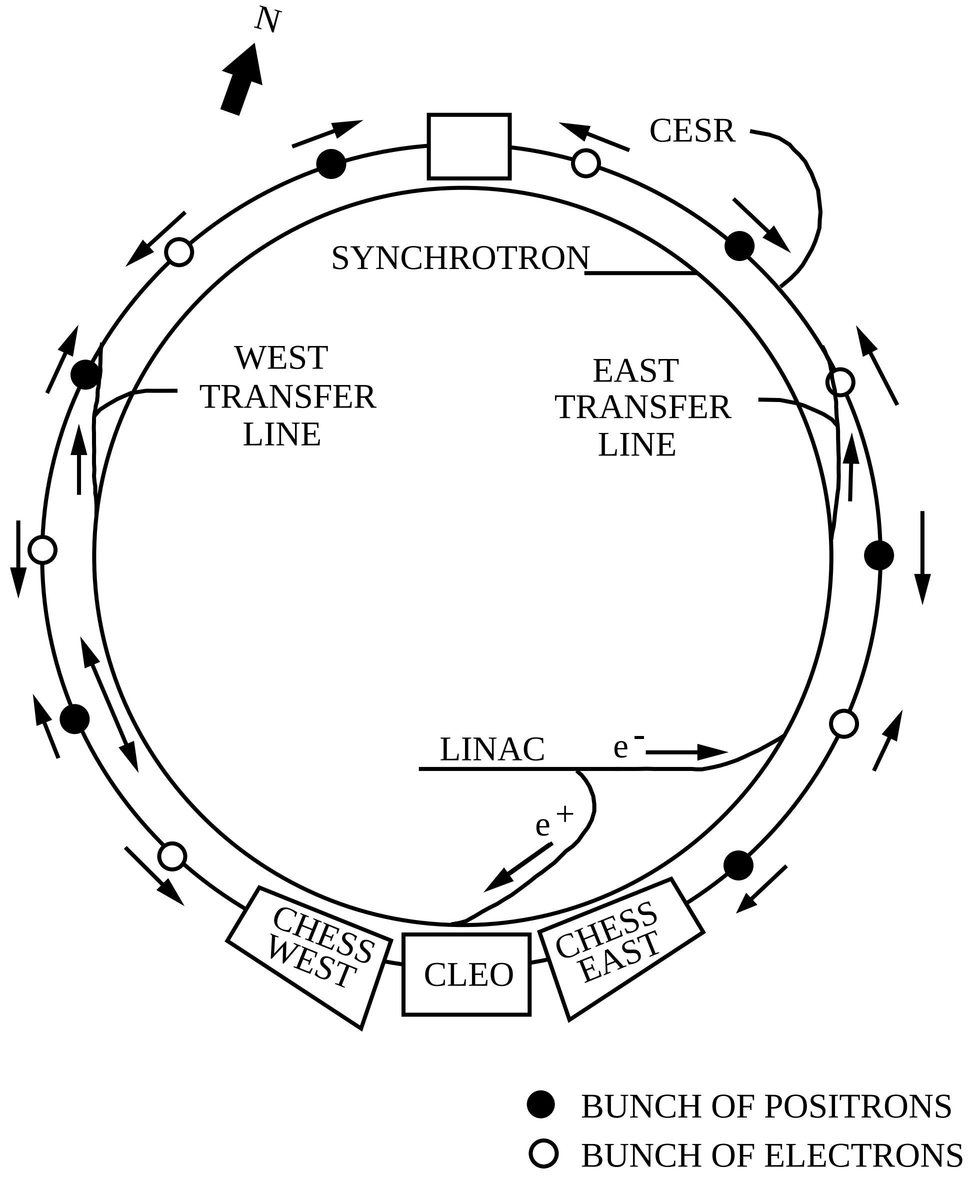

Figure 2.2: “Bird’s-eye” view of CESR

bunches and accelerated in the 30 m straight section up to their final energy of 200 MeV. Positrons are produced in the intermediate point in the linac by placing a tungsten target in the way of 150 MeV electrons. As a result of the electron's interaction with the target an electromagnetic shower containing positrons is produced. Positrons are then selected, bunched and accelerated in the remaining length of the linac.

At the end of the linac electrons or positrons are injected into the synchrotron, where they are accelerated to their final energy of 5.29 GeV by repeatedly passing through several RF cavities. After about 4,000 revolutions, when the desired energy is reached, electrons (positrons) are transferred into the storage ring. This acceleration cycle has a frequency of 60 Hz and is repeated until the necessary current has been stored. Typical currents at the time of this writing are on the order of 150 mA per beam and the storage cycle takes approximately 10 minutes.

Once stored, bunches of electrons and positrons are brought into collision at the interaction point (IP) inside the CLEO detector. Storing many bunches in CESR has distinct advantage of higher luminosity, but poses a problem of avoiding unnecessary collisions at places other than the IP. CESR solves this problem by employing the so called "pretzel" scheme, separating electron and positron orbits at the parasitic crossing points. With this scheme it was possible to store 7 bunches in the machine and achieve a luminosity of $2.0 \times 10^{32} cm^{-2} s^{-1}$. Further increase in the luminosity was gained through the implementation of the "crossing-angle" scheme, shown in Figure 2.3. The idea is to collide "trains" of closely spaced bunches (separated by as little as 14 ns) at a small ($\sim 2mr$) angle at the interaction region.

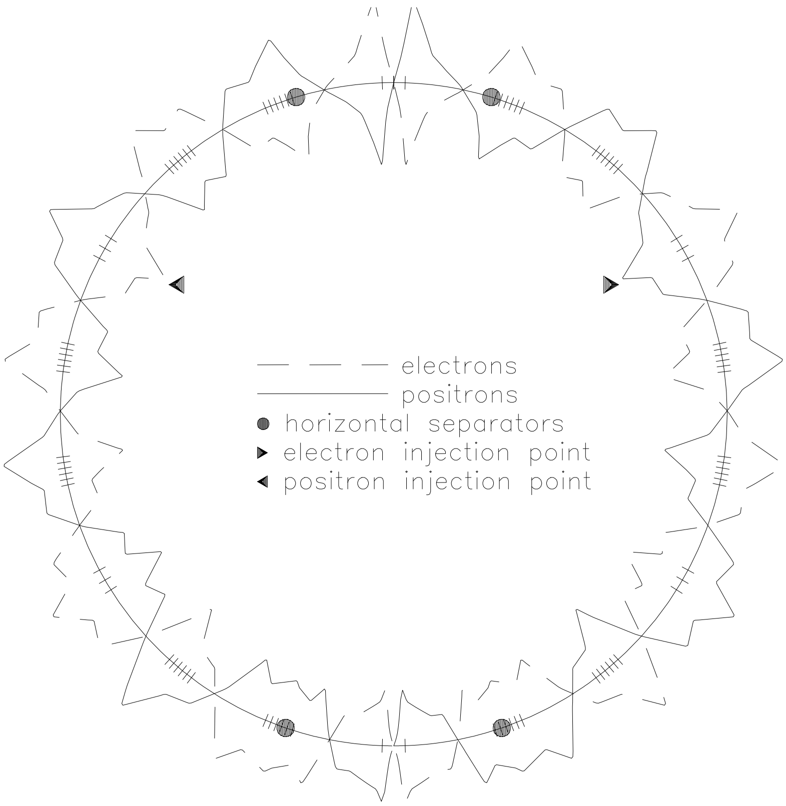

Figure 2.3: Crossing angle scheme for CESR.

The crossing angle scheme avoids parasitic crossings in the immediate vicinity of the IP and relies on "pretzels" to separate beams elsewhere in the machine. The current record of instantaneous luminosity of $4.1 \times 10^{32} cm^{-2} s^{-1}$ was achieved with 9 trains of two bunches separated by 28 ns within the trains.

While particles spend only about a hundredth of a second inside the synchrotron, their lifetime inside the storage ring is usually about an hour. Since they lose approximately 1.5 MeV of energy per turn due to the synchrotron radiation, these energy losses have to be compensated with the additional RF system in the storage ring. The ability of the present RF system to deal with high beam currents is at the moment one of the factors limiting luminosity. Installation of the new superconducting RF cavities in 1997-1998 should further boost CESR luminosity.

2.2 CLEO II detector

2.2.1 Overview

In order to study B mesons, we have to be able to reconstruct products of their decay with maximal efficiency and precision. CLEO II is a 4π detector with excellent capabilities both for charged tracks and photons [48]. A diagram describing CLEO II detector elements is shown in Figure 2.4

Three tracking chambers placed inside the 1.5 T superconducting solenoid measure momenta of the charged particles. Outside the tracking volume decay products encounter time-of-flight scintillating counters and the electromagnetic calorimeter.

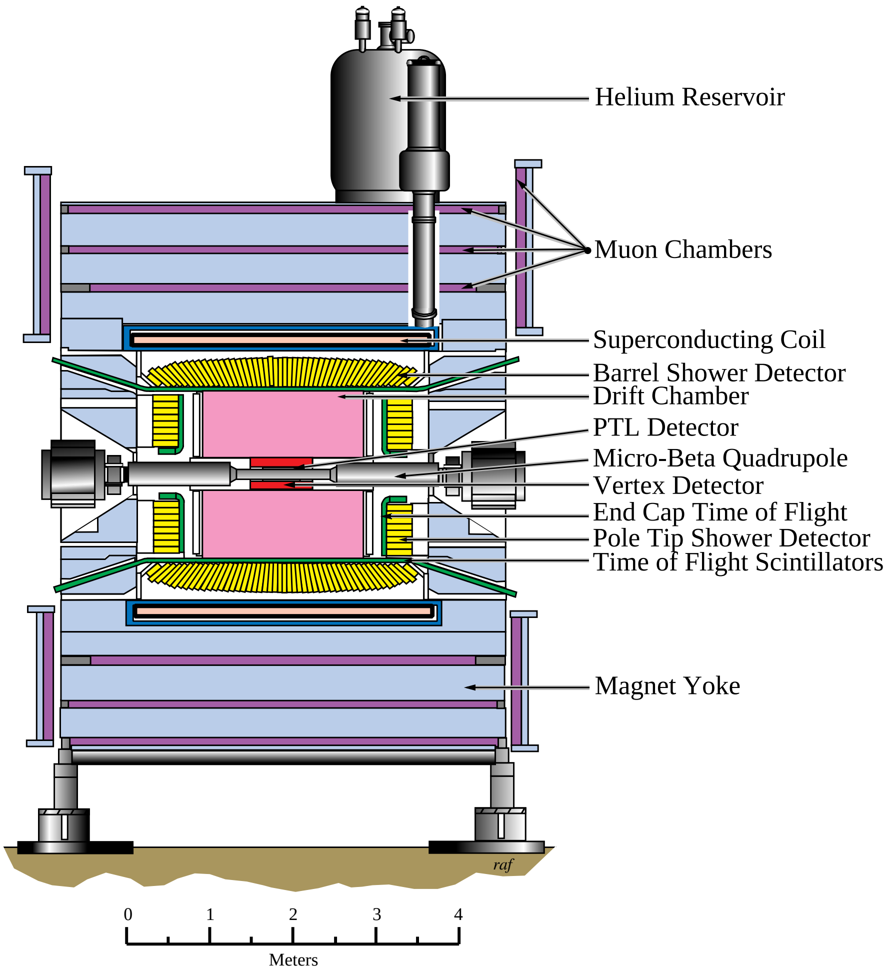

Figure 2.4: The CLEO II detector.

Based on CsI crystals, the calorimeter provides very good energy and coordinate measurements for the photons. The flux-return iron yoke is instrumented with tracking chambers to identify muons. A sophisticated trigger and data acquisition system enables the CLEO II detector to recognize and record events with interesting physics, while suppressing unwelcome backgrounds. In the subsequent sections we provide a description of the detector elements most relevant for our analysis.

2.2.2 Tracking system

The tracking system in CLEO II consists of three concentric cylindrical wire drift chambers measuring the momentum and direction of charged tracks. Track reconstruction is achieved by detecting the ionization trail left by the charged particle traversing the gas-filled volume subdivided into many drift cells. By knowing the coordinates of the wires which were "hit" and the time it took for the ionization to reach the particular wire, it is possible to precisely measure track parameters. For a detailed review of the tracking chamber operating principles see [49, 50].

The precision tracking layer (PT) has six longitudinal wire layers with radius from 4.7 to 7.2 cm. This is the device closest to the 3.5 cm beam-pipe and it provides the most precise measurement of the coordinate resolution ($r-\phi$ plane only). It is crucial for the accurate measurement of the track directions and detection of the secondary vertices. Each layer is made of 64 Mylar tubes which define the drift cell for the signal wires in the center of the tubes as can be seen in Figure 2.5.

The intermediate drift chamber, known as the vertex detector (VD) is a 10-layer wire chamber, also shown in Figure 2.5. 800 sense wires and 2272 field wires

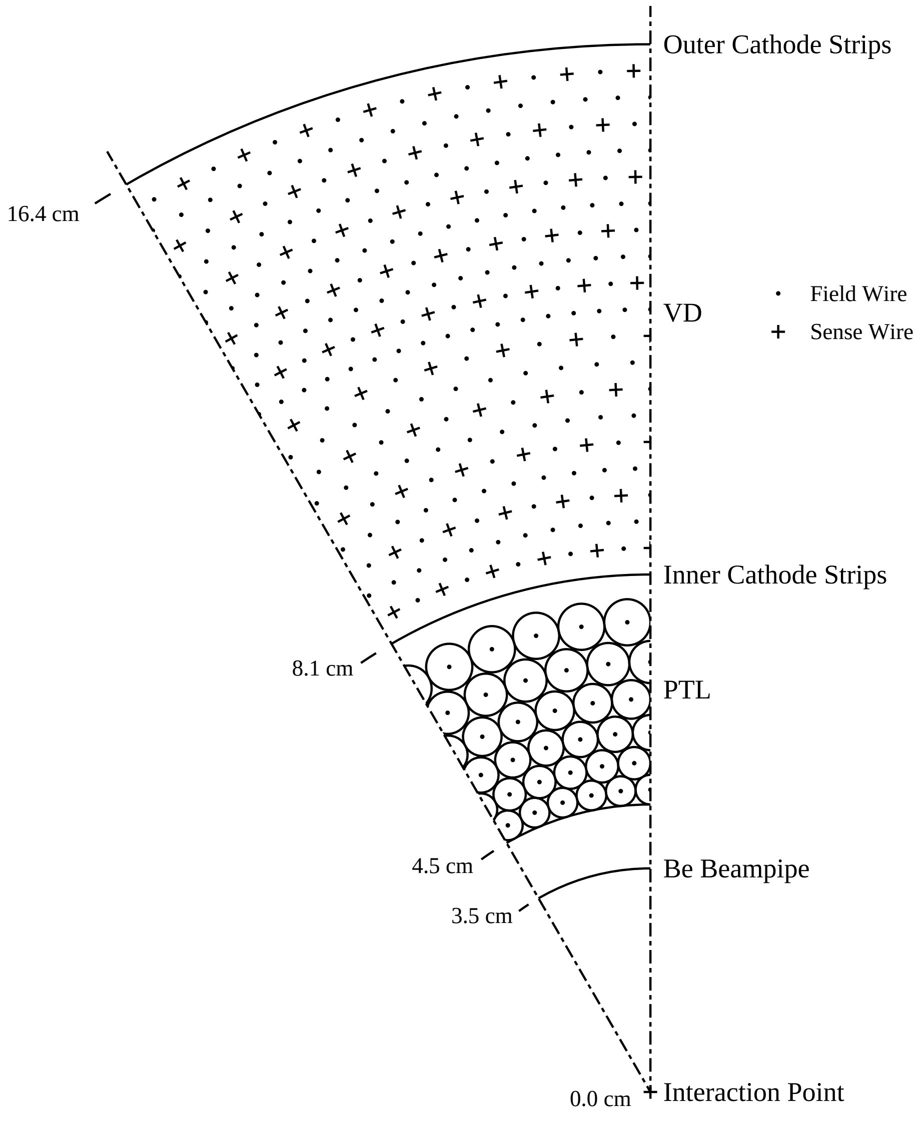

Figure 2.5: PT and VD .

form layers of hexagonal cells. Cells in the adjacent layers are staggered by a half of the cell width to resolve left-right ambiguities in the drift distance measurements. For the innermost and outermost layers the field shaping is provided by the segmented cathode surfaces shown in Figure 2.6. Segmentation of the cathode

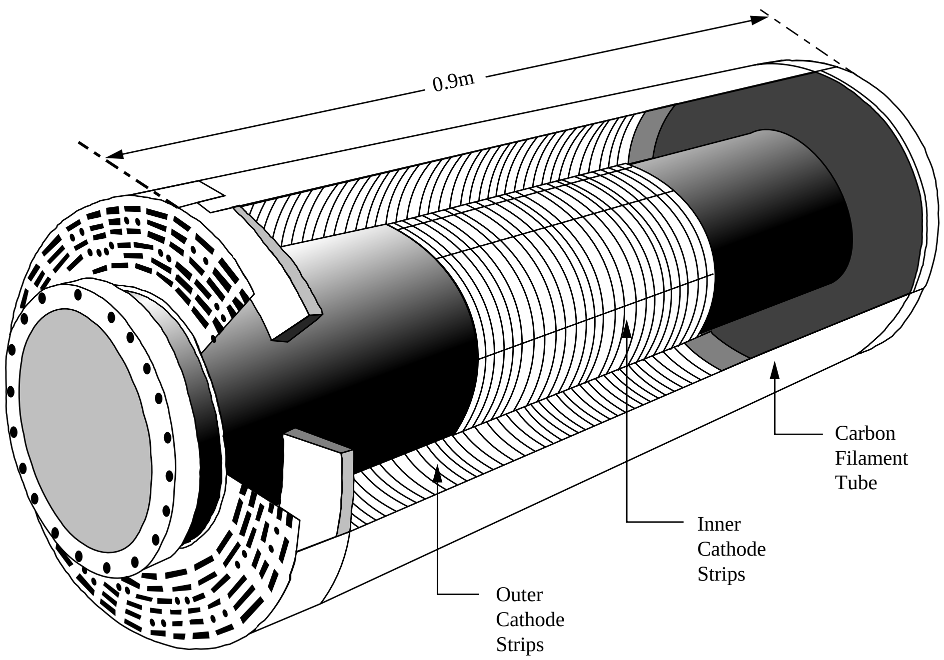

Figure 2.6: VD cathodes.

pads in z and ϕ allows the imaging of the avalanche from the nearby signal wires and provides a z coordinate measurement. Additional z information is obtained by using high resistance nickel-chromium signal wires instrumented for the charge division measurements.

The main drift chamber (DR) has 12,240 sense wires and 36,240 field wires arranged in the pattern of 51 layers of cells as illustrated in Figure 2.7. 40 axial layers provide information about track parameters in the $r-\phi$ plane, while 11 stereo layers with slanted sense wires measure longitudinal track parameters. Segmented inner and outer cathode pads also contribute to the z coordinate measurements.

Tracking chambers are able to measure tracks in the polar angle range of $|\cos\theta| < 0.9$. However, for tracks with $|\cos\theta| > 0.71$ the momentum and angular resolutions begin to deteriorate due to the smaller number of layers traversed by the particle. Transverse momentum resolution is determined by two factors. The first comes from the error in the curvature measurement due to the individual measurement errors in drift distances. The second is due to the deviation of track from the perfect helix, caused by the multiple scattering. Measured resolution for high momentum tracks in CLEO II can be parameterized as [51]

$$(\delta p/p)^2 = (0.0017p)^2 + (0.005)^2. \tag{2.1}$$

2.2.3 Calorimetry

The CLEO II electromagnetic calorimeter is based on the thallium-doped CsI scintillating crystals read out by the photodiodes. Its main goal is to provide uniformly good energy and coordinate resolution for the photons in the wide energy range (30 to 5000 MeV). There are 7800 crystals in total, 6144 in the barrel and 1656 in the endcaps. The crystal size of approximately $5 \times 5 \times 30$ cm is a compromise be-

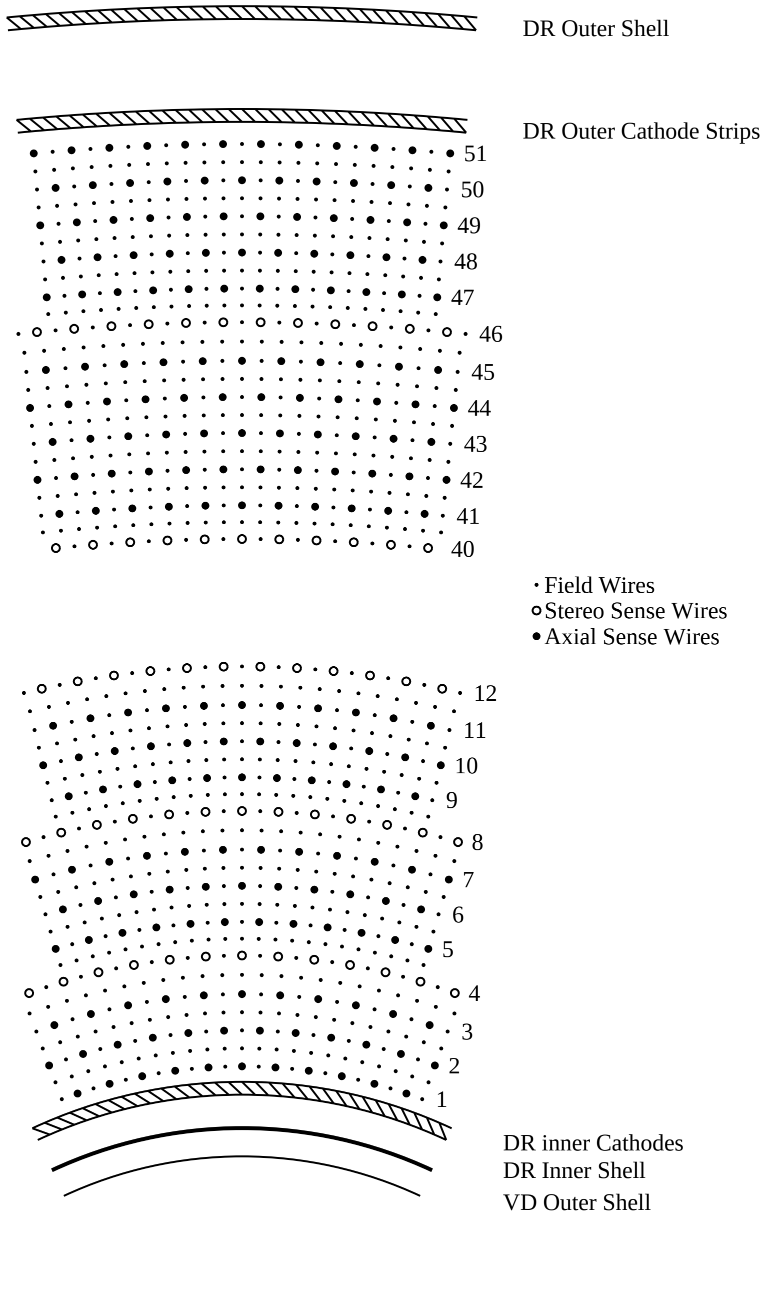

Figure 2.7: Drift chamber.

tween cost and performance. Longer crystals would have better energy resolution for high energy photons, where it is dominated by the longitudinal leakage. However, longer crystals cost more and light output uniformity is more of a problem, leading to poor energy resolution at low energies. Smaller lateral dimensions are beneficial for the coordinate measurements, but increased number of the readout channels in the system leads to higher cost. Energy resolution, especially at the low energies would also suffer, as number of crystals to be included in the sum goes up, increasing electronics noise contribution.

Each crystal is read out by 4 photodiodes, whose output is amplified, mixed, shaped and digitized, resulting in one ADC value per crystal. The calorimeter is calibrated using a wide variety of processes such as $e^+e^- \to e^+e^-, e^+e^-\gamma$ and π^0's to obtain crystal-to-crystal variations and the absolute energy normalization. Achieved energy resolution can be parameterized as

$$Barrel : \frac{\sigma_E}{E}(\%) = \frac{0.35}{E^{0.75}} + 1.9 - 0.1E \ , \tag{2.2}$$

$$Endcap : \frac{\sigma_E}{E}(\%) = \frac{0.26}{E} + 2.5 \ , \tag{2.3}$$

where E is measured in GeV. The degraded energy resolution for the endcaps is explained by the large amount of passive material in front of the crystals. For this reason, when reconstructing π^0 we require at least one photon to be in the good barrel region.

2.2.4 Particle identification

The particle identification in CLEO II uses time-of-flight (TOF) scintillating counters and specific ionization loss measurements in the drift chamber.

The time-of-flight system uses fast plastic scintillators to measure the velocity of the charged tracks. Combined with the momentum measurement in the drift chamber, it is possible to discriminate between particles with different masses, such as kaon and pion for example. Achieved time resolution of 140 ps allows good particle identification with the TOF system up to a track momentum of 1 GeV/c.

The other method relies on the fact that ionization loss per unit of path length, called dE/dx, is velocity dependent. Therefore, measuring pulse heights of the hits in the drift chamber, it is possible to distinguish kaons from pions etc. For a particular particle hypothesis the variable σ_{hyp} is defined:

$$\sigma_{hyp} = \frac{(dE/dx)_{meas} - (dE/dx)_{hyp}}{\sigma} \tag{2.4}$$

where σ is the expected resolution. dE/dx measurements are calibrated to ensure unit Gaussian distribution of σ_K for kaons, σ_π for pions etc.

2.2.5 Muon system

Muons are identified by three layers of the barrel muon chambers [53] embedded in the iron of the flux return yoke and additional chambers covering the endcaps. Total effective depth of the iron absorber varies between 7.2 and 10 nuclear absorption lengths, depending on the incidence angle of the track. Muon system covers 85% of the solid angle and provides an effective tool for selecting or rejecting muons, depending on the analysis.

2.2.6 Trigger and data acquisition

As we noted in the beginning of this chapter, the $B\bar{B}$ production cross section at the peak of the $\Upsilon(4S)$ resonance is only 1.07 nb. Combined with the current peak CESR luminosity of $4 \times 10^{32} cm^{-2} s^{-1}$, we find the $B\bar{B}$ event rate is at most 0.4 Hz. Other processes of interest to CLEO, such as tau and charm production and two-photon physics have comparable contributions. At the same time other processes, from e^+e^- interactions and from beam-gas, beam-wall events occur at a much higher rate. In order to select interesting events a four-level trigger system was implemented [52]. The first three levels (L0, L1, and L2) are hardware based and are shown in Figure 2.8. L0 uses the fastest detector subsystems, TOF counters and VD, to make a decision within a 400 ns interval whether to keep event or throw it out. A positive L0 decision disables data taking and additional detector information is made available for L1 and L2. L1 makes a decision within approximately 1 μs, while L2 takes almost 50 μs. The L0 output rate is on the average 20 kHz, compared to the input rate of 3 MHz. A level 2 positive decision results in the readout of the whole detector and is limited by the current data acquisition system maximal throughput of 50 Hz. At this stage the Level 3 software trigger has information from all of the detector subsystems and further rejects background to reduce the amount of data written to disk.

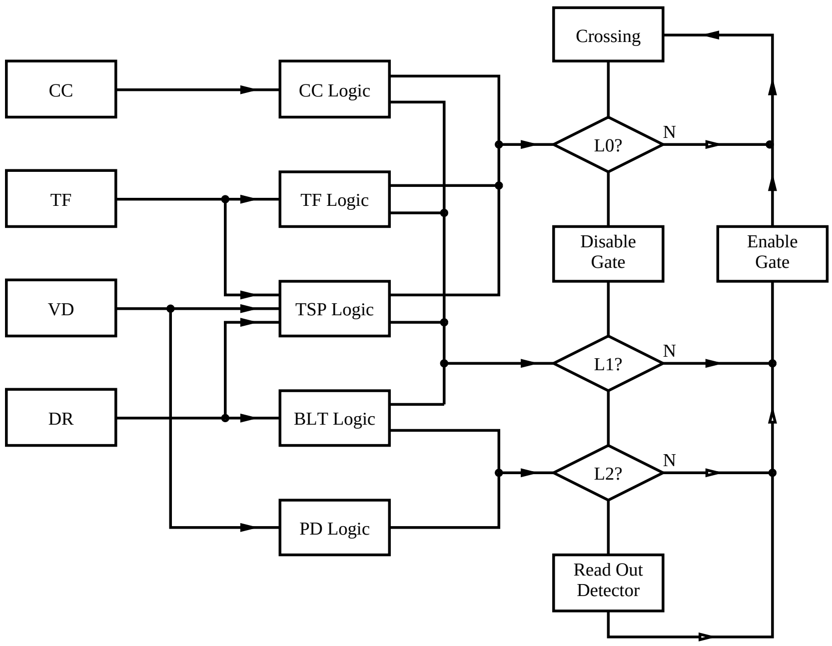

Figure 2.8: CLEO II trigger.

2.3 SVX

In the fall of 1995 the PT tracking chamber was replaced by the Silicon Vertex Detector (SVX), shown in Figure 2.9. The very high intrinsic resolution of the SVX greatly improves the vertexing capabilities of the CLEO II detector, allowing better separation of the secondary vertexes from charm and τ production. Resolution in the z coordinate measurement for tracks is improved by at least one order of magnitude. The high granularity of the SVX also helps pattern recognition and track reconstruction efficiency.

The SVX is a three-layer tracker with octagonal symmetry. It covers a solid angle region of $|cos\theta| < 0.92$. The SVX has 96 detectors arranged in 8 octants. These octants overlap in azimuth in each layer to ensure full coverage and facilitate detector alignment with tracks. Both the $r - \phi$ and z measuring sides are read out at the ends of the wafers, removing all electronics from the tracking volume. Layers 1 and 2 use single-length detectors, while layer 3 detectors are made from two wafers which are glued and wire-bonded at the ends. The total number of channels in the detector is 26,208.

The SVX uses 300 μm double-sided silicon microstrip detectors manufactured by Hamamatsu Photonics [54]. A cross section of a wafer is shown in Figure 2.10. The $r - \phi$ side (p-side) has an implant pitch of 28 μm with every fourth strip being read out. Charge deposited on the unbonded strips is collected through the interstrip capacitance. z side implants have 105 μm pitch and every strip is read out with the help of additional aluminum readout traces, on top of and orthogonal

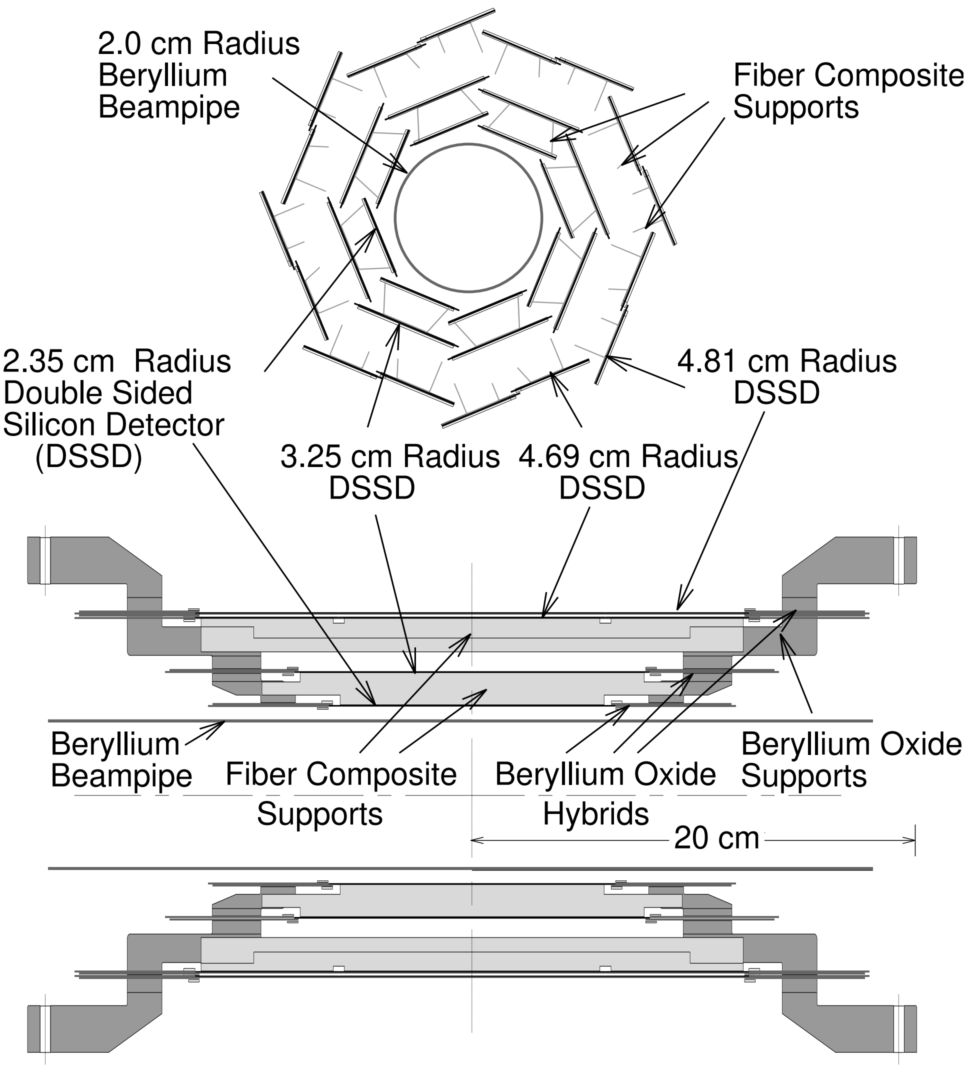

Figure 2.9: CLEO II Silicon Vertex Detector.

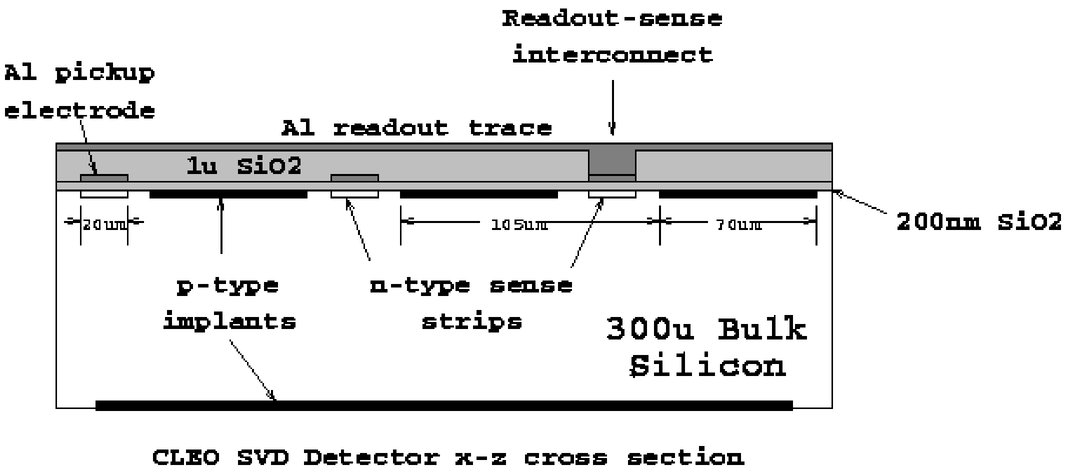

Figure 2.10: Double-sided Si detector.

to the z sensitive strips. Since the aspect ratio of the wafer is roughly 1:3, each readout trace on the z side is connected to three sense strips. This results in a 3-fold ambiguity in layers 1 and 2, and a 6-fold ambiguity in layer 3 for the z coordinate reconstruction. Expected resolutions are 12 μm and 30 μm for the $r-\phi$ and z sides respectively. Detectors have integrated AC coupling capacitors on both sides, formed by a thin insulating layer between the implant and readout trace. Imperfections in this layer, known as pinholes, can make the channel unusable. At the time of this writing, the SVX bad channel rate is approximately 6%. Detectors also feature polysilicon bias resistors on the n-side and punch-through resistors on the p-side. Wide p-type implants are used to isolate n-type strips on the n-side.

The SVX is mounted on the new 2 cm radius beryllium beam-pipe. It has two 0.25 mm walls separated by a 0.5 mm gap for water cooling. The inner surface is sputtered with a thin layer of gold for synchrotron radiation absorption. To minimize multiple scattering in the SVX, low mass, low Z material support is a necessity. The SVX uses kevlar U-channels to support detectors within the octants. Beryllium oxide pillars suspend detector ladders from the carbon fiber tubes, known as clamshells. The BeO provides a good thermal pathway for approximately 100 W of heat generated by the readout electronics. Detectors are read out by the CAMEX64 and JAMEX64 (layer 3 n-side only) chips, both developed at MPI-Munich [55]. These chips are mounted on BeO hybrids manufactured by Pacific Microelectronics. All readout signals are generated externally and brought to the hybrids via kapton flexible circuits.

Assembly of the SVX was done at the University of California at Santa Barbara. Pairs of layer 3 wafers were glued, wire-bonded and encapsulated to make a double-length detector. Hybrids were glued to the detectors forming the detector module. The wafer was wire-bonded to the preamplifier die on the hybrid and all known pinhole channels were disconnected. After this step all detector modules were tested for functionality with an infrared pulser and kept in a storage facility with detectors biased and hybrids powered for a burn-in test. Tested detector modules were glued to kevlar beams and beryllium oxide supports to make an octant. Produced octants were surveyed and tested prior to the installation into the clamshell. Two assembled clamshells were then shipped to Cornell for the final testing and installation.

The SVX has to withstand significant doses of radiation during its lifetime. Our previous studies [56] showed that powered CAMEX chips begin to fail after a dose of more than 20 kRad has been accumulated. The task of radiation protection and monitoring is therefore very important. The “moving shields” system [57] illustrated in Figure 2.11 protects SVX electronics against synchrotron radiation during the CESR injection. The fixed tungsten shields are glued to the beam-pipe,

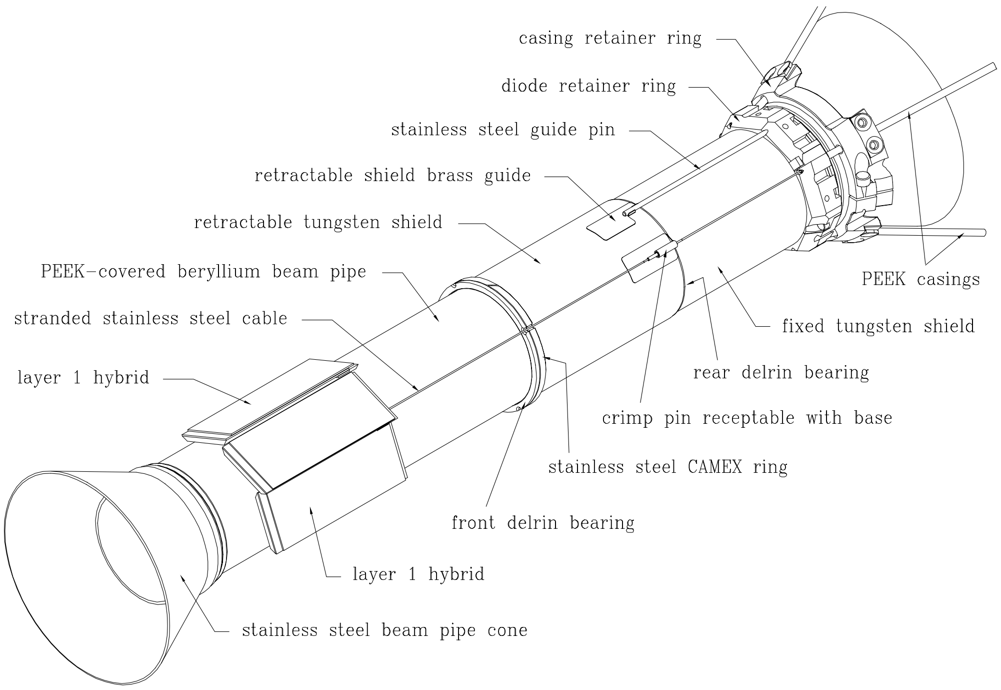

Figure 2.11: Retractable shields.

while the retractable shields are pulled open or closed by the stainless steel cables, activated by the stepping motors. We measure radiation dose received by the SVX with the help of PIN diode based radiation monitors. There are 24 such diodes in total, 12 on the east side of detector and 12 on the west, evenly spaced in azimuth around the beam-pipe. In order to minimize radiation damage to the CAMEX chips, they are left unpowered during CESR injection. JAMEX chips, used for layer 3 readout, are less exposed to the synchrotron radiation and are relatively radiation hard. Since they also consume more power than CAMEXes, they are kept powered all the time to minimize temperature fluctuations in the system.

2.3.1 SVX DAQ

The data acquisition system for SVX is probably the most complicated in CLEO:

1. Number of channels in the SVX is the largest in CLEO.
2. CAMEX/JAMEX chips need a large variety of signals and voltages.
3. The floating ground scheme for SVX electronics, used to reduce stress on AC coupling capacitors.
4. A large "common-mode" component of the detector noise which needs to be subtracted online for proper data sparsification.

A schematic of the SVX DAQ system is shown in Figure 2.12. The outputs of all CAMEX/JAMEX chips are sent via flexible circuits to the receiver boards and from there via flat ribbon cables to the Sequencer-CAMEX-Interface (SCI) crate. We "float" the hybrid ground by keeping it close to the detector bias voltage. This approach prevents the development of new pinholes. The SCI crate defloats chip outputs and floats all control signals going into the hybrids. This crate also fans out DC voltages from the SVX power supplies to the chips. Defloated outputs go to 16 databoards in the SVX VME crate where they are digitized and stored in the FIFO memory. A VME 68040-based CPU on each databoard reads the FIFO, calculates

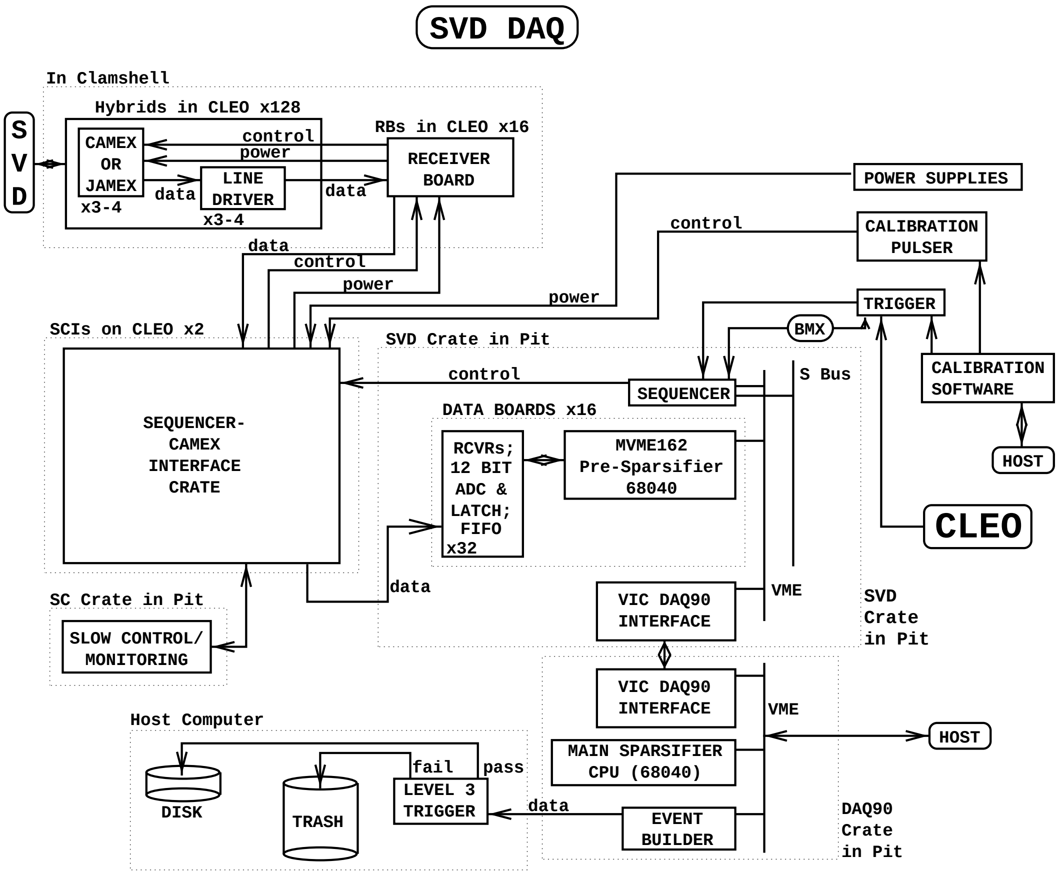

Figure 2.12: Diagram of the SVX DAQ.

and subtracts the common-mode noise and performs sparsification, reducing the amount of data by approximately a factor of 25. Event fragments from each databoard are collected by the master board in the SVX VME crate. This master board then assembles the SVX event and sends it to the main CLEO DAQ crate, where it is incorporated into the CLEO output data stream. The SVX DAQ system in stand-alone mode is able to handle event rates up to 60 Hz, which is quite adequate for CLEO II conditions.

The timing diagram of the SVX readout is shown in Figure 2.13. In the asynchronous mode of operation we are constantly updating the state of the internal capacitors with S-pulses, storing at any given time a short history of charge flow into the amplifier. When a trigger arrives, the R2 switch is opened and three samples of the baseline-subtracted charge are summed and stored for the subsequent readout. L0 trigger pauses the S-pulses to prevent the loss of the potentially interesting signal and we wait for the L1 to open the R2 switch.

An elaborate slow control system monitors voltages, currents and temperatures, over 2000 quantities in total. In case of a serious problem the system shuts down the power supplies to prevent damage to the SVX.

Figure 2.14 shows a typical "hadronic" event, most likely $\tau^+\tau^-$ production. SVX hits are represented as lines whose length is proportional to the collected charge. Hits in the VD and several drift chamber layers are also shown. One can easily recognize tracks in the SVX and see the level of spurious noise hits.

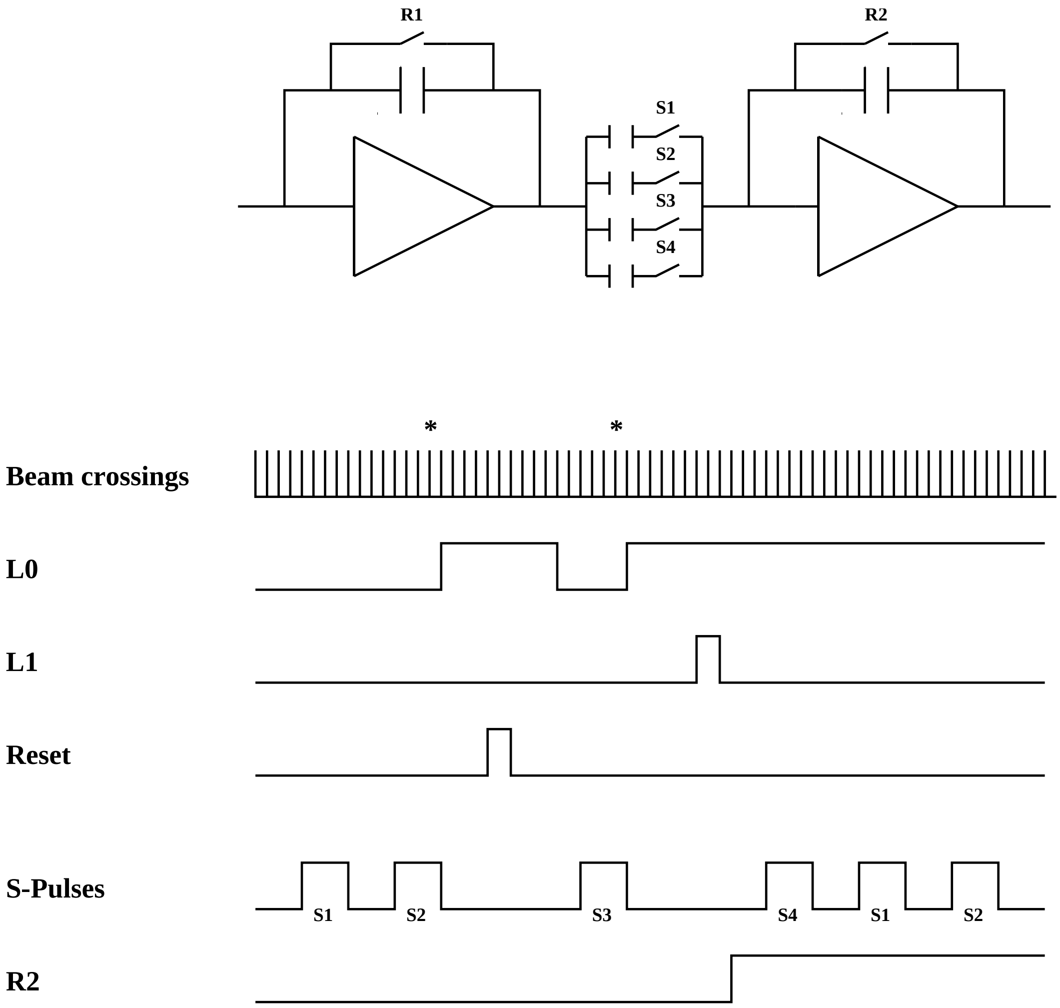

Figure 2.13: Timing diagram of the SVX readout.

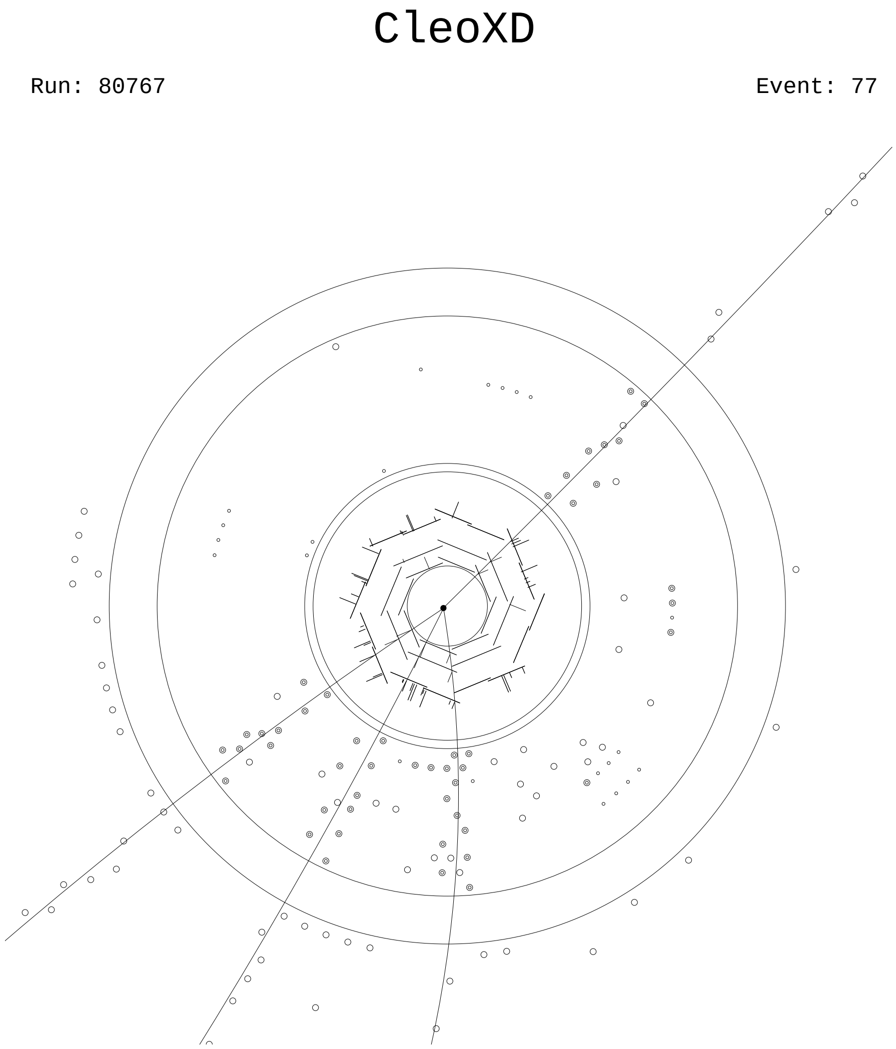

Figure 2.14: SVX event.

2.4 Present and future of experimental B facilities

Let us briefly discuss the current and future experimental prospects for B meson production and studies. Hadronic colliders as well as fixed-target experiments historically were better suited for the discovery of new particles and resonances, due to the wide range of invariant masses accessible there. Once discovered, however, new resonances and particles are easier to study at the e^+e^- collider, where large clean samples can be obtained. This explains why the majority of results in B physics so far came from e^+e^- colliders. The major challenge for an e^+e^- machine operating at the $\Upsilon(4S)$ is luminosity. CESR holds the world record for peak luminosity at $4.1 \times 10^{32} cm^{-2} s^{-1}$. At the moment 3.3 M $B\bar{B}$ events from CLEO II are available. Combined with CLEO II.V data, by the end of 1998 this number should go up to at least 7 M. Further increase in the luminosity will come from the upgrades to CESR and CLEO [58]. It will be possible to achieve a peak luminosity of 2×10^{33}, producing as many as 20 M $B\bar{B}$ pairs per year. CLEO III will become better detector too, with a new Silicon Vertex Detector, Drift Chamber, and RICH-based particle identification system installed. CLEO will have competition at this moment: asymmetric B-factories under construction at SLAC [59] and KEK [60] should begin operation by the end of this century with projected luminosities of $(3-10) \times 10^{33}$.

In the past few years substantial progress was achieved in doing B physics at hadronic machines, in particular at CDF and D0 experiments operating at Fermilab. The main problem lies in the small $\sigma_{b\bar{b}}/\sigma_{tot}$ ratio and difficulties in triggering on $b\bar{b}$ events. B decay channels with leptons in the final states are more accessible, as CDF demonstrated recently by reconstructing a large sample of $B^0 \rightarrow J/\Psi K^0_S$ decays. Reconstruction of the $B^0 \rightarrow \pi^+\pi^-$ decay mode in particular and purely hadronic decays in general is much more challenging and will require a sophisticated triggering scheme. Both CDF [61] and D0 [62] are currently undergoing upgrades for Run II, scheduled to start in 1999.

Meanwhile, the HERA-B experiment at DESY [63] plans to use the halo of the HERA proton beam and internal copper wire targets to stage a fixed-target experiment to study CP violation in the $B^0 \rightarrow J/\Psi K^0_S$ decay. Experimental conditions are much more severe at HERA-B than at CDF/D0, $\sigma_{b\bar{b}}/\sigma_{tot}$ is on the order of 10^{-6} as opposed to 2×10^{-3}. Still, if HERA-B performs as expected, it might be the first experiment to measure $\sin 2\beta$, with the expected turn-on time in the end of 1998. Some of the parameters and predicted performance for all of the described experiments are listed in the Table 2.1.

The experiments listed above represent the near term future of B physics. Looking further ahead, Large Hadron Collider (LHC) at CERN, scheduled to begin operation in the year 2005, will produce an enormous number of B hadrons, as many as 10^{11} in 10^7 seconds (one effective year). While designed for the Higgs and supersymmetry search, two general purpose experiments ATLAS [65] and CMS [66] will be quite competitive in CP violation studies. LHC-B, a dedicated experiment for the study of CP violation in the B system [67] is currently under consideration, as well as BTeV at Fermilab [64]. Table 2.2 lists projected CP physics performance for these experiments.

Table 2.1: List of parameters and expected performance in selected modes for the near-future experiments. One year of running at design luminosity is assumed.

Experiment	BaBar	BELLE	CDF(D0)	HERA-B
$\sigma_{b\bar{b}}$	$\sim 1nb$	$\sim 1nb$	$\sim 100\mu b$	$\sim 760nb$
$\sigma_{b\bar{b}/\sigma_{had}}$	~ 0.2	~ 0.2	~ 0.002	$\sim 10^{-6}$
$\sin 2\alpha$				
$B^0 \to \pi^+\pi^-$	0.2	0.15	0.1	0.14
$B^0 \to \rho^\pm\pi^\mp$	0.11	0.15	-	-
$\sin 2\beta$				
$B^0 \to J/\Psi K_S$	0.1	0.08	0.08	0.13
$B^0 \to J/\Psi K_L$	0.16	0.14	-	-
γ				
$B \to DK^*(K)$	-	12°	-	-

Table 2.2: Parameters and expected performance (one year at design luminosity) for the next generation of B physics experiments.

Experiment	ATLAS	CMS	LHC-B	BTEV
$\sigma_{b\bar{b}}$	$\sim 500\mu b$	$\sim 500\mu b$	$\sim 500\mu b$	$\sim 100\mu b$
$\mathcal{L}$ for B physics	10^{33}	10^{33}	1.5×10^{32}	5×10^{31}
$\sin 2\alpha$ $B^0 \to \pi^+\pi^-$	0.05	0.08	0.05	0.05
$\sin 2\beta$ $B^0 \to J/\Psi K_S$	0.02	0.05	0.02	0.04
γ $B \to DK^*(K)$	-	-	$6 - 12°$	

To summarize, there exists an active experimental program for years to come to ensure precision studies of CP violation in B mesons. The program of upgrades for both CESR and CLEO will enable CLEO to stay at the forefront of B physics well into the 21st century.

CHAPTER 3

EVENT SELECTION AND BACKGROUND SUPPRESSION

3.1 Introduction

Since the expected branching fractions for the processes of interest are on the order of $\mathcal{O}(10^{-5})$ or less, we are faced with a formidable task of finding several (less than 50) events in the 3.3×10^6 $B\bar{B}$ data sample. To make things even worse, $q\bar{q}, \;\; q = \{u, d, s, c\}$ continuum production has cross section approximately 3 times higher than $e^+e^- \to B\bar{B}$ at the $\Upsilon(4S)$. These continuum events pose a serious background problem, faking signal events of interest.

This chapter describes the event selection criteria and background suppression techniques used in the search for $B \to K\pi, \; \pi\pi$ decays.

3.2 Event selection

CLEO data taken at the $\Upsilon(4S)$ resonance is divided into several data sets[68], labeled as 4s1, 4s2,...4s9, 4sA, 4sB,... etc. For this analysis we used data sets 4s1 through 4sG, which correspond to the complete CLEO II data.

Only events classified as hadronic decays are used in this analysis. In order to qualify as hadronic, an event must contain at least 3 charged tracks, the energy of all tracks should be larger than 0.15 of the center of mass energy E_{CM} and the total energy of showers in the calorimeter should be larger than $0.15E_{CM}$ as well. The event vertex has to be within ± 2 cm in x and y and ± 5 cm in z of the nominal interaction point position. In addition to the hadronic event class requirements above, we demand the total number of tracks in the event to be at least $N_{cand} + 3$. N_{cand} is the number of tracks used to form the B meson candidate.

We divide all data into two subsets: ON- and OFF-resonance. The former refers to the data taken with CESR running at the beam energies of $5.285 \leq E_{beam} \leq 5.295$, on top of the $\Upsilon(4S)$ resonance. The latter is defined by the energy range of $5.187 \leq E_{beam} \leq 5.28$ and is free of B mesons. We use the OFF-resonance data only to study continuum background.

B meson candidates are formed from tracks, π^0's and K^0_S's satisfying selection criteria described below.

3.2.1 Tracks

We impose track quality cuts based on the impact parameters in $r - \phi$ and $r - z$ planes and the average hit residual. We require a track to have hits in at least 50% of the tracking layers it traversed. The track quality package TRKMAN [69] is used to remove "curlers", "ghosts" and other tracking misfits. For the analysis of the $B^0 \to K^+\pi^-/\pi^+\pi^-$ decay mode we impose additional cuts on the missed distance in the $r - \phi$ and $r - z$ planes.

Electrons are vetoed by using the ratio of the measured track momentum to the matched shower energy in the CsI calorimeter [70] . Tracks penetrating more than five nuclear interaction lengths in the iron are rejected as muons [71].

3.2.2 π^0's

We reconstruct π^0's as two showers with an unconstrained invariant mass $115 \leq M_{\gamma\gamma} \leq 155$ MeV. At least one photon has to be in the "good barrel" region of $|\cos\theta| < 0.71$. Minimal shower energy is 30 MeV in the "good barrel" and 50 MeV elsewhere. The shower shape should be consistent with photon's and we impose an additional cut on the decay angle of the π^0: $|\cos\theta_{dec}| < 0.97$, where θ_{dec} is the angle between the π^0 flight direction and the photon in the π^0's rest frame. All π^0 candidates are kinematically fitted assuming the nominal π^0 mass. The spectrum of $M_{\gamma\gamma}$ after all selection cuts is given in Figure 3.1. Mass resolution for high momentum π^0's is approximately 10 MeV.

3.2.3 K_S^0's

Pairs of tracks forming a displaced vertex are taken as K_S^0 candidates. We require the secondary vertex to be displaced by at least 3 mm from the primary vertex of the event and the $\pi^+\pi^-$ invariant mass to be within 10 MeV from the nominal K_S^0 mass. Figure 3.2 shows the $\pi^+\pi^-$ invariant mass distribution for K_S^0 candidates in the data. A flight distance cut has already been applied.

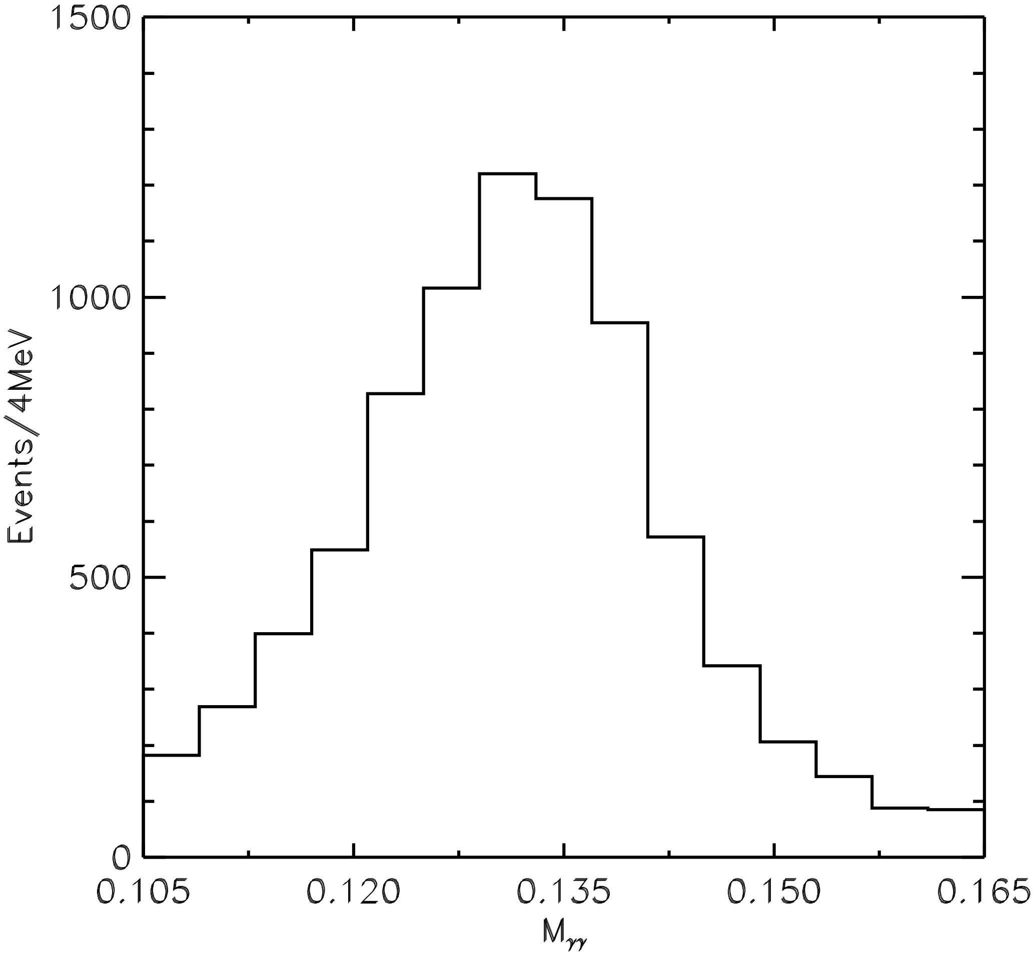

Figure 3.1: $M_{\gamma\gamma}$ for the π^0 candidates in the data.

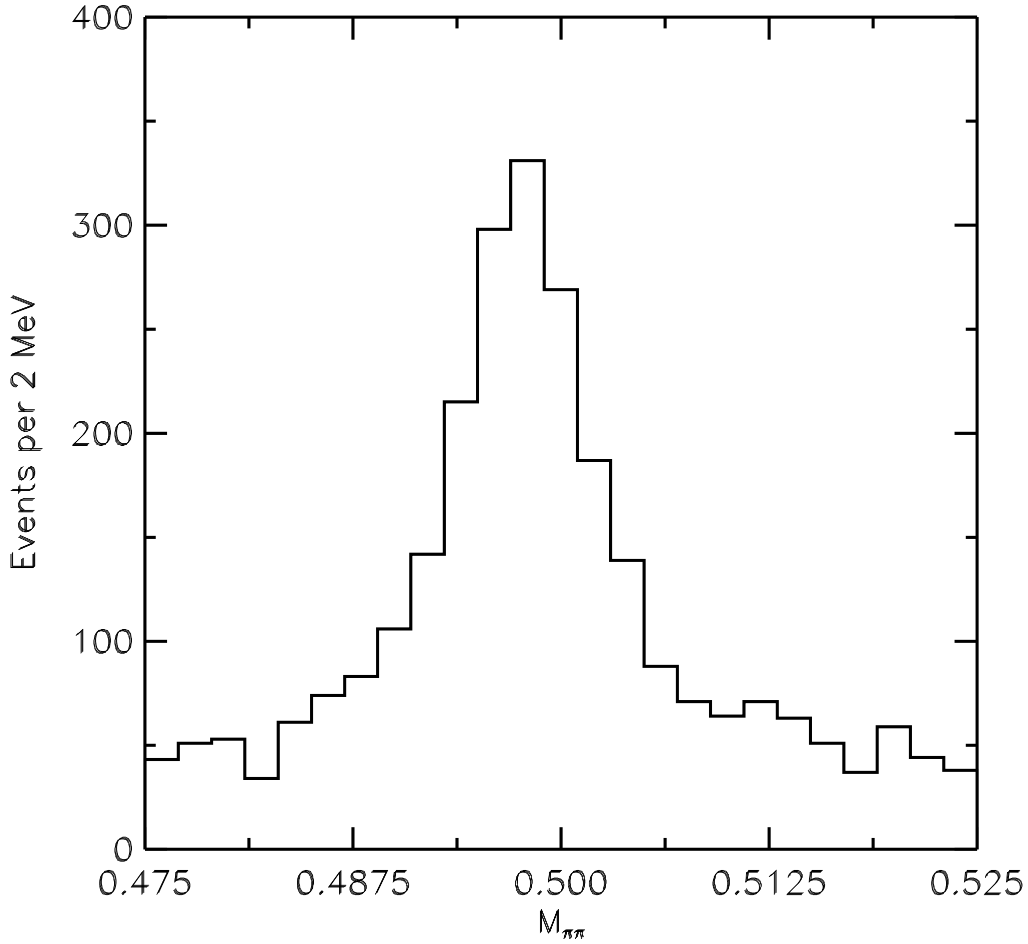

Figure 3.2: K_S^0 mass distribution in the data.

3.2.4 Particle identification

In the momentum range of interest to us, 2.3 - 2.9 GeV/c, only dE/dx discriminates between different hadron species. Figure 3.3 shows σ_K distribution for kaons and pions in the momentum range of 2.3 to 2.9 GeV/c. In principle, continuum background contains not only pions and kaons, but also protons. It is reasonable to ask, whether we should consider proton hypothesis as well. Fortunately, for this particular momentum range the dE/dx for protons and kaons is practically identical and we can treat protons and kaons on the same ground. We therefore consider only kaon and pion dE/dx hypotheses in this analysis.

We require that tracks (excluding K^0_S daughters) have good dE/dx information. In addition to that, for $h^+\pi^0$ and $h^+K^0_S$ modes we require the dE/dx for the track to be consistent with either kaon or pion hypothesis at the 3σ level:

$$Min(\sigma_K, \sigma_\pi) < 3\ . \tag{3.1}$$

For the h^+h^- analysis a similarly loose requirement of

$$Min(\sigma^2_{K1}, \sigma^2_{\pi 1}) + Min(\sigma^2_{K2}, \sigma^2_{\pi 2}) < 6 \tag{3.2}$$

is imposed to remove tracks with outrageous dE/dx.

3.3 Candidate selection

With the basic building blocks such as track, π^0 and K^0_S at hand, we now can proceed in search for the B meson decays.

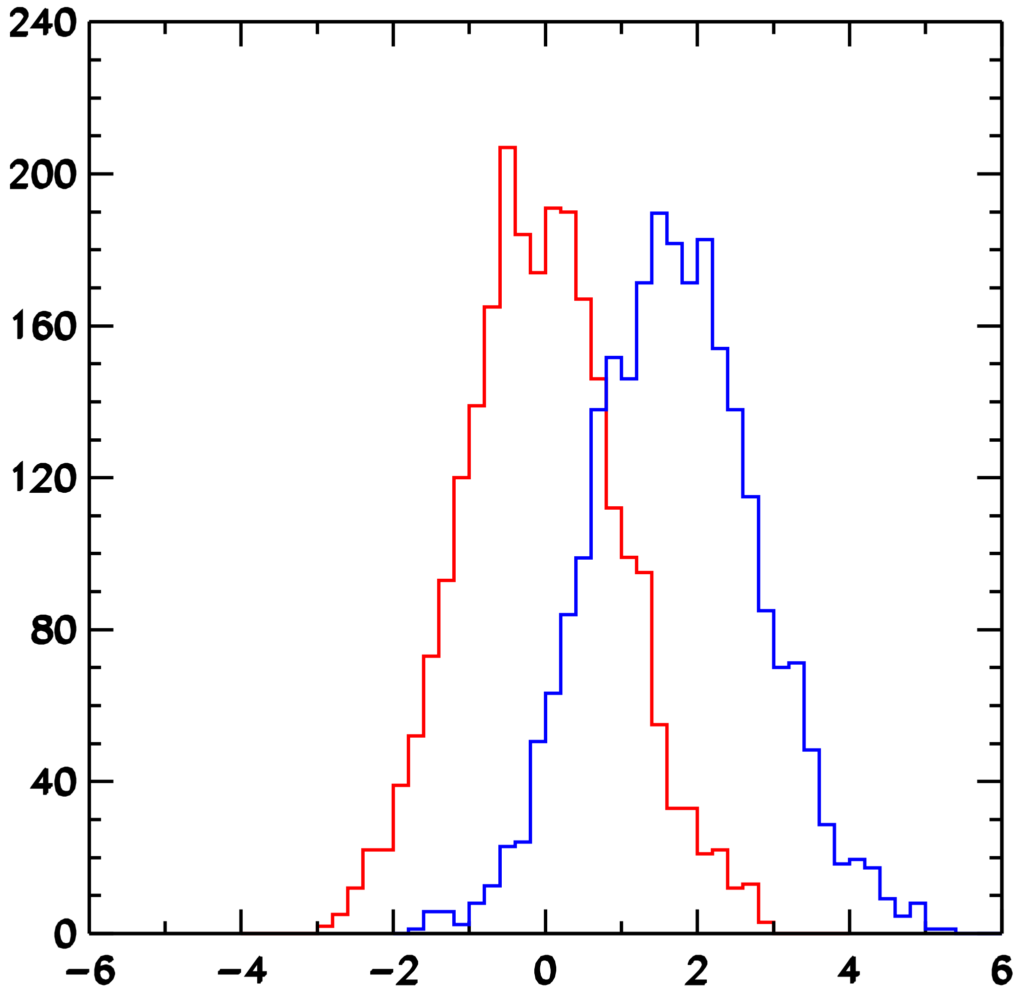

Figure 3.3: $K - \pi$ dE/dx separation for high momentum (2.3 - 2.9 GeV/c) kaons and pions.

3.3.1 Energy conservation

At the symmetric e^+e^- collider the $\Upsilon(4S)$ is produced at rest. This means that each of the B mesons produced will have its energy E_B equal to the energy of the beam E_{beam}. We can define ΔE as $\Delta E = E_1 + E_2 - E_{beam}$ and note that for the true B meson it should be centered around 0 with the width determined by the detector resolution. When calculating the energy of the charged particles we always assume the pion mass hypothesis. This has an effect of the overall shift of the ΔE signal distribution by -42 MeV for each charged kaon present in the final state. We can use this effect to our advantage to gain additional separation between $K^+\pi^-$ and $\pi^+\pi^-$.

Table 3.1 lists ΔE resolution for different modes as determined from Monte Carlo [77]. Previous studies [51, 78] showed that the Monte Carlo models ΔE resolution quite well. Modes with π^0's in the final state have significantly worse ΔE resolution. The ΔE distribution in this case becomes asymmetric as shown in Figure 3.4. This effect is due to the substantial leakage of the shower energy through the ends of the crystals. We find that the sum of two bifurcated Gaussians describes the ΔE shape for modes with π^0 quite well. The single Gaussian parameterization is used for all-charged final states.

Background events are distributed almost uniformly in ΔE, with slight negative slope as shown in Figure 3.5.

Table 3.1: ΔE resolution (MeV) for different modes as determined from Monte Carlo. Modes with π^0's in the final state are parameterized by the sum of two bifurcated Gaussians with relative normalization given in the last column.

Decay mode	Ave.	σ_L	σ_R	Norm.
$\pi^+\pi^-$	0	27	27	
$K^+\pi^-$	-42	27	27	
K^+K^-	-84	27	27	
$\pi^+K^0_S$	0	26	26	
$K^+K^0_S$	-42	26	26	
$\pi^+\pi^0$	0	49	42	0.86
	0	132	31	0.14
$K^+\pi^0$	-42	49	42	0.86
	-42	132	31	0.14
$K^0_S\pi^0$	0	47	32	0.66
	0	100	66	0.34
$\pi^0\pi^0$	-21	53	53	0.62
	-21	162	82	0.38

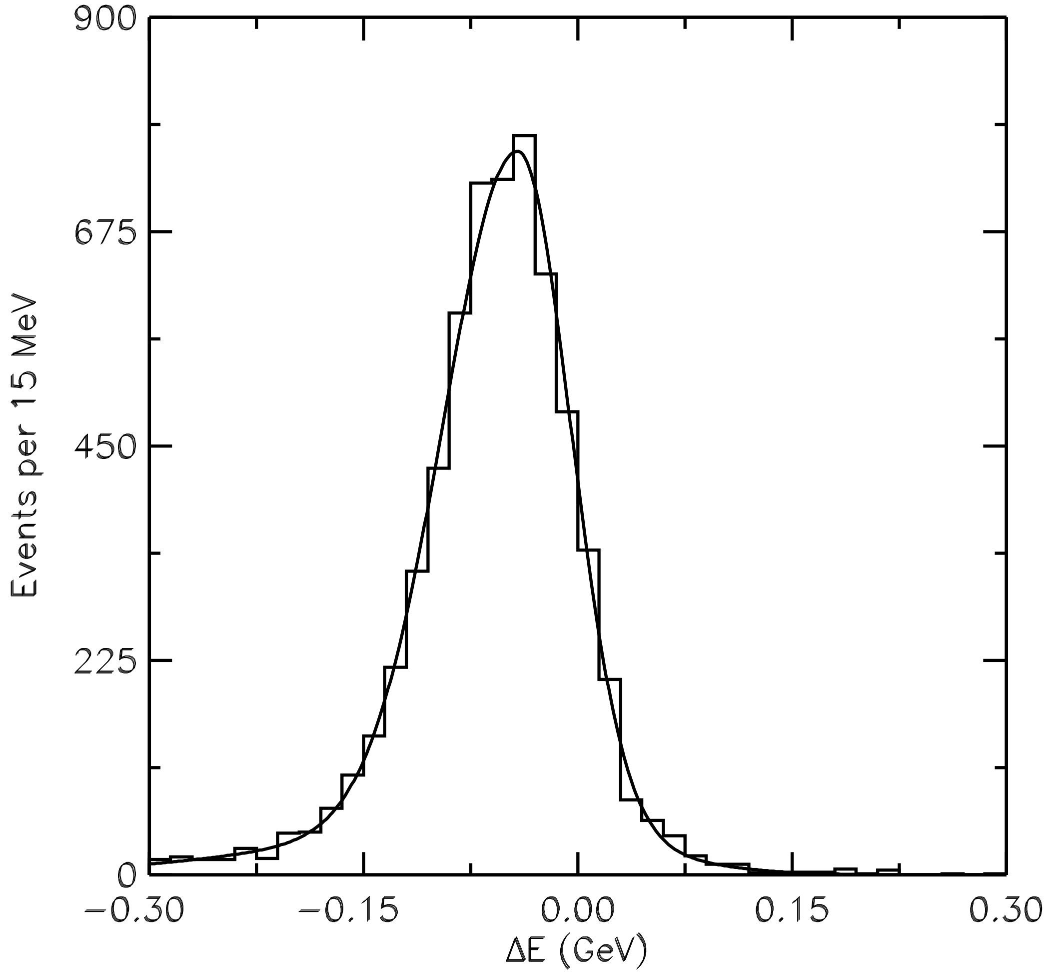

Figure 3.4: ΔE distribution for the $K^+\pi^0$ signal in Monte Carlo.

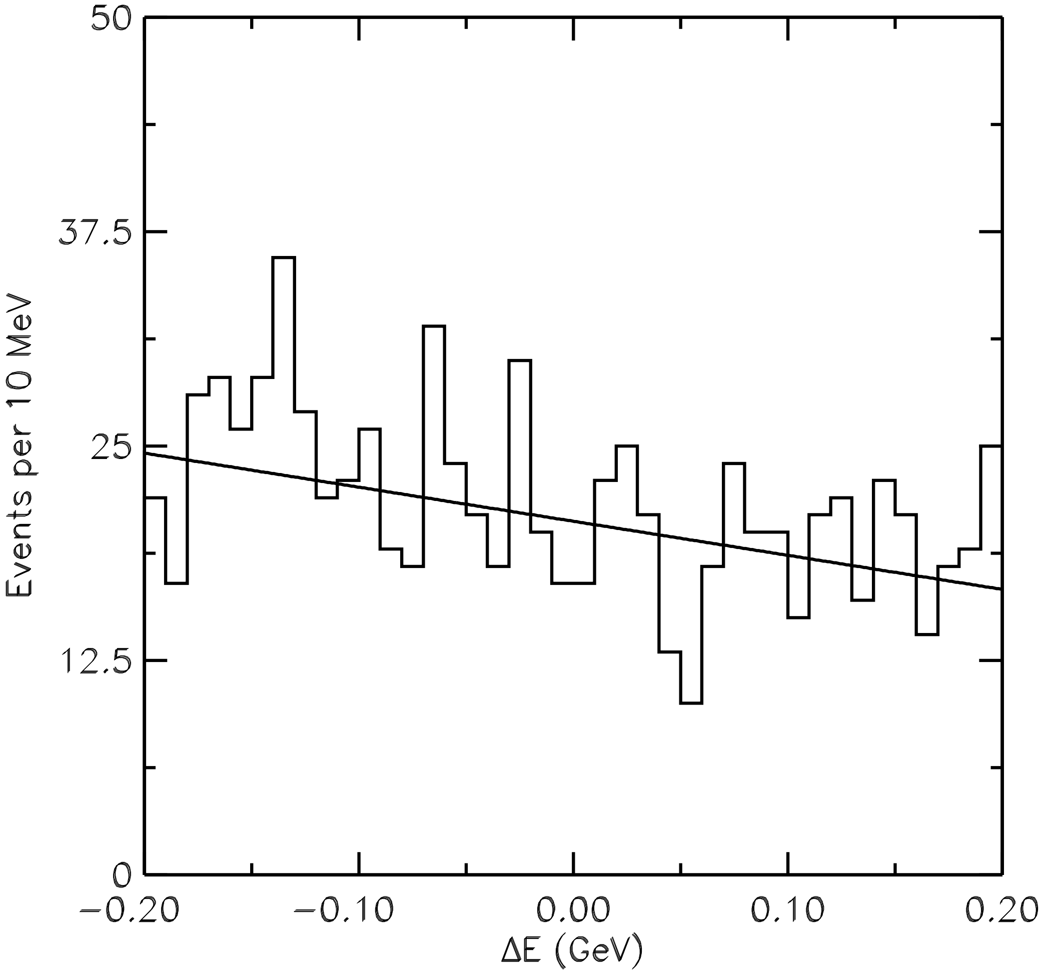

Figure 3.5: ΔE distribution for the background in the h^+h^- mode in the OFF-resonance data.

3.3.2 Beam-constrained mass

When calculating the invariant mass of the B meson candidate $M_B = \sqrt{E_B^2 - p_B^2}$ we again can exploit the fact that at CLEO the B meson energy is equal to the beam energy and use E_{beam} instead of the measured $E_B = E_1 + E_2$ to calculate M_B. This constraint improves mass resolution by almost an order of magnitude, since E_{beam} is known to much better precision than E_B and p_B is small, on the order of 300 MeV/c. The beam-constrained mass resolution can be deduced from Monte Carlo and verified by the sample of fully reconstructed low-multiplicity B decays [79], shown in Figure 3.6. It is typically in the range of 2.5 - 3.0 MeV, depending on the decay mode. Table 3.2 lists the M_B resolution for our modes. We use the bifurcated Gaussian shape to parameterize the M_B distribution for the signal. Again, in the case of decay modes with π^0 we add a second bifurcated Gaussian to take into account tails of the distribution properly.

The M_B distribution for the continuum background is shown in Figure 3.7 where we plotted OFF-resonance data for the h^+h^- mode. We always shift the calculated M_B by $5.2892 - E_{beam}$ for the OFF data to provide kinematical match with the ON data. The M_B background shape is modeled well by the empirical shape

$$f(M_B) \sim M_B\sqrt{(1-x^2)}e^{-\lambda(1-x^2)} \qquad (3.3)$$

with $x = M_B/E_{beam}$. Figure 3.7 also has the results of the fit superimposed.

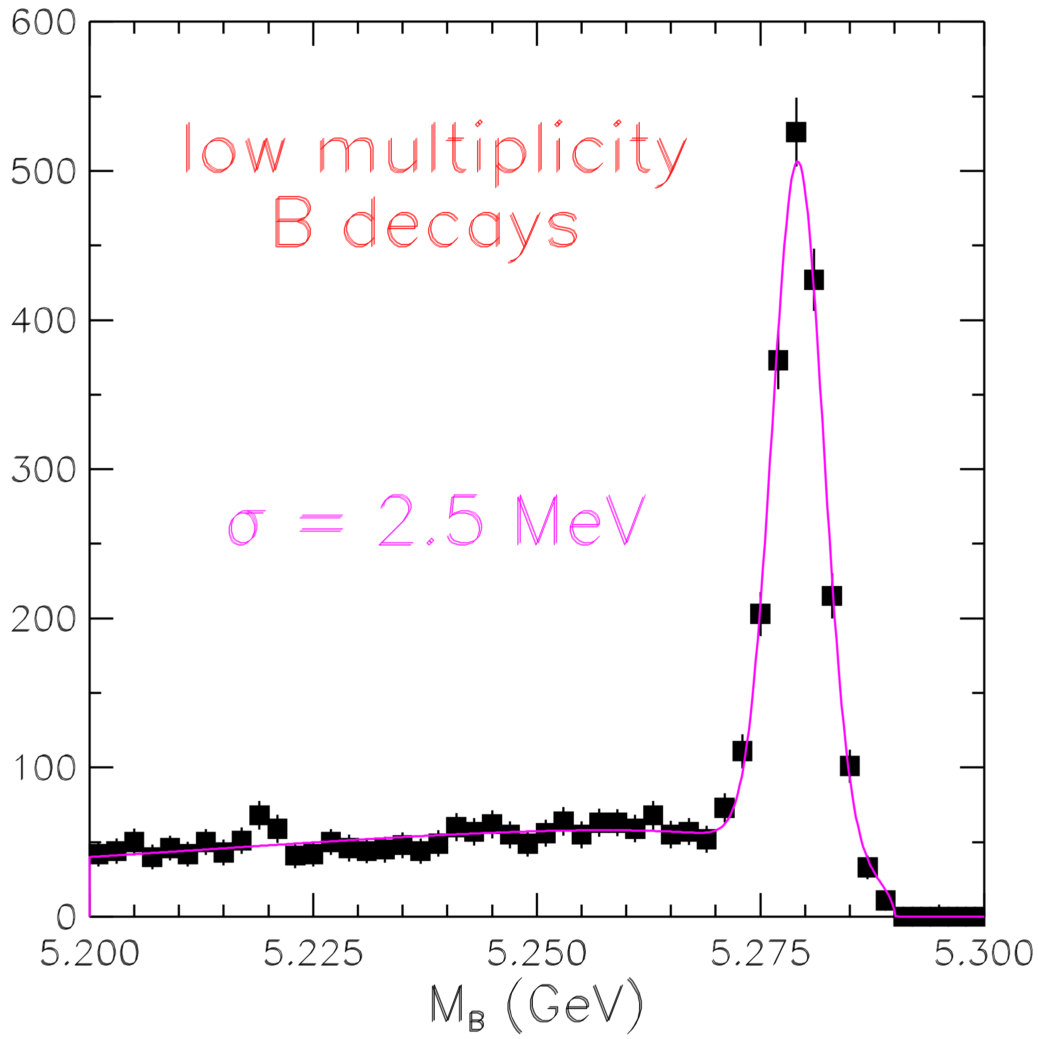

Figure 3.6: Beam-constrained mass distribution for the sample of the reconstructed B mesons in the data.

Table 3.2: Beam-constrained mass resolution (MeV) for different modes as determined from Monte Carlo. For modes with π^0's in the final state the last column gives the relative normalization of two bifurcated Gaussians used to parameterize the M_B distribution.

Decay mode	σ_L	σ_R	Norm.
h^+h^-	2.7	2.4	
$h^+K_S^0$	2.9	2.4	
$h^+\pi^0$	2.7	2.8	0.77
	5.2	2.8	0.23
$K_S^0\pi^0$	2.8	2.8	0.85
	5.8	2.8	0.15
$\pi^0\pi^0$	2.9	3.2	0.74
	6.6	3.2	0.26

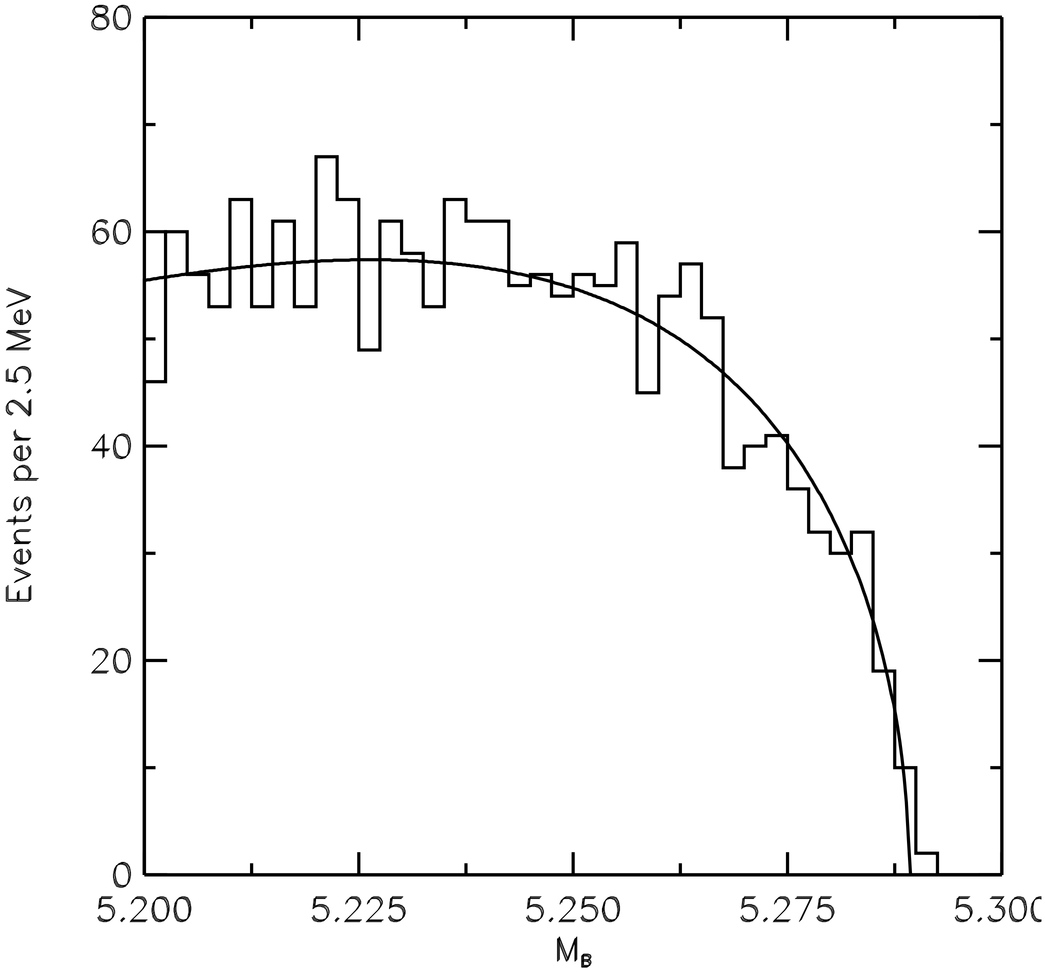

Figure 3.7: M_B distribution for the continuum background. OFF-resonance data for the h^+h^- analysis.

3.4 Background suppression

The main source of background in this analysis comes from the continuum production of $e^+e^- \to q\bar{q},\ q = \{u, d, s, c\}$. The $B\bar{B}$ background is negligible, since high momentum decay products from the charmless B decays are not found in the dominant $b \to c$ B decays. The kinematic variables M_B and ΔE described above provide some discrimination against continuum background, but it remains relatively easy to pick two random high momentum particles which will make a "B meson" in the $M_B - \Delta E$ plane. In this section we describe methods which use information about the shape of the event to suppress continuum background.

3.4.1 $cos\Theta_{sph}$

Continuum events are "jetty" in their nature - this is the consequence of the underlying production of the highly boosted light quarks and their subsequent hadronization. A typical continuum event is shown in Figure 3.8, where two jets of particles are quite evident. B mesons on the other hand are produced almost at rest. As a result, decay products of the B meson are distributed practically isotropically and event has a spherical shape, shown in Figure 3.9.

We use this distinction in the following way. For a given set of N tracks and showers we can define the momentum tensor

$$S_{ij} = \sum_{1}^{N} (\delta_{ij} P^2 - P_i P_j) \tag{3.4}$$

and calculate its eigenvectors which we label as the major, semi-major, and semi-minor sphericity axes. We then calculate the major sphericity axis of the candidate

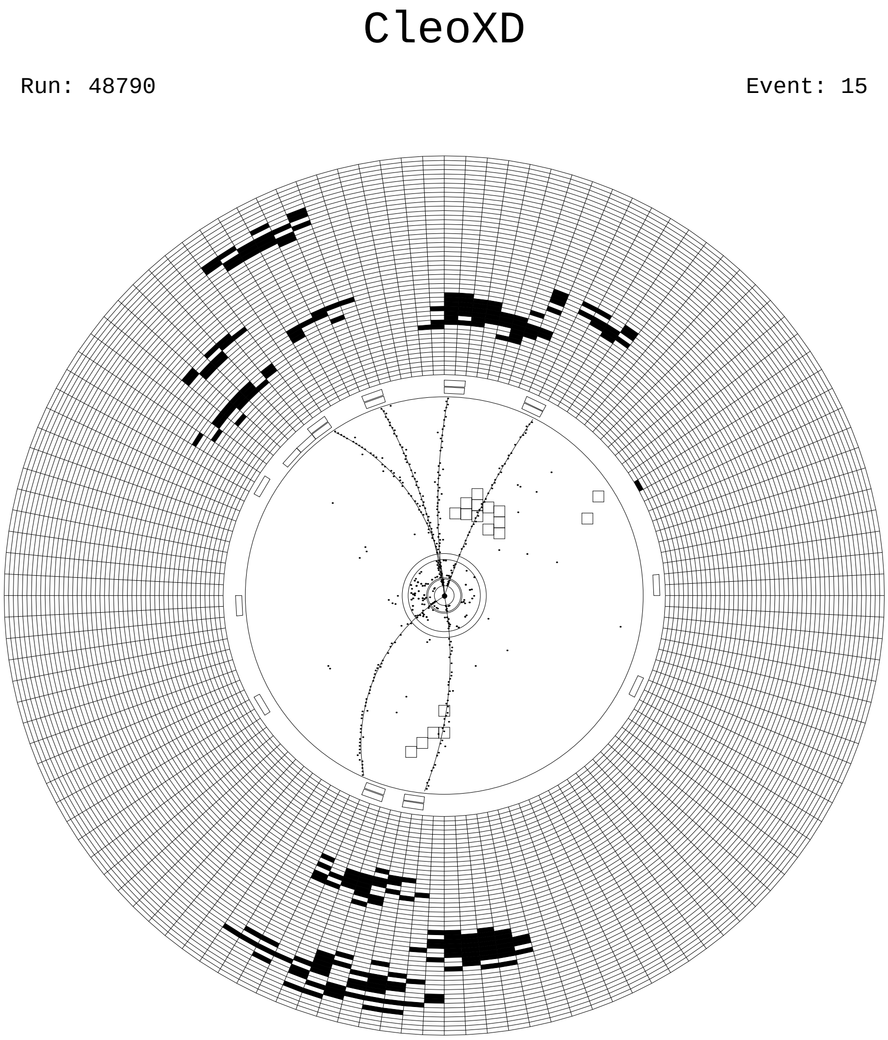

Figure 3.8: Typical jetty continuum event.

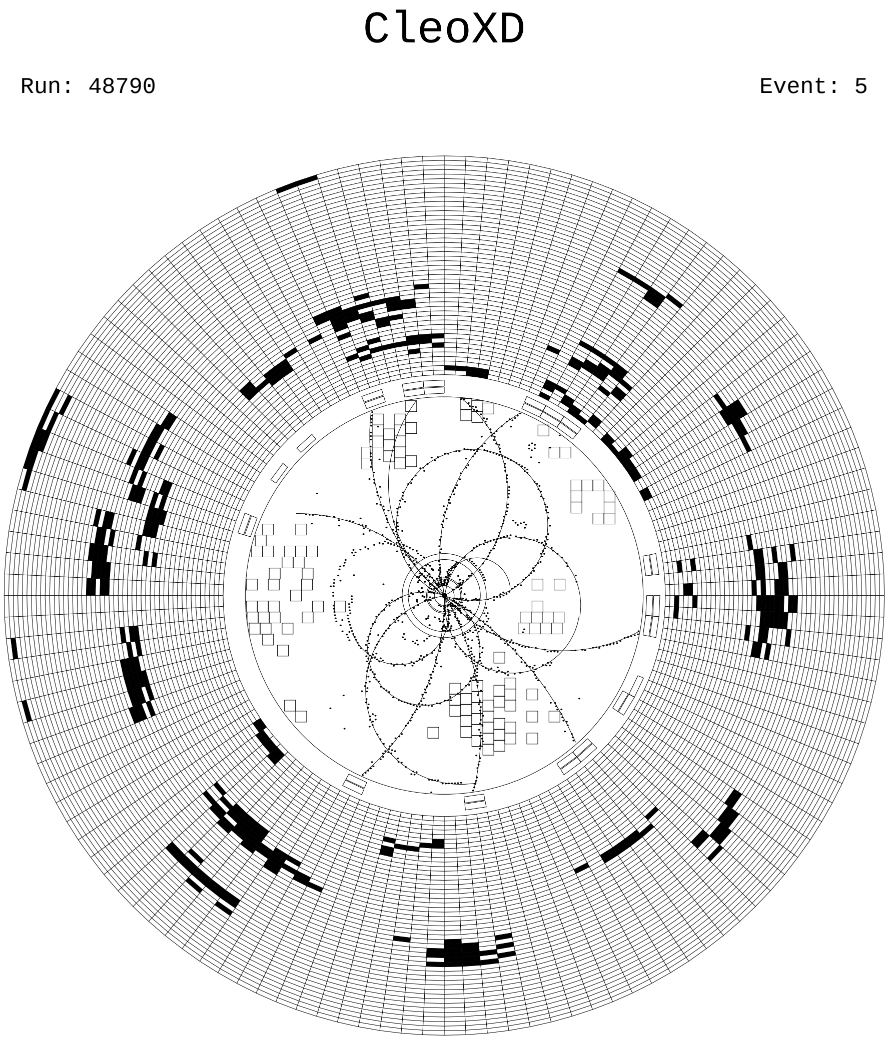

Figure 3.9: Typical spherical $B\bar{B}$ event.

and the major sphericity axis for the rest of the event, that is, for all remaining good tracks and showers. When calculating the sphericity axis for the rest of the event we require tracks and showers to meet minimal quality criteria. Tracks should satisfy essentially the same (although less stringent) requirements as the candidate tracks. We consider showers with $E > 50$ MeV only and veto all bad showers and showers matched to tracks. We also remove all showers with $E < 100$ MeV and $cos\Theta_\gamma > 0.9$, where Θ_γ is the angle between the shower axis and any candidate track. This last requirement was designed to remove split-off showers from the hadronic interactions in the calorimeter. We find that this filtering helps to achieve better separation between signal and background in the $\cos\Theta_{sph}$ variable.

The cosine of the angle between the two axes, $\cos\Theta_{sph}$, has an almost flat distribution for the spherical $B\bar{B}$ events and peaks at ±1 for the jetty continuum events, as illustrated in Figure 3.10. It can be seen from the Figure 3.10 that the $cos\Theta_{sph}$ variable provides very powerful background rejection. For instance, a cut at $|cos\Theta_{sph}| < 0.7$ has 68 % efficiency for the signal and only 7% efficiency for the background. Note that the $cos\Theta_{sph}$ distribution for the signal is not perfectly flat, giving 68% instead of expected 70% efficiency of the cut. This non-flatness is mostly due to the imperfect track-shower matching and split-off showers.

In principle one can use the thrust axis instead of the sphericity axis and work with $cos\Theta_{thr}$. Our decision to use $cos\Theta_{sph}$ variable was motivated by the fact that it is slightly more efficient for the signal events while providing the same background rejection.

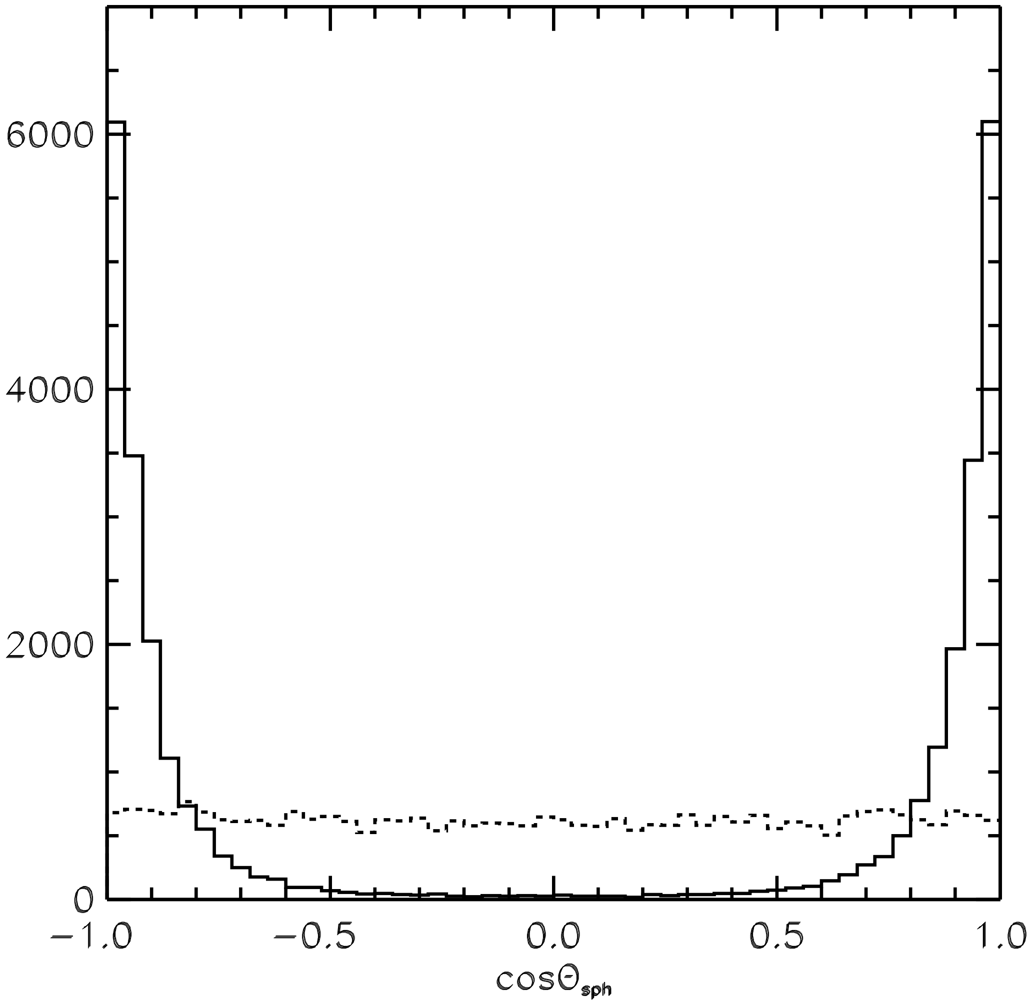

Figure 3.10: $cos\Theta_{sph}$ distribution for the continuum (solid line) data and the signal Monte Carlo (dotted line) $h^+\pi^0$ events.

3.4.2 Fisher discriminant

The $cos\Theta_{sph}$ variable is very powerful in suppressing the continuum background. Continuum events which survived the $cos\Theta_{sph}$ cut look almost like the signal and we have to look for more subtle features to distinguish signal and background. It turns out that there are indeed several such variables which we describe below.

Virtual Calorimeter

We have already used some information about the shape of the momentum flow in the event while computing $cos\Theta_{sph}$. It is reasonable to expect that apart from the overall sphericity axis orientation for the rest of the event, the distribution of the particles' momenta around the candidate sphericity axis should be somewhat different for the signal and background events. In order to characterize these differences we construct the so called Virtual Calorimeter (VC) [72], illustrated in Figure 3.11. We divide the solid angle with the respect to the candidate sphericity axis into conical segments, each covering a polar angle interval of 10 degrees. Forward and backward cones are then folded, leaving us with 9 Virtual Calorimeter elements. We calculate the scalar sum of momentum flow of the tracks and showers into each of the cones, measuring the "pulse heights" in the Virtual Calorimeter. "Pulse height" distributions for the signal and background events are shown in Figure 3.12 [73]. It is evident that VC provides some discrimination between signal and background, although the differences are not striking enough to warrant cutting on any of the individual VC variables.

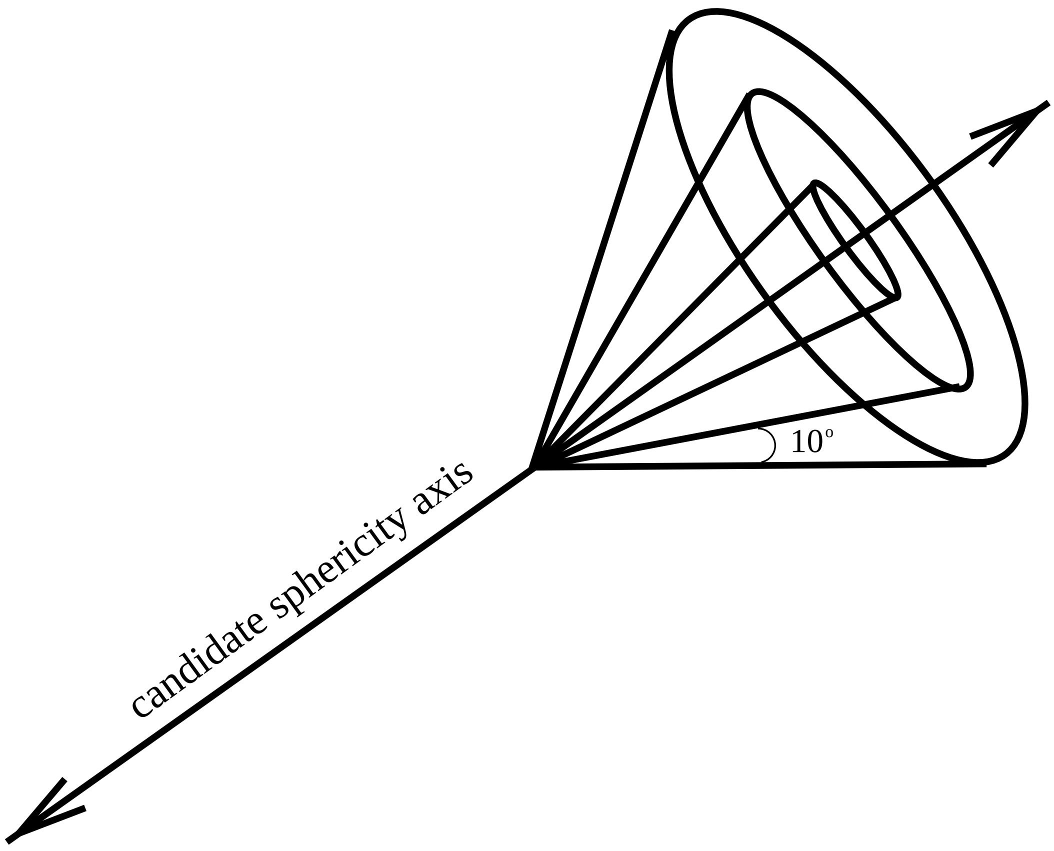

Figure 3.11: Illustration of the Virtual Calorimeter concept.

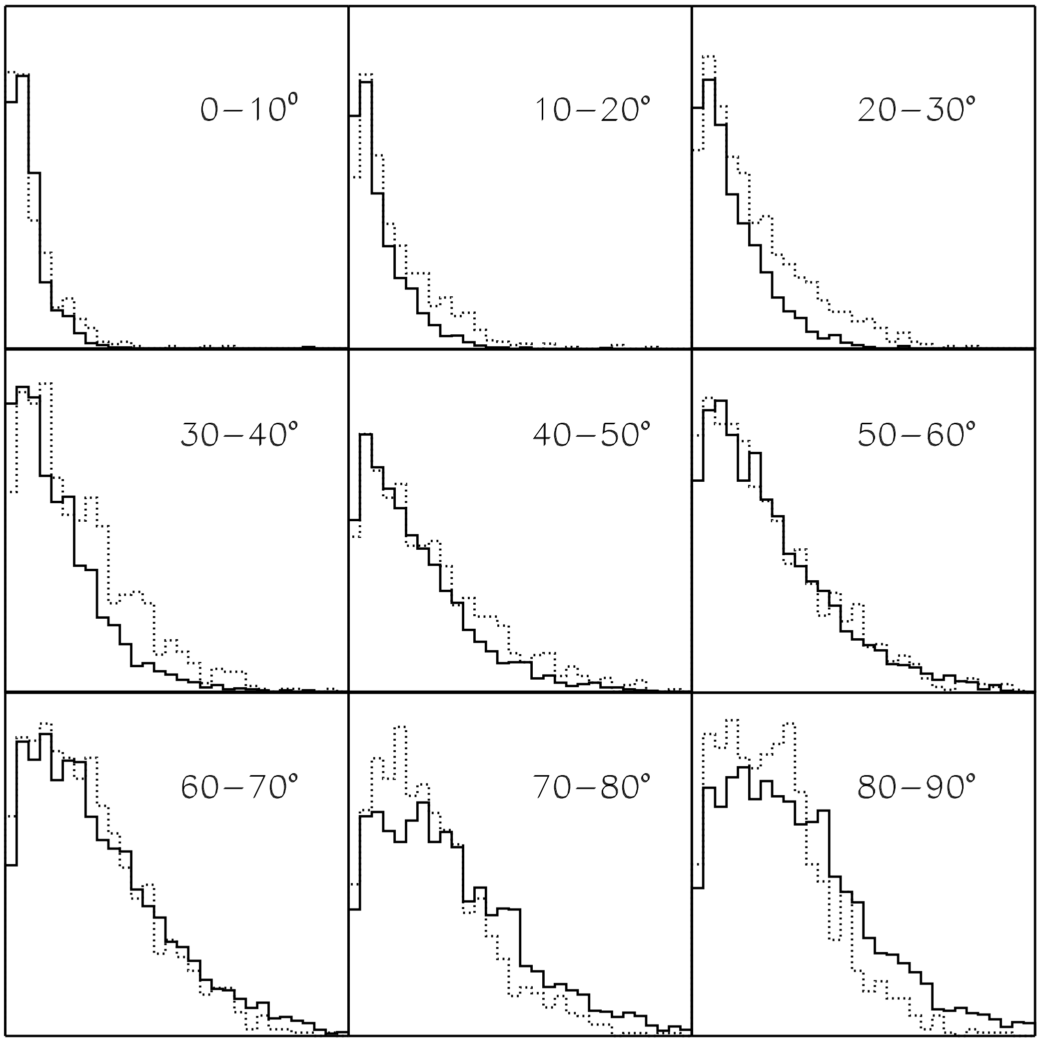

Figure 3.12: Virtual Calorimeter pulse heights for signal (solid histograms) and continuum (dotted histograms) events.

Angular momentum conservation

Let us recall that B mesons are spin 0 particles and at the $\Upsilon(4S)$ resonance they are produced through the single photon e^+e^- annihilation. Since the virtual photon has only ± 1 helicities, the angular distribution of the produced B mesons has a $sin^2\Theta_B$ dependence, where Θ_B is the angle between the B meson flight direction and the beam axis. For the continuum background events, the reconstructed B momentum has an essentially random orientation and we should expect a flat distribution in the $cos\Theta_B$ variable. Figure 3.13 shows the $|cos\Theta_B|$ distribution for signal and background.

We can also use the fact that all our decays are of the $P \to PP$ kind, where P denotes a pseudoscalar meson. This leads to the isotropic decay of the B meson and a flat distribution in $|cos\Theta_{can}|$, where Θ_{can} is the angle between the sphericity axis of the candidate and the z axis. Since continuum background events are due to $e^+e^- \to q\bar{q}$ production, where q is a spin 1/2 quark, the $|cos\Theta_{can}|$ distribution for the background is proportional to $1 + cos\Theta_{can}^2$, as can be seen in Figure 3.14.

Second Fox-Wolfram moment

Another shape variable which we find useful is the second Fox-Wolfram moment R_2 [74]. It measures the overall isotropy of the momentum distribution in the event. All tracks and showers used to calculate $cos\Theta_{sph}$ are included in the R_2 calculation. The R_2 distributions after the $|cos\Theta_{sph}| < 0.8$ cut are shown in Figure 3.15

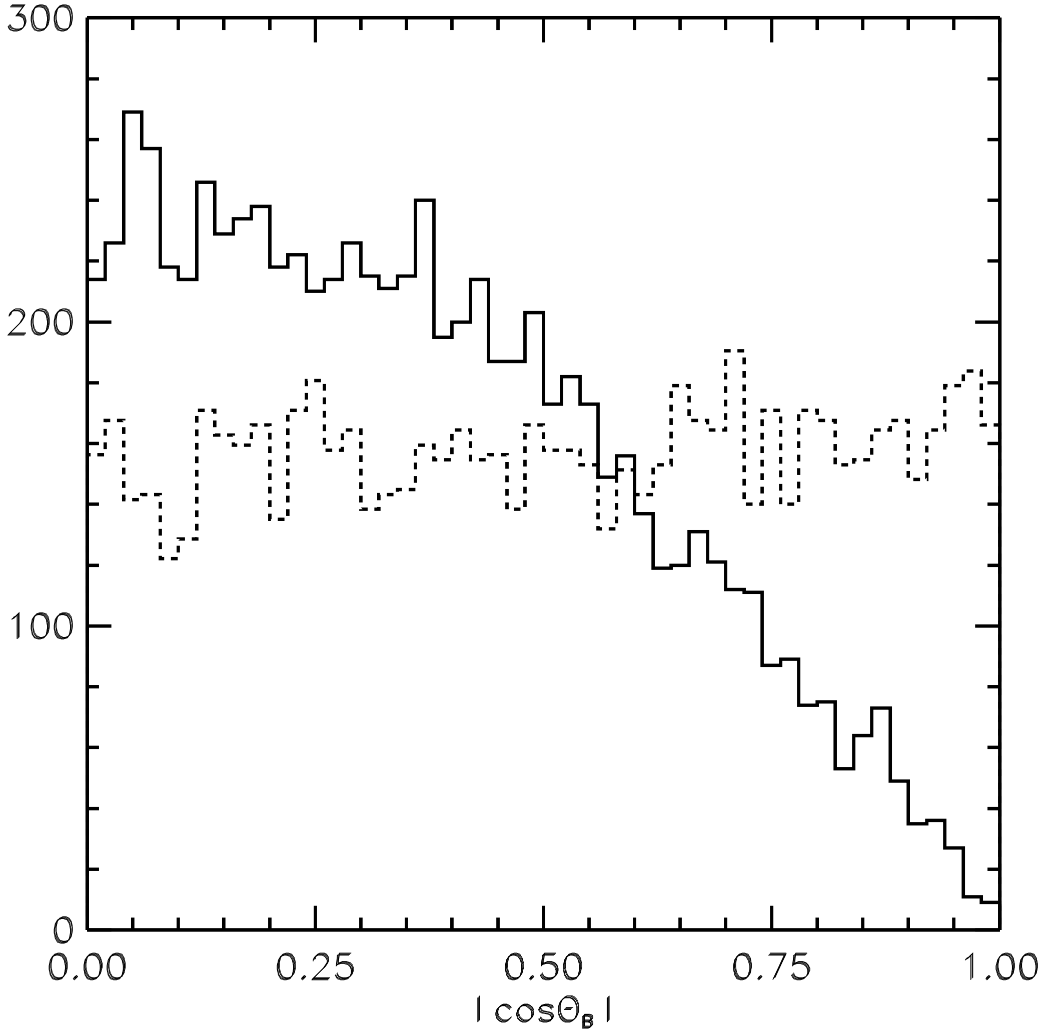

Figure 3.13: The $|cos\Theta_B|$ distribution for signal (solid line) and background (dotted line) events.

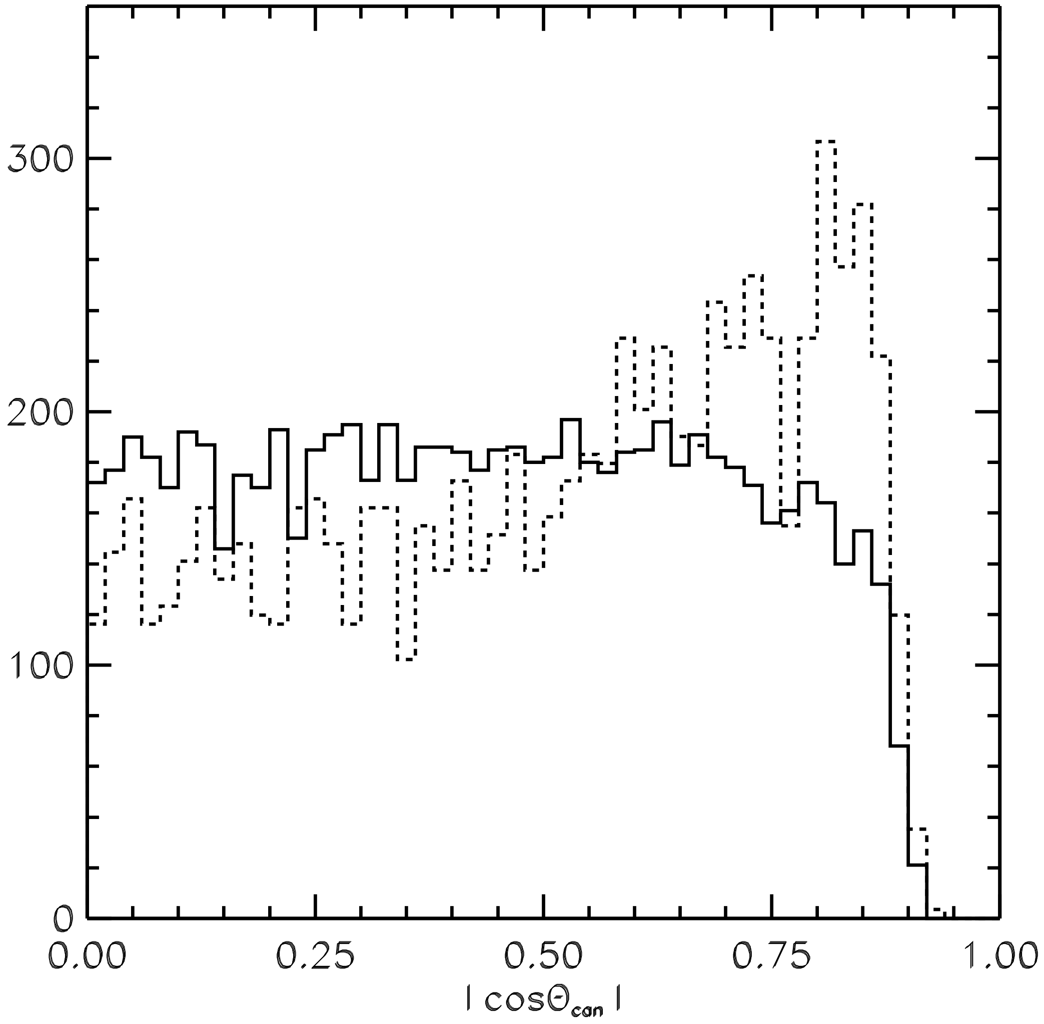

Figure 3.14: $|cos\Theta_{can}|$ distribution for signal (solid line) and background (dotted line) Monte Carlo events.

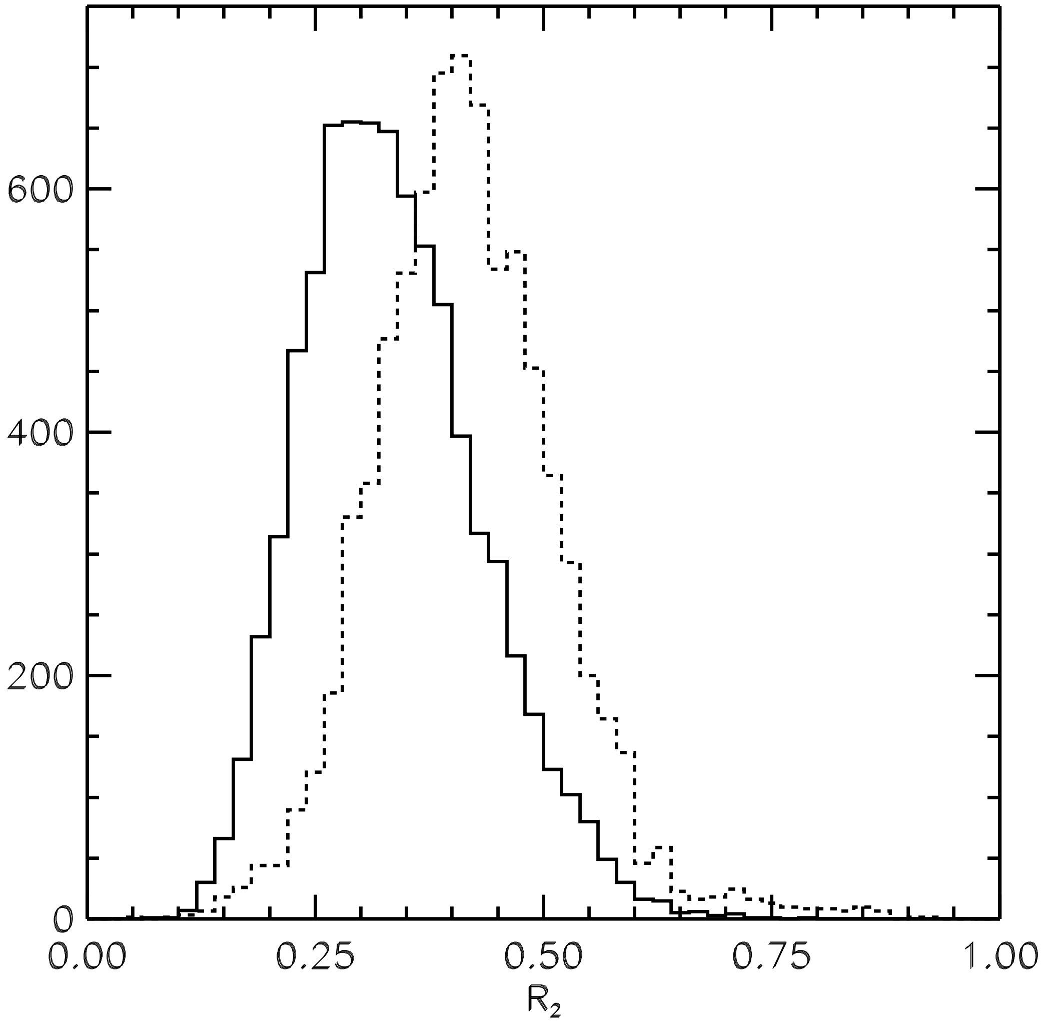

Figure 3.15: R_2 distribution for signal Monte Carlo (solid line) and background data (dotted line) events after the $|cos\Theta_{sph}| < 0.8$ cut.

Definition of the Fisher discriminant

So far we have shown that there are additional variables discriminating between continuum background and signal events, but almost none of the individual variables provides separation good enough on its own. The idea is then to combine all available variables into one which will have the best separation between signal and background. We achieve this goal with the help of the Fisher discriminant [75], originally designed to sort various plant species, but lately in wide use in experimental particle physics [72, 73, 76]. The Fisher discriminant is a linear combination of the N input variables:

$$\mathcal{F} = \sum_{i=1}^{N} \alpha_i x_i \ . \tag{3.5}$$

The coefficients α_i are chosen to provide maximal separation between the output values of $\mathcal{F}$ for signal and background. Given the covariance matrices for the signal and background input variables U^S_{ij} and U^B_{ij} as well as the mean values μ^S_i and μ^B_i, α_i are determined by

$$\alpha_i = \sum_{j=1}^{N} (U^S + U^B)^{-1}_{ij} \times (\mu^S_j - \mu^B_j). \tag{3.6}$$

We calculate α_i for any given set of the input variables using large Monte Carlo samples of signal and background events for the $B^0 \to h^+h^-$ mode. After experimenting with several combinations of the input variables, we arrived at the following set: nine elements of the Virtual Calorimeter VC_i, $|cos\Theta_{can}|$ and R_2. The corresponding coefficients α_i are given in the Table 3.3. The $cos\Theta_B$ in this analysis is not used in the Fisher discriminant. We decided to use it as one of the maximum likelihood fit variables instead. Output values of the Fisher discriminant

Table 3.3: Coefficients for the Fisher discriminant used in this analysis.

No.	Input Variable	α_i
1	VC_1	0.401
2	VC_2	0.859
3	VC_3	0.734
4	VC_4	0.416
5	VC_5	0.074
6	VC_6	-0.192
7	VC_7	-0.525
8	VC_8	-0.796
9	VC_9	-0.879
10	$\|cos\Theta_{can}\|$	0.439
11	R_2	-2.491

for signal and continuum background are plotted in Figure 3.16 (we always rescale Fisher discriminant output $\mathcal{F} = (\mathcal{F} + 5.)/6.$ for convenience) . To make sure our MC models the Fisher discriminant well, we check the agreement between data and MC in two ways. First, we compare the $\mathcal{F}$ distribution for the $B \to D\pi$ signal events in the data and MC in Figure 3.17(a). Second, we do the same for the h^+h^- continuum background in Figure 3.17(b). We find good agreement between MC and data in both cases. In the subsequent analyses we rely on the Monte Carlo sample to provide us with the parameterization of the $\mathcal{F}$ shape for the signal events. We determine $\mathcal{F}$ shape for the background events from the data.

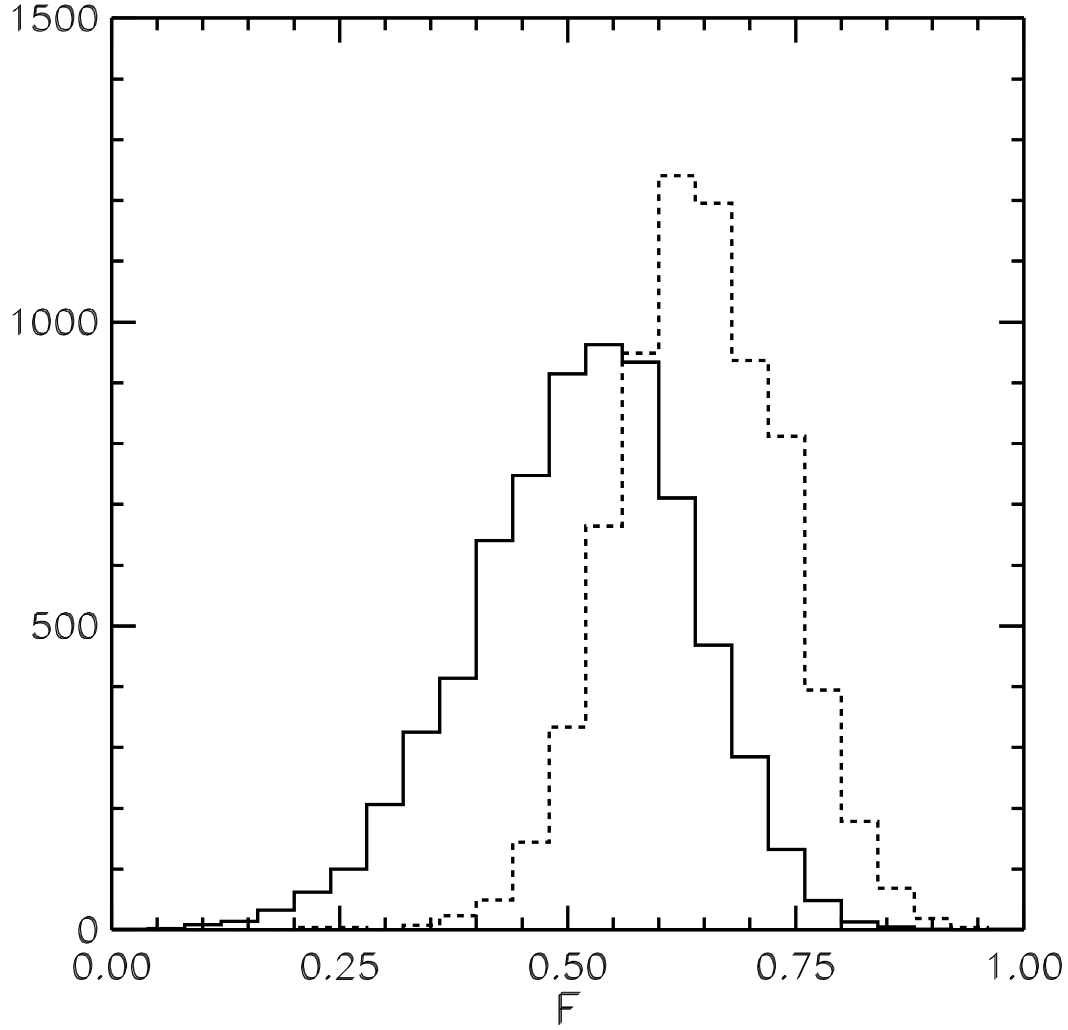

Figure 3.16: $\mathcal{F}$ distribution for signal (solid line) and background (dotted line) Monte Carlo $B^0 \to h^+h^-$ events. The $|cos\Theta_{sph}| < 0.8$ cut was applied.

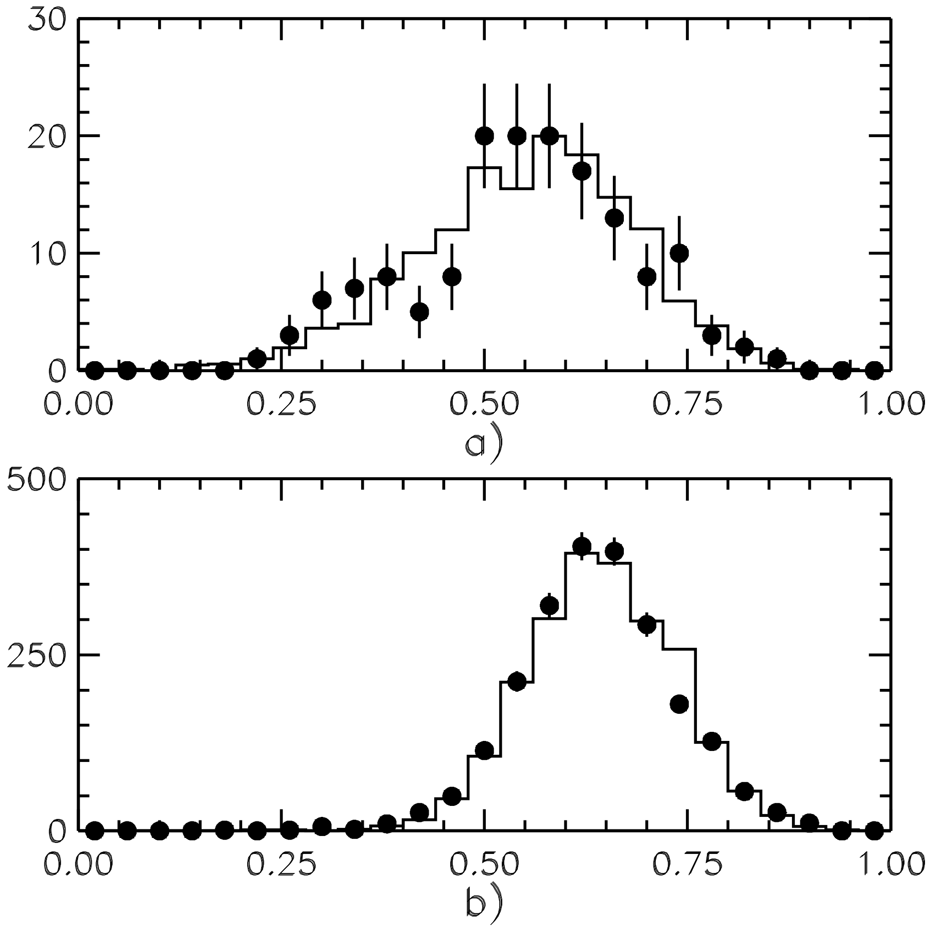

Figure 3.17: Comparison of the $\mathcal{F}$ distributions for the a) $D^0\pi^+$ signal in the data (points) and Monte Carlo (histogram); b) h^+h^- continuum Monte Carlo (solid histogram) and data (points).

CHAPTER 4

MAXIMUM LIKELIHOOD FIT RESULTS

4.1 Introduction

We extract signal yields from the data by performing the unbinned maximum likelihood (ML) fit. We describe the idea of the ML method and its application to the search for the rare B meson decays. In the later sections we present results of our search for rare charmless B decays into $K\pi, \pi\pi$ final states. Throughout this chapter we do not distinguish between B and $\bar{B}$ decays, that is $Br(B^+ \to K^+\pi^0)$ stands for $Br(B^\pm \to K^\pm\pi^0)$ etc.

4.1.1 ML fit basics

The general idea behind the maximum likelihood fit can be described as follows. Let us assume that we have measured a set of N "events", each characterized by several variables $\vec{x^i}$ and we would like to get an estimate for a set of parameters $\vec{f}$. If for given values of $\vec{f}$ the probability density function (PDF) of the i^{th} "event" is $P(\vec{f}, \vec{x^i})$, then the likelihood function is written as

$$\mathcal{L}(\vec{f}, \vec{x}) = \prod_{i=1}^{N} P(\vec{f}, \vec{x^i}) \ . \tag{4.1}$$

The likelihood function measures the cumulative probability of N "events" for the particular choice of parameters $\vec{f}$. Then the estimate of the $\vec{f}$ can be found by maximizing the likelihood function $\mathcal{L}$. In practice one usually chooses to minimize $-2ln\mathcal{L}$, replacing the product with the sum of the logarithms of the individual "event" contributions. We will always refer to $\vec{x}$ as a set of the ML fit variables and $\vec{f}$ as the fit parameters. Further discussion of the maximum likelihood method can be found elsewhere [80].

4.1.2 ML fit procedure

We apply the ML method to our problem in the following way. In general we would like to determine how many signal and background events are in the ON-resonance sample we selected. Selection criteria are mode-dependent and will be described below. We choose M_B, ΔE, Fisher discriminant $\mathcal{F}$, $|cos\Theta_B|$ and dE/dx (where appropriate) as our ML fit variables. Before we describe the fit parameters, let's note that our PID capabilities are far from perfect. This results in the sizable cross-feed between signal events for the modes with charged tracks, such as $K^+\pi^-$ and $\pi^+\pi^-$ for example. Table 4.1 demonstrates migration between related signal modes in the case of h^+h^- analysis. We consider all modes related in this way in one analysis, fitting simultaneously for $K^+\pi^0$ and $\pi^+\pi^0$, for example. Similar decomposition is done for background events as well. It is worthwhile doing, since kaons are less abundant in the continuum than pions. For instance, 30% of the background in the $h^+\pi^0$ mode is of the $K^+\pi^0$ kind. Therefore, background for the $K^+\pi^0$ will be effectively reduced, when PID information for the background

Table 4.1: Misidentification probabilities for the h^+h^- analysis. Both ΔE and dE/dx are used to separate different modes.

Decay mode	$K^+\pi^-$	$K^-\pi^+$	$\pi^+\pi^-$	K^+K^-
$K^+\pi^-$	0.731	0.071	0.106	0.092
$K^-\pi^+$	0.071	0.725	0.123	0.082
$\pi^+\pi^-$	0.093	0.093	0.812	0.001
K^+K^-	0.120	0.106	0.02	0.771

events is taken into account by the ML fit. With these things in mind we write the likelihood contribution from a single event as

$$\begin{aligned} P(\vec{f},\vec{x^i}) &= f^S_{K\pi^0}P^S_{K\pi^0}(\vec{x^i}) + f^S_{\pi\pi^0}P^S_{\pi\pi^0}(\vec{x^i}) + f^C_{K\pi^0}P^C_{K\pi^0}(\vec{x^i}) + \\ &+ (1 - f^S_{K\pi^0} - f^S_{\pi\pi^0} - f^C_{K\pi^0})P^C_{\pi\pi^0}(\vec{x^i}) \ , \end{aligned} \tag{4.2}$$

where $\vec{f} \equiv \{f^S_{K\pi^0},\ f^S_{\pi\pi^0},\ f^C_{K\pi^0}\}$ and $\vec{x^i} \equiv \{M_B,\ \Delta E,\ \mathcal{F},\ |cos\Theta_B|,\ dE/dx\}^i$. $P^S_{\pi\pi^0}(\vec{x^i})$ is written as a product of the PDF's for each of the individual variables for the $\pi\pi^0$ signal hypothesis. We determine PDF for each of the variables for signal and background from data and Monte Carlo. The signal and background fractions $f^S_{K\pi^0}, f^S_{\pi\pi^0}, f^C_{K\pi^0}$ and $f^C_{\pi\pi^0}$ are normalized to satisfy

$$f^S_{K\pi^0} + f^S_{\pi\pi^0} + f^C_{K\pi^0} + f^C_{\pi\pi^0} = 1 \tag{4.3}$$

and are required to be positive during the fit. The signal yield for the $K^+\pi^0$ mode (as an example) is then given by $N_{K\pi^0} = f^S_{K\pi^0} \times N$, where N is the total number of events used in the fit. Likelihood functions for other decay modes are constructed in the similar fashion. By expressing $P^S_{\pi\pi^0}(\vec{x^i})$ as a product of the PDF's for the individual variables we assumed that the ML fit variables are uncorrelated, which is almost always true. We address the question of the correlations later, while discussing systematic errors of the fit.

In the case where the observed signal yields are not statistically significant we calculate the number of events corresponding to the 90% confidence level upper limit N^{UL} as

$$\frac{\int_0^{N^{UL}} \mathcal{L}_{max}(N)dN}{\int_0^{\infty} \mathcal{L}_{max}(N)dN} = 0.9 \ . \tag{4.4}$$

$\mathcal{L}_{max}(N)$ is the maximal $\mathcal{L}$ for the given N.

4.1.3 Selecting events for the fit

Only events from the ON-resonance data sample satisfying the general criteria described in the Chapter 3 are used in the ML fit. We accept events in the region of interest in the $M_B - \Delta E$ plane defined as

$$5.2 < M_B < 5.3 \ GeV/c^2, \ |\Delta E| < 0.2 \ GeV \tag{4.5}$$

for modes without a π^0 in the final state and

$$5.2 < M_B < 5.3 \ GeV/c^2, \ |\Delta E| < 0.3 \ GeV \tag{4.6}$$

for modes involving π^0's.

$|cos\Theta_{sph}|$ cut

We apply the $|cos\Theta_{sph}| < 0.8$ cut for all decay modes . This value was chosen to maximize the probability of measuring $B^0 \to K^+\pi^-$ and $B^0 \to \pi^+\pi^-$ decays separately. As a reminder, previous CLEO results [76, 81] established the existence of the decay $B^0 \to h^+\pi^-$ but due to the limited statistics we were unable to separate individual decay modes. To find the optimal value of the $|cos\Theta_{sph}|$ cut we performed Monte Carlo experiments, generating the appropriate number of signal and background events with correct distributions in all fit variables. Equal branching fractions for $K^+\pi^-$ and $\pi^+\pi^-$ were assumed, which is a worst case scenario for the individual mode measurement. We then performed the ML fit like we would do for the real data and determined the significance of the $K^+\pi^-$ mode for instance. Significance of the signal is defined in the following way. We first perform the basic ML fit to determine the central value of the signal yield and the minimal value of the likelihood function $L_{best} \equiv -2ln\mathcal{L}_{best}$ corresponding to it. To determine the significance of the $K^+\pi^-$ signal, for example, we perform the ML fit with the constraint $f_{K\pi} = 0$ to find the new value of the likelihood function minimum $L_{nosig} \equiv -2ln\mathcal{L}_{nosig}$. Significance is then defined as $S = \sqrt{L_{nosig} - L_{best}}$. It measures how unlikely the "no signal" hypothesis is and for a Gaussian likelihood function S is the number of standard deviations the measured signal is away from zero. Distributions of the $K\pi$ significance in Monte Carlo experiments for the particular choice of the $|cos\Theta_{sph}|$ cut is shown in Figure 4.1.

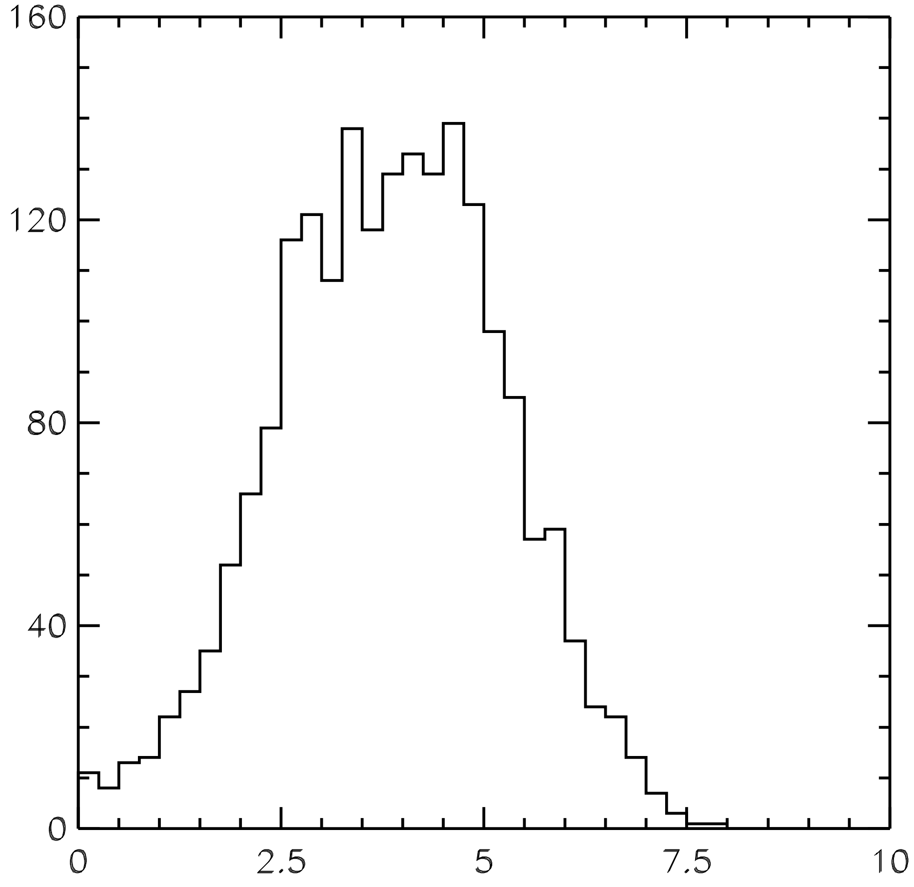

Figure 4.1: Distribution of the $K^+\pi^-$ significance for the $|cos\Theta_{sph}| < 0.8$ determined from Monte Carlo experiments. Average number of generated signal $K^+\pi^-$ events is 13.

$|cos\Theta_{can}|$ cut

We also apply the $|cos\Theta_{can}| < 0.8$ cut for all modes. One can think about this requirement as a detector acceptance cut, since it eliminates events with particles entering detector at small polar angles, where detector resolution deteriorates. We illustrate this point in Figure 4.2, where we plotted ΔE resolution for the $K^+\pi^-$ mode versus $|cos\Theta_{can}|$. We found that loosening $|cos\Theta_{can}|$ requirement beyond 0.8 is not warranted, because higher signal yield is offset by the degraded ΔE resolution and increased background.

With all selection criteria defined, we use Monte Carlo samples of the signal events to determine event selection efficiency for the signal. Table 4.2 lists efficiencies for all modes of interest. Quoted numbers for modes with K_S^0 in the final state include $K^0 \to K_S^0$ and $K_S^0 \to \pi^+\pi^-$ branching fractions.

Table 4.2: Event selection efficiencies for different modes. Errors reflect the systematic uncertainty.

Decay mode	h^+h^-	$h^+K_S^0$	$h^+\pi^0$	$K_S^0\pi^0$	$\pi^0\pi^0$
Efficiency (%)	44 ± 3	12 ± 1	37 ± 3	8 ± 1	29 ± 3

4.1.4 PDF shapes

We determine PDF shapes for the ML fit variables from data (when possible) and Monte Carlo.

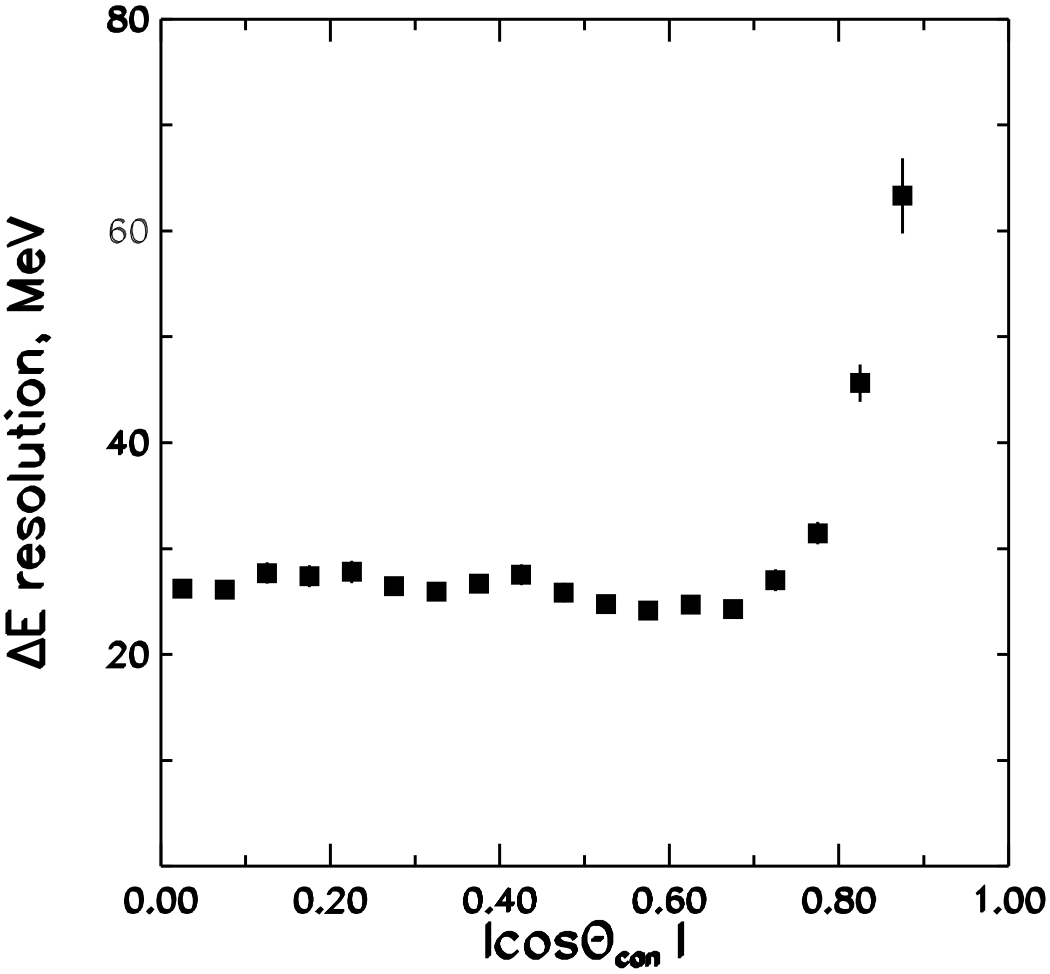

Figure 4.2: ΔE resolution dependence on $|cos\Theta_{can}|$ for the $K^+\pi^-$ mode.

All shapes for the signal fit variables, except dE/dx, are taken from Monte Carlo. We use bifurcated Gaussians to parameterize M_B, ΔE and Fisher discriminant (Figure 4.3) distributions. The $|cos\Theta_B|$ shape is well described by the second order polynomial.

We use OFF-resonance data combined with the sideband($M_B < 5.27$) of the ON-resonance sample to determine corresponding PDF shapes for the background. M_B distribution for the continuum(Figure 4.4) is described by the ARGUS function (defined in the previous chapter). We convolute the ARGUS function at the endpoint with a Gaussian with 1 MeV σ to account for the CESR beam energy spread. ΔE and $|cos\Theta_B|$ continuum shapes are described well by the straight line. Fisher discriminant for continuum is parameterized by the sum of two bifurcated Gaussians.

dE/dx shapes for high momentum (2.3 - 2.9 GeV/c) kaons and pions were found from the tagged D^0 decays [82]. Figure 4.5 shows dE/dx information for true kaons and pions in this sample. As can be seen from the plot, there are small differences between distributions for the positively and negatively charged particles. We take this into account in our fit procedure by using separate dE/dx parameterizations for K^+ and K^- etc.

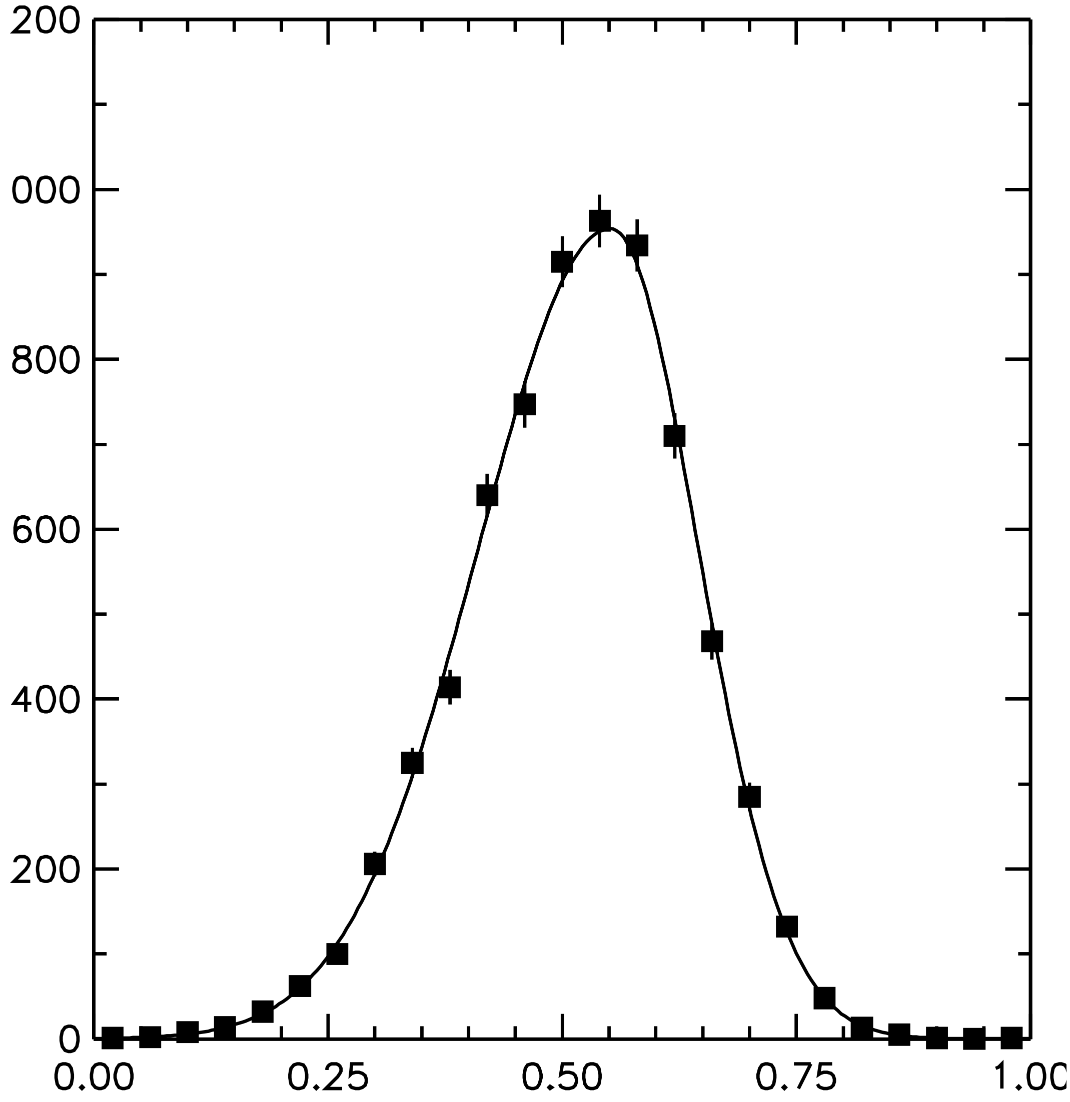

Figure 4.3: Fisher discriminant distribution for the h^+h^- signal determined from Monte Carlo.

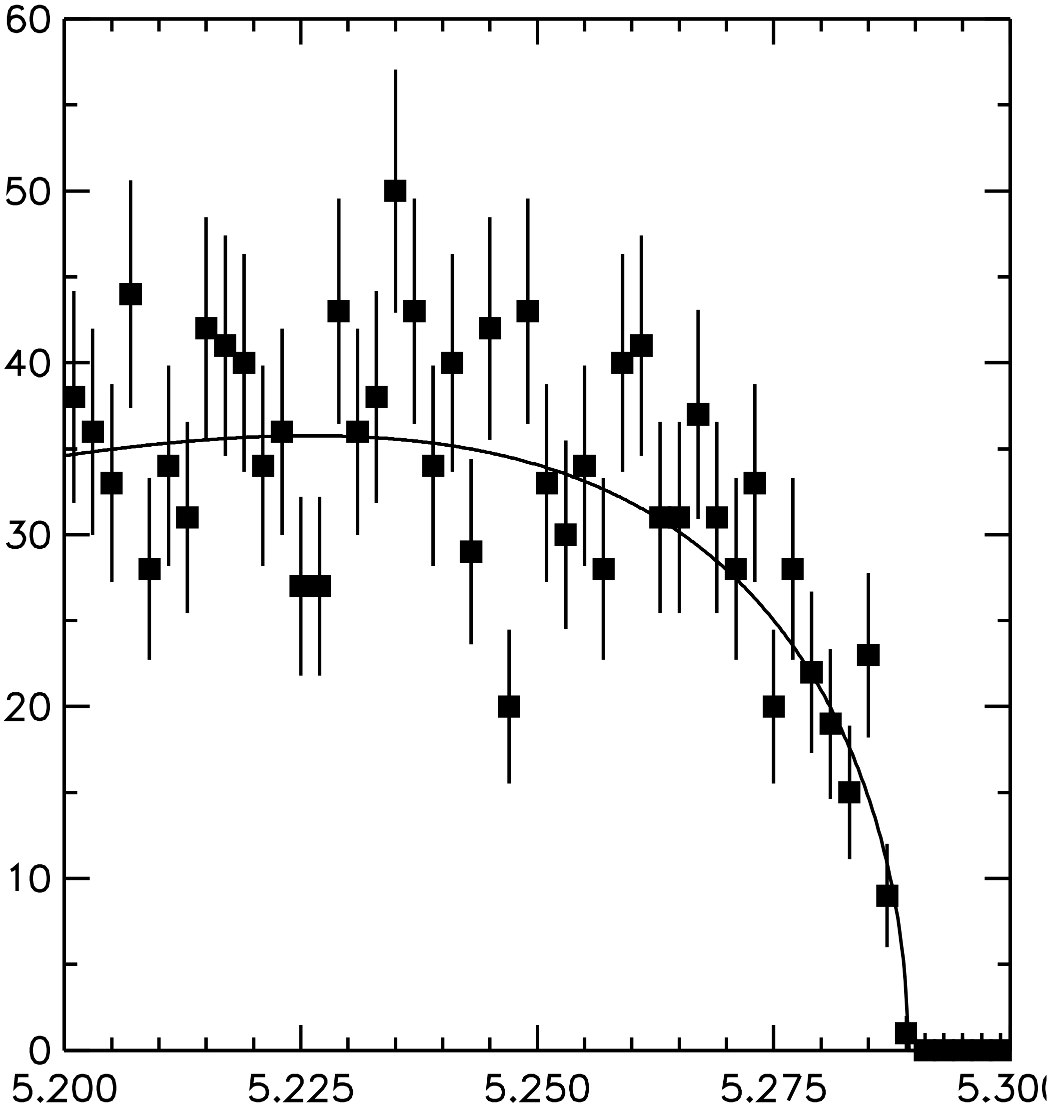

Figure 4.4: Shape of the M_B distribution for $h^+\pi^0$ events determined from the OFF-resonance data sample.

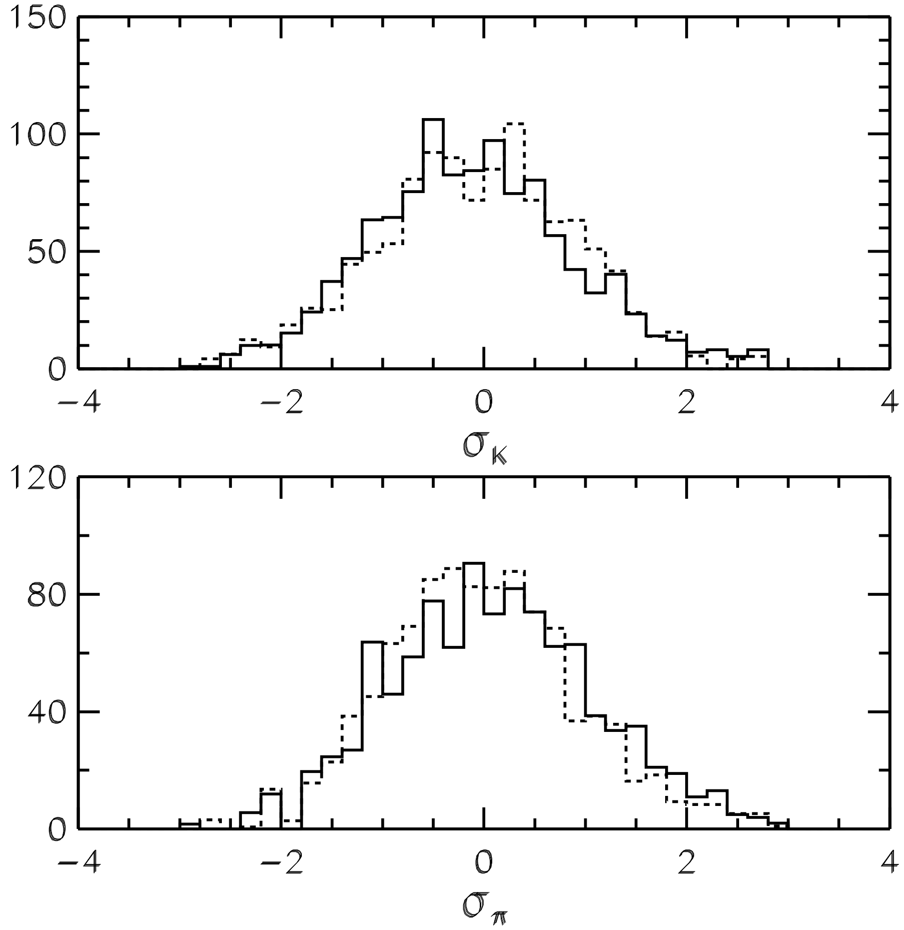

Figure 4.5: dE/dx distributions for K (top) and π (bottom) in the 2.3 - 2.9 GeV/c momentum range in the data. Solid histograms are for K^+ (π^+), dashed histograms for K^- (π^-) .

4.2 $B^0 \to K^+\pi^-/\pi^+\pi^-/K^+K^-$

4.2.1 Fit results

We select 1547 events from the ON-resonance data sample for the ML fit. Fitting for the number of $K\pi$ ($K^+\pi^-$ and $K^-\pi^+$ combined) and $\pi\pi$ signal events gives

- $N_{K\pi} = 21.6^{+6.8}_{-6.0}$, 5.6σ
- $N_{\pi\pi} = 9.9^{+6.0}_{-5.1}$, 2.2σ ,

where we also quoted the significance of the signal. The contour plot of the likelihood function in the $N_{K\pi} - N_{\pi\pi}$ plane, is shown in Figure 4.6. Note that the $K\pi$ central value is clearly more than 5σ away from zero, while evidence for the $\pi\pi$ remains at the 2.2σ level. To further illustrate results of the fit , we project events used in the ML fit onto the M_B and ΔE variables. To make an M_B projection for example, we apply cuts on ΔE and Fisher discriminant to remove most of the background events. While making the projection for the $K\pi(\pi\pi)$ signal, we require events to have dE/dx information favoring the $K\pi(\pi\pi)$ hypothesis. Overall efficiency of these extra cuts (M_B projection as an example) is $\sim 2\%$ for the background and $\sim 50\%$ for the signal. The resulting distributions are shown in Figures 4.7 - 4.8. Superimposed curves are obtained by taking the probability density functions as used by the ML fit and rescaling them to account for the expected loss of efficiency due to the extra cuts. We observe nice peaks in M_B and ΔE for $K\pi$ signal component and note good agreement between the actual distributions and the ML fit projections. We also plot all events used in the fit and satisfying

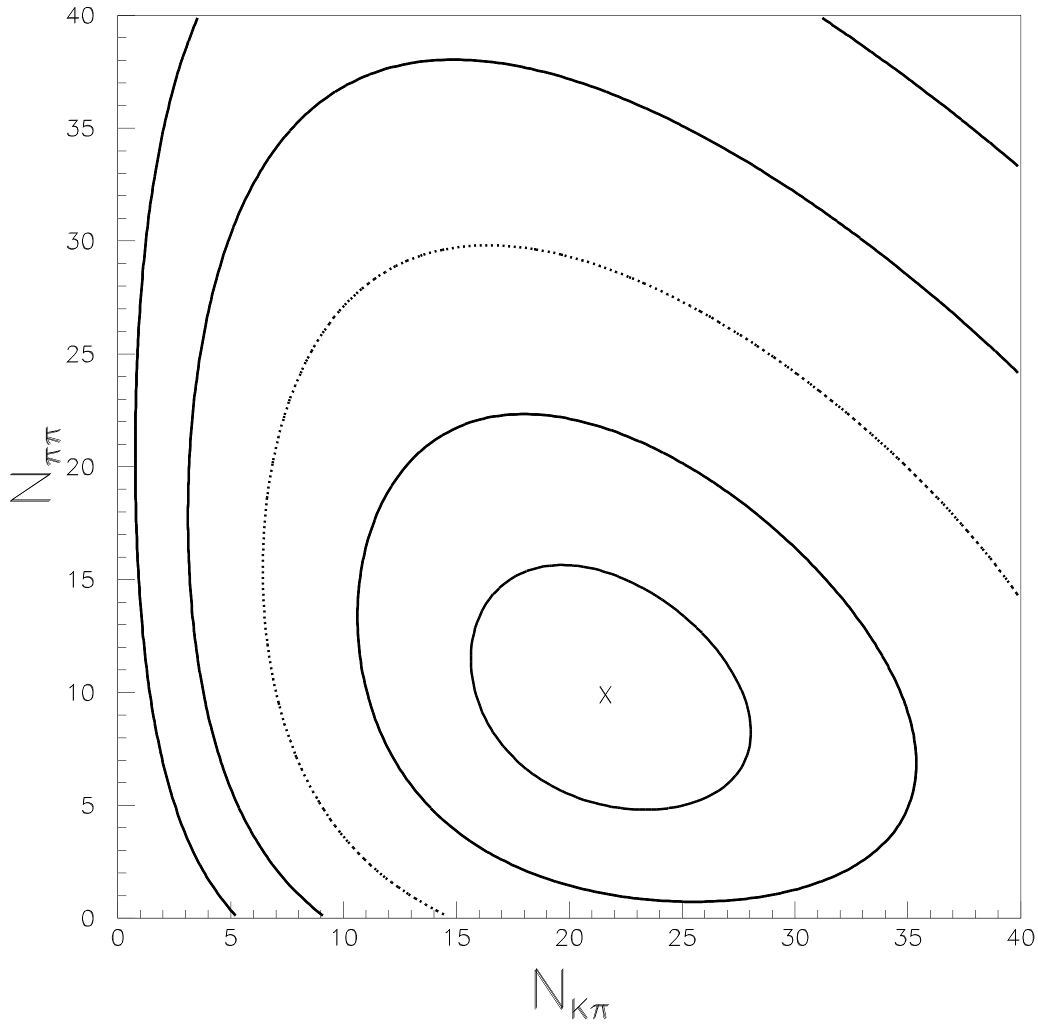

Figure 4.6: Contours of $-2ln\mathcal{L}$ in the $N_{K\pi} - N_{\pi\pi}$ plane. 3σ contour is represented by the dotted line.

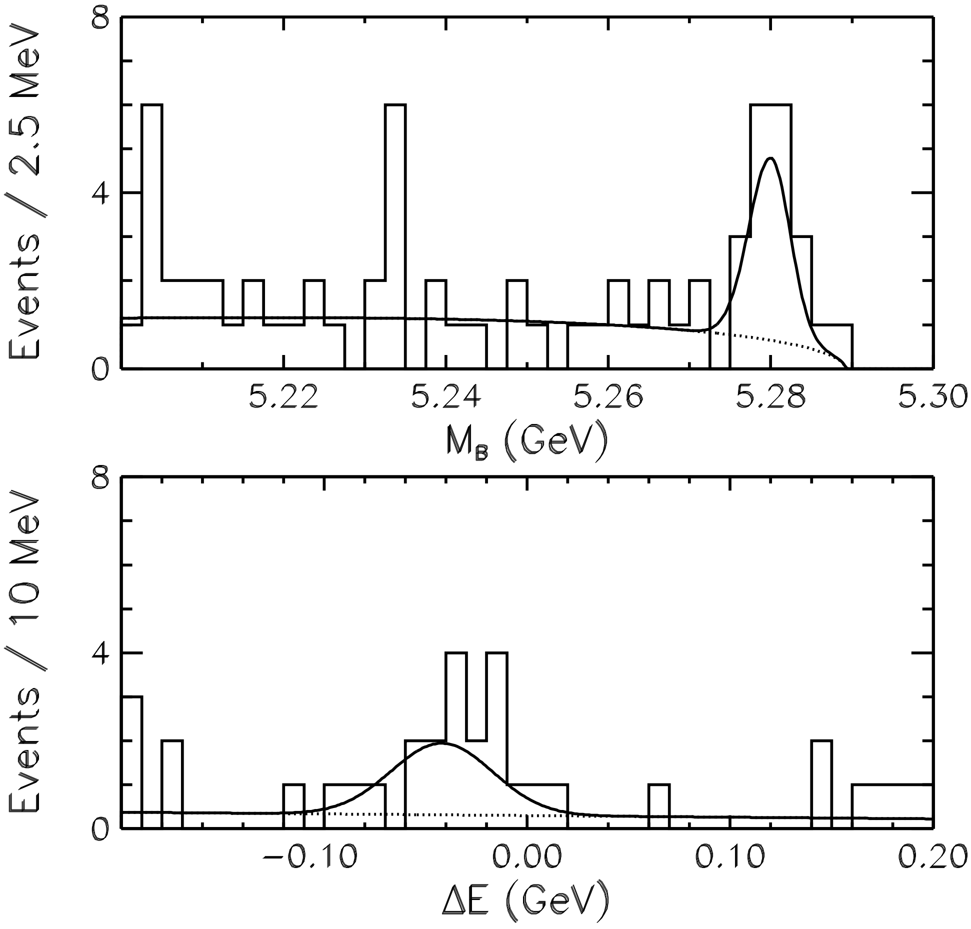

Figure 4.7: M_B and ΔE distributions for $K\pi$ events.

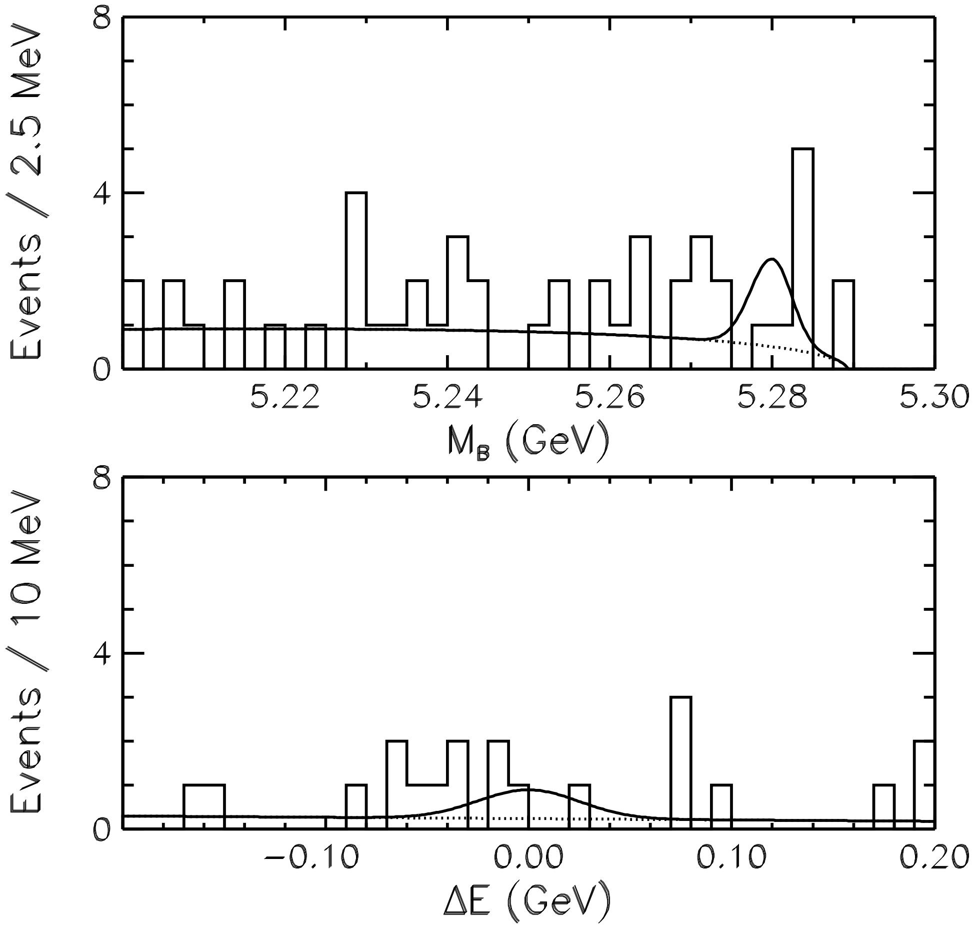

Figure 4.8: M_B and ΔE distributions for $\pi\pi$ events.

the $\mathcal{F} < 0.6$ cut in the M_B - ΔE plane, as shown in Figure 4.9.

The measured $K\pi$ signal yield translates into the branching fraction of

$$Br(B^0 \to K^+\pi^-) = 1.5^{+0.5}_{-0.4} \times 10^{-5} ,$$

where we used selection efficiency of 44% and number of $B\bar{B}$ events $N_{B\bar{B}} = 3.3 \times 10^6$. We establish 90% confidence level upper limit of $N^{UL}_{\pi\pi} = 18.5$ using method defined by Eq. 4.4.

4.2.2 Consistency checks

We performed numerous checks to see how stable our results are.

KK signal

The ML fit described above didn't have the K^+K^- signal fraction included. This has mainly historical reasons, since the expected branching fraction is negligible and all previous CLEO results were insensitive to the K^+K^- presence in the fit. To be fair and also to set an upper limit for the $B^0 \to K^+K^-$ decay, we repeat the analysis allowing for the signal KK component. We find

- $N_{K\pi} = 21.6^{+6.8}_{-6.0}$, 5.6σ
- $N_{\pi\pi} = 9.9^{+6.0}_{-5.1}$, 2.2σ
- $N_{KK} = 0.0^{+1.3}_{-0.0}$, 0.0σ .

As one can see, results for $N_{K\pi}$ and $N_{\pi\pi}$ remain the same. We calculate 90% C.L. upper limit for N_{KK} to be $N^{UL}_{KK} = 5.1$.

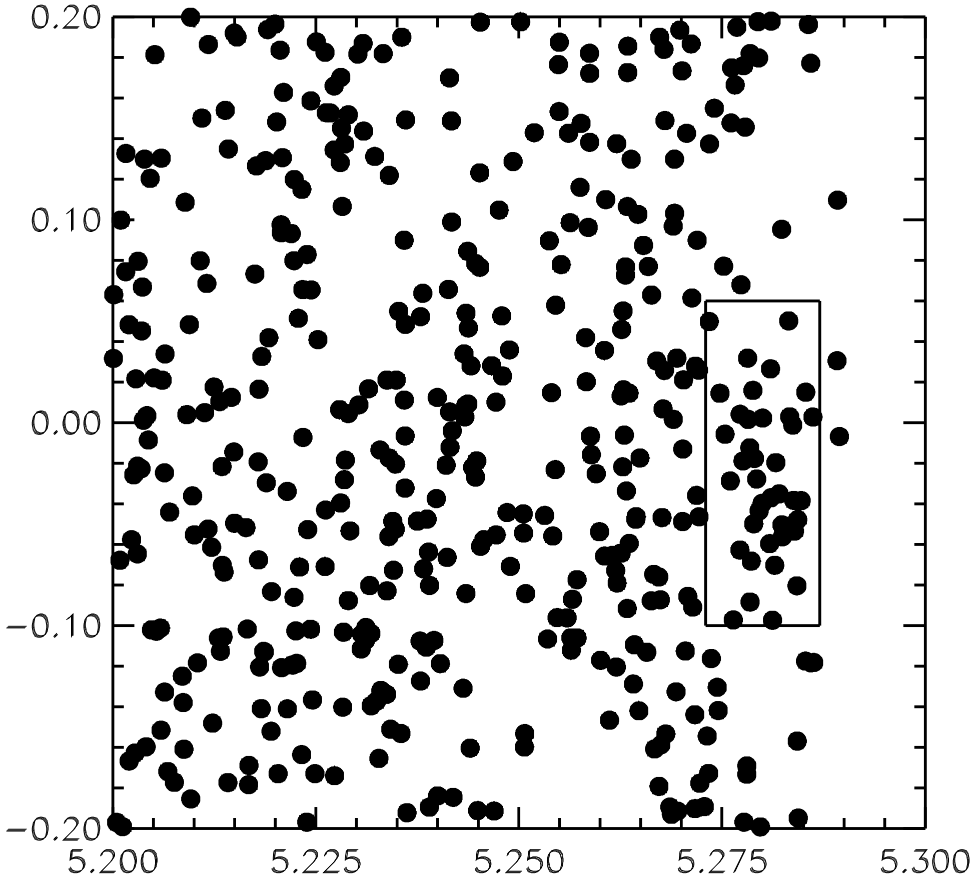

Figure 4.9: M_B - ΔE scatter plot for events used in the $B^0 \rightarrow h^+h^-$ analysis. The $\mathcal{F} < 0.6$ cut was applied.

OFF-resonance data

We fitted the OFF-resonance data sample of 869 events. As expected, signal yields for the B meson free sample are consistent with 0:

- $N_{K\pi} = 0.0^{+1.4}_{-0.0}$
- $N_{\pi\pi} = 0.0^{+1.9}_{-0.0}$.

$|cos\Theta_{sph}|$ dependence

We check our results against variations in the $|cos\Theta_{sph}|$ cut by performing fits of the samples corresponding to the $|cos\Theta_{sph}|$ cut values of 0.7 and 0.9. This translates approximately into a reduction (increase) of the number of background events in the fit by a factor of 2. Since the Fisher discriminant distribution depends on the $|cos\Theta_{sph}|$ cut value, we reevaluated $\mathcal{F}$ shapes for these fits. Obviously signal reconstruction efficiency had to be adjusted as well. Fitting the "low-background" sample of $|cos\Theta_{sph}| < 0.7$ consisting of 868 events we get

- $N_{K\pi} = 19.0^{+6.1}_{-5.3}$, 5.6σ
- $N_{\pi\pi} = 8.5^{+5.4}_{-4.5}$, 2.1σ
- $Br(B^0 \to K^+\pi^-) = 1.52^{+0.48}_{-0.42} \times 10^{-5}$.

For the "high-background" sample of $|cos\Theta_{sph}| < 0.9$, with 3265 events in the fit we obtain

- $N_{K\pi} = 26.0^{+8.2}_{-7.2}$, 5.6σ

- $N_{\pi\pi} = 14.3^{+7.6}_{-6.6}$, 2.4σ

- $Br(B^0 \to K^+\pi^-) = 1.54^{+0.48}_{-0.43} \times 10^{-5}$.

Again, there is a remarkable agreement among various fits. We conclude that ML fit distinguishes signal from the background very well.

ML fit without dE/dx information

In principle it is possible that the large $K\pi$ signal is due to some anomalous distribution of the dE/dx for signal events. We therefore repeated the fit without using dE/dx information:

- $N_{K\pi} = 23.7^{+8.1}_{-7.3}$, 4.0σ

- $N_{\pi\pi} = 8.2^{+7.2}_{-6.1}$, 1.4σ .

Agreement with our main result is quite good. In principle one should have expected that, given the ΔE distribution in Figure 4.7, where the peak position strongly favors the $K\pi$ hypothesis.

ML fit without ΔE

Analogously to the previous case, we also checked what happens if we drop the ΔE variable from the fit. In this case we measure

- $N_{K\pi} = 15.6^{+9.3}_{-8.3}$, 3.7σ

- $N_{\pi\pi} = 13.7^{+8.9}_{-8.8}$, 1.9σ

which still agrees quite well with our main result.

ML fit without Fisher discriminant

For the final test we drop the Fisher discriminant from the fit. In this case signal yields become

- $N_{K\pi} = 20.3^{+6.6}_{-6.1}$, 4.7σ
- $N_{\pi\pi} = 7.2^{+5.8}_{-4.9}$, 1.6σ .

This proves that signal is not "manufactured" by the tail of the Fisher discriminant distribution.

In conclusion, we verified that the signal yields as given by the maximum likelihood fit are stable and robust with respect to different fit scenarios. None of the variations we tried was able to destroy the observed $K\pi$ signal or to push the $\pi\pi$ signal beyond the 3σ threshold. We have established that the central values of the signals and their significances are not dominated by the tails of distributions for any of the fit variables.

4.2.3 Systematic errors for the h^+h^- analysis

The errors on the signal yields given in the previous section are due to statistics only. Systematic errors of our measurements come from two major sources. First, our maximum likelihood fit procedure may be biased. Second, we determine reconstruction efficiency for the signal from Monte Carlo, by applying our event selection criteria to the large sample of the Monte Carlo generated events. Since our detector simulation package is not perfect, the reconstruction efficiency has its own systematic uncertainty listed in Table 4.2.

Systematics of the fit

There are several effects which can make the ML fit to produce incorrect results. In principle, the ML fit estimator is unbiased only in the limit of infinite statistics. Using Monte Carlo generated experiments we verified that while the number of signal events in our analysis is not very large, the ML fit produces an unbiased estimate.

While constructing the likelihood function we assumed that all fit variables are uncorrelated. We measured correlations between the ML fit variables and found that the only noticeable correlation is between M_B and ΔE variables for the signal events, which we found to be -0.17. In order to estimate this affects the ML fit we again used Monte Carlo generated experiments, where we produced signal events with the correct $M_B - \Delta E$ correlation, but fitted them under assumption of no correlation. In this way we estimated the resulting bias to be at most -1.5% for the $K^+\pi^-$ yield.

The most important systematics of the ML fit come from our imperfect knowledge of the PDF shapes for the fit variables. In order to determine the corresponding systematic error, we varied all the parameters describing the PDF shapes within reasonable limits, determined by their errors or from the comparison between data and MC. Table 4.3 lists the dominant contributions to the $K^+\pi^-$ signal yield and upper limits for the $\pi^+\pi^-$ and K^+K^- signal. Some of the systematic variations are illustrated in Figures 4.10 - 4.11. Overall systematic error is then determined by adding all individual contributions in quadrature.

For the $\pi^+\pi^-$ and K^+K^- modes we evaluate the effect of the fit systematics

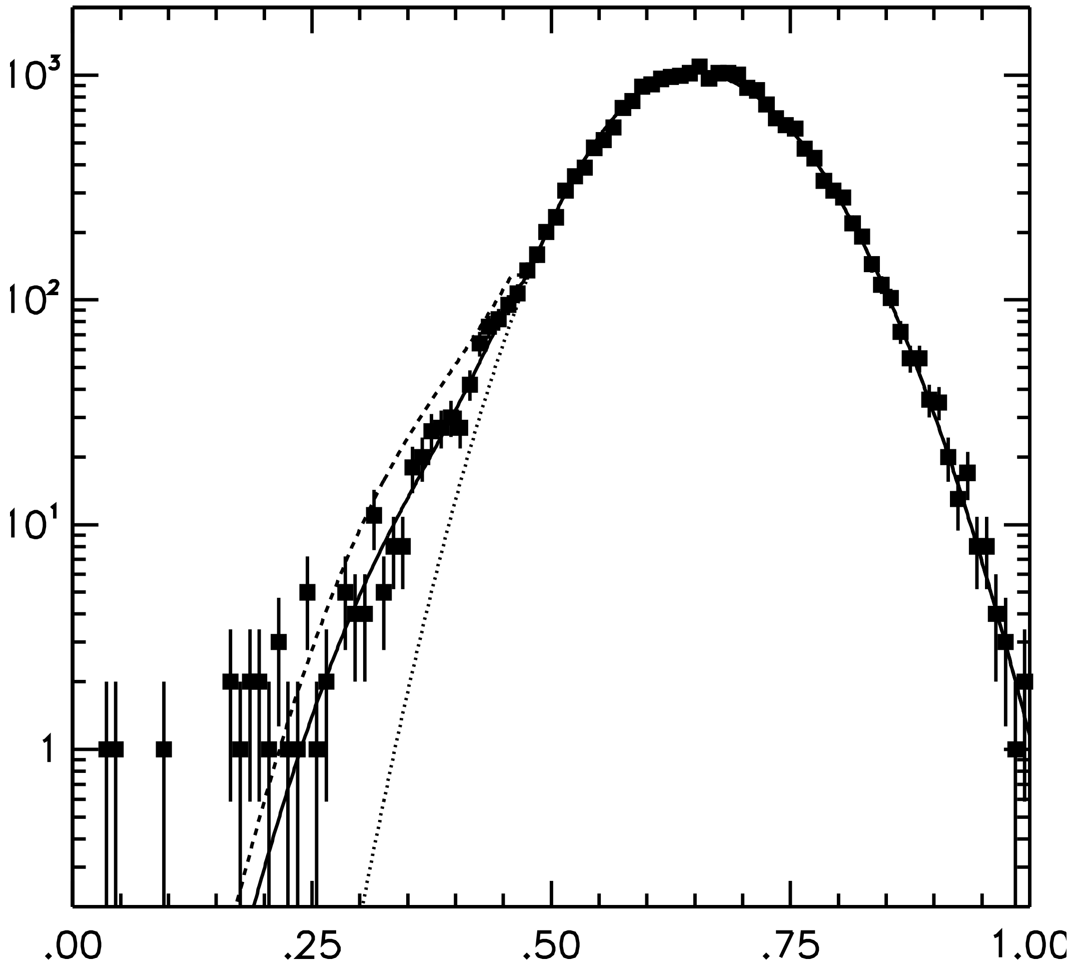

Figure 4.10: Systematic variations in the tail of the Fisher discriminant distribution for the background.

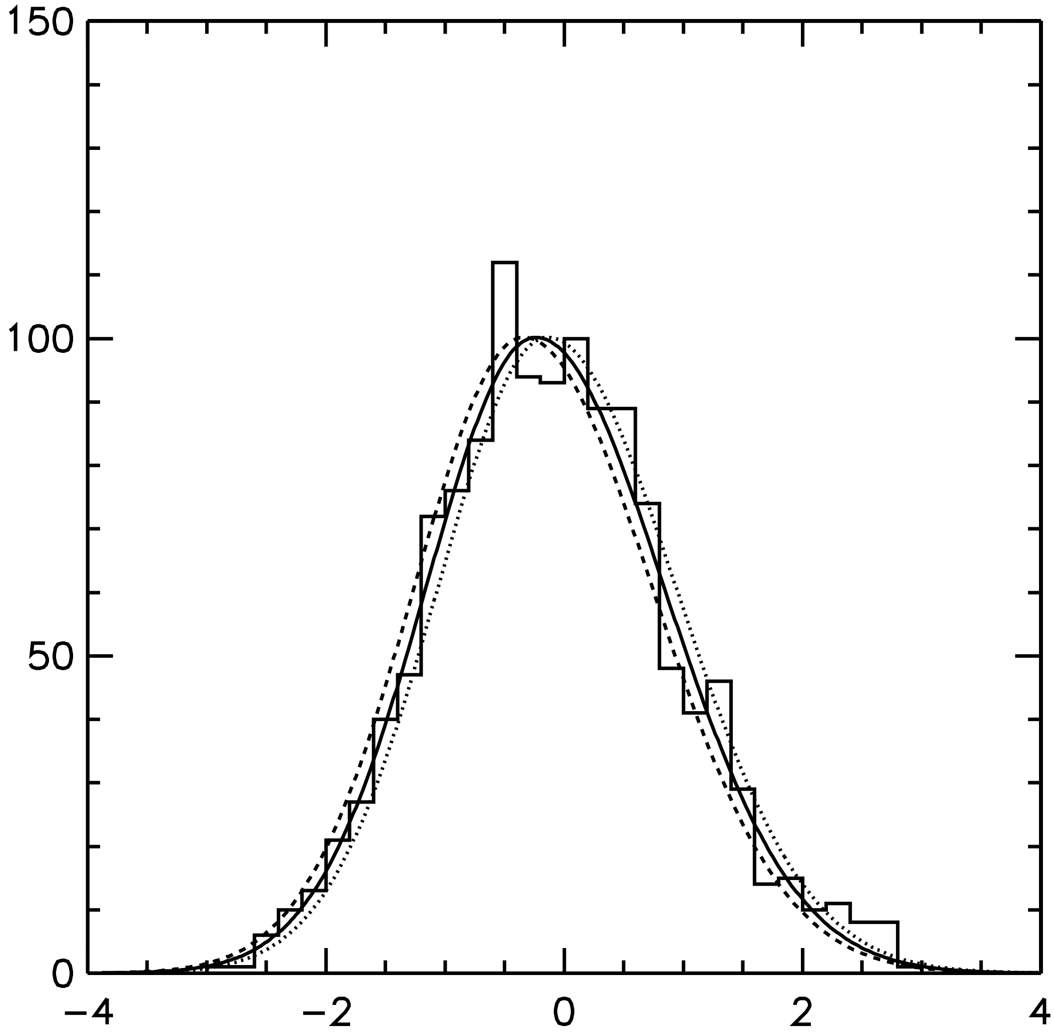

Figure 4.11: Systematic variation for the means of the dE/dx distributions.

Table 4.3: Change in the signal yield ($K^+\pi^-$ mode) and upper limits ($\pi^+\pi^-$ and K^+K^- modes) for systematic variations of the fit parameters.

Parameter variation	$\Delta N_{K\pi}$	$\Delta N^{UL}_{\pi\pi}$	ΔN^{UL}_{KK}
M_B background:			
$\lambda = -17.9 \pm 3.7$	±0.5	0.5	0.1
$E_{beam} = 5.2892 \pm 0.001$	±0.4	0.7	-
M_B signal:			
$\sigma^{low}_{MB} = 2.7 \pm 0.1$, $\sigma^{high}_{MB} = 2.4 \pm 0.1$	-0.1	0.1	0.1
$M_B = 5.28 \pm 0.0003$	$^{+0.1}_{-0.3}$	-	0.2
ΔE signal:			
$\sigma_{\Delta E} = 27 \pm 2$ MeV	-0.2	0.6	-
Nominal $\Delta E \pm 3$ MeV	$^{+0.5}_{-0.7}$	0.9	0.2
$< \mathcal{F}^{sig} >= 0.547,\ \sigma^{low} = 0.147,\ \sigma^{high} = 0.087$	-0.6	-	-
$< \mathcal{F}^{sig} >= 0.559,\ \sigma^{low} = 0.135,\ \sigma^{high} = 0.095$	$+0.5$	0.3	0.3
$< \mathcal{F}^{bkg} >= 0.644,\ \sigma^{low} = 0.083,\ \sigma^{high} = 0.1$	$+0.6$	1.2	0.2
$< \mathcal{F}^{bkg} >= 0.623,\ \sigma^{low} = 0.076,\ \sigma^{high} = 0.098$	-	-	-
Area of the tail $(1.2 \pm 1.2)\%$	$^{+1.1}_{-0.9}$	0.9	0.2
dE/dx: Shift all means ±0.1	$^{+0.9}_{-1.1}$	1.1	0.6
Shift separation of means ±0.2	-0.1	0.2	0.2
Shift all sigmas ±0.1	$^{+0.1}_{-0.3}$	0.2	0.2
Total systematic error:	$^{+1.8}_{-1.9}$	2.4	0.8

on the N^{UL}. When calculating branching fraction upper limit we increase N^{UL} by its systematic error and also reduce the reconstruction efficiency by its systematic error.

4.2.4 Final results

Taking systematic errors into account we measure branching fraction for the decay $B^0 \to K^+\pi^-$ to be $(1.5^{+0.5+0.1}_{-0.4-0.1} \pm 0.1) \times 10^{-5}$. The first error is statistical, second is due to the systematics of the ML fit and the last comes from the systematic uncertainty in the event selection efficiency. We do not observe a statistically significant signal in the $\pi^+\pi^-$ or K^+K^- modes and therefore calculate 90% C.L. upper limits for these modes

- $Br(B^0 \to \pi^+\pi^-) < 1.5 \times 10^{-5}$
- $Br(B^0 \to K^+K^-) < 4.3 \times 10^{-6}$.

4.3 $B^+ \to K^+\pi^0/\pi^+\pi^0$

A selected sample of 1930 events is fitted to determine the fractions of $K^+\pi^0$ and $\pi^+\pi^0$ signal events. The same fit variables are used, with the only difference that the dE/dx information for only one track is present. The fit results are given below:

- $N_{K\pi^0} = 8.7^{+5.3}_{-4.2}$, 2.7σ
- $N_{\pi\pi^0} = 11.3^{+6.3}_{-5.2}$, 2.8σ

- $N_{h\pi^0} = 20.0^{+6.8}_{-5.9}$, 5.5σ .

Corresponding likelihood function contours are shown in Figure 4.12. Figure 4.13 shows M_B and ΔE projection plots for the $h^+\pi^0$ mode ($K^+\pi^0$ and $\pi^+\pi^0$ events combined). As usual, we imposed extra cuts and overlayed the predictions from the ML fit. Similar plots for the individual modes are shown in Figures 4.14 ($K^+\pi^0$) and 4.15 ($\pi^+\pi^0$). The M_B - ΔE scatter plot is shown in Figure 4.16.

Since both $K^+\pi^0$ and $\pi^+\pi^0$ signals are not statistically significant, we compute 90% C.L. upper limits for individual signals and calculate the branching fraction for their sum:

- $N^{UL}_{K\pi^0} = 16.2$
- $N^{UL}_{\pi\pi^0} = 20.0$
- $Br(B^+ \to h^+\pi^0) = 1.6^{+0.6}_{-0.5} \times 10^{-5}$.

4.3.1 Consistency checks

We performed several tests to verify stability of the signal.

$|cos\Theta_{sph}|$ dependence

Repeating the fit with $|cos\Theta_{sph}| < 0.7$ cut (1046 events) we find

- $N_{K\pi^0} = 7.1^{+4.5}_{-3.5}$, 2.8σ
- $N_{\pi\pi^0} = 9.8^{+5.5}_{-4.5}$, 3.0σ

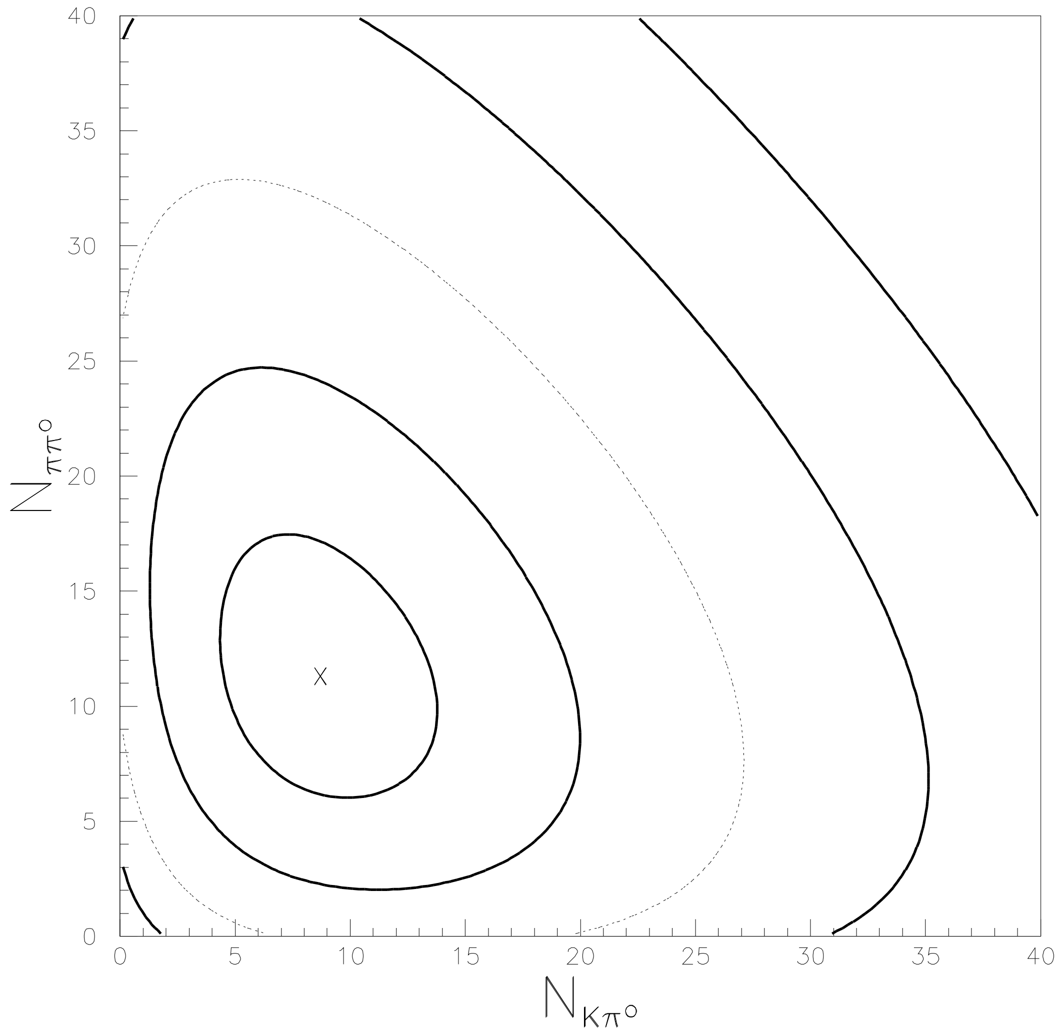

Figure 4.12: Contours of $-2ln\mathcal{L}$ in the $N_{K\pi^0} - N_{\pi\pi^0}$ plane. The 3σ contour is represented by the dotted line.

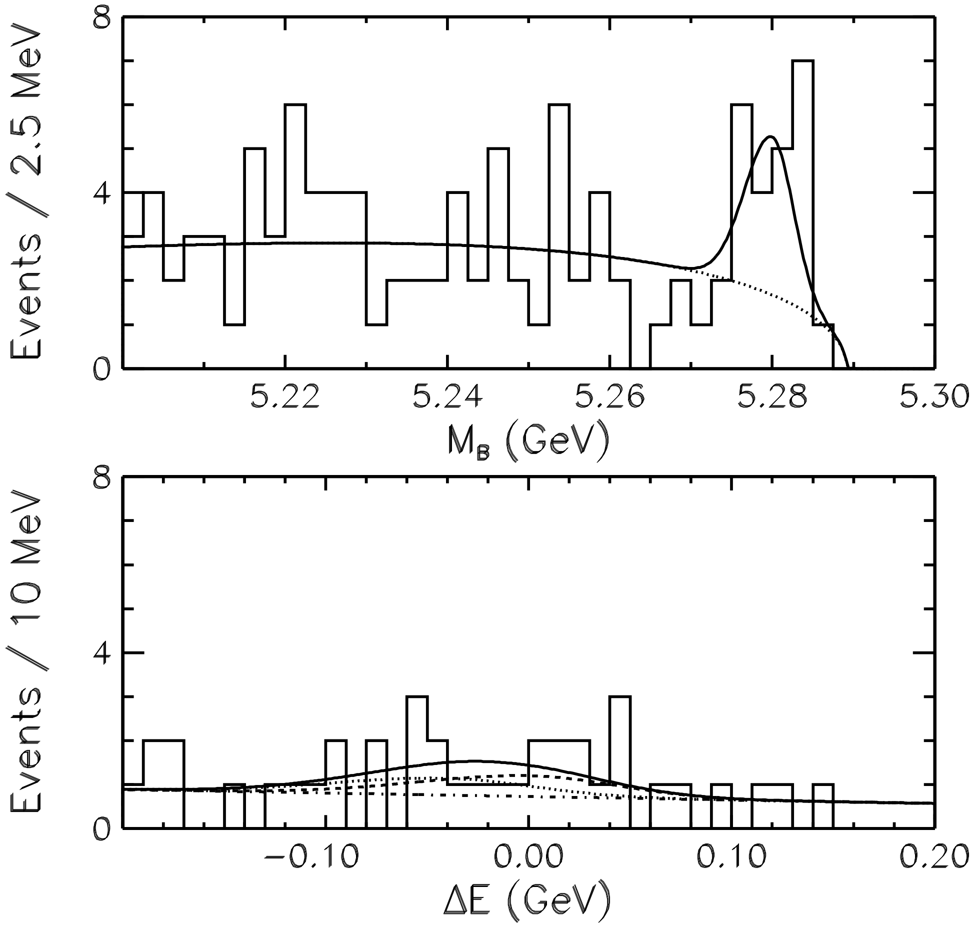

Figure 4.13: Projections of the ML fit sample onto M_B and ΔE variables for the $h^+\pi^0$ decay mode. Scaled ML fit predictions are overlayed

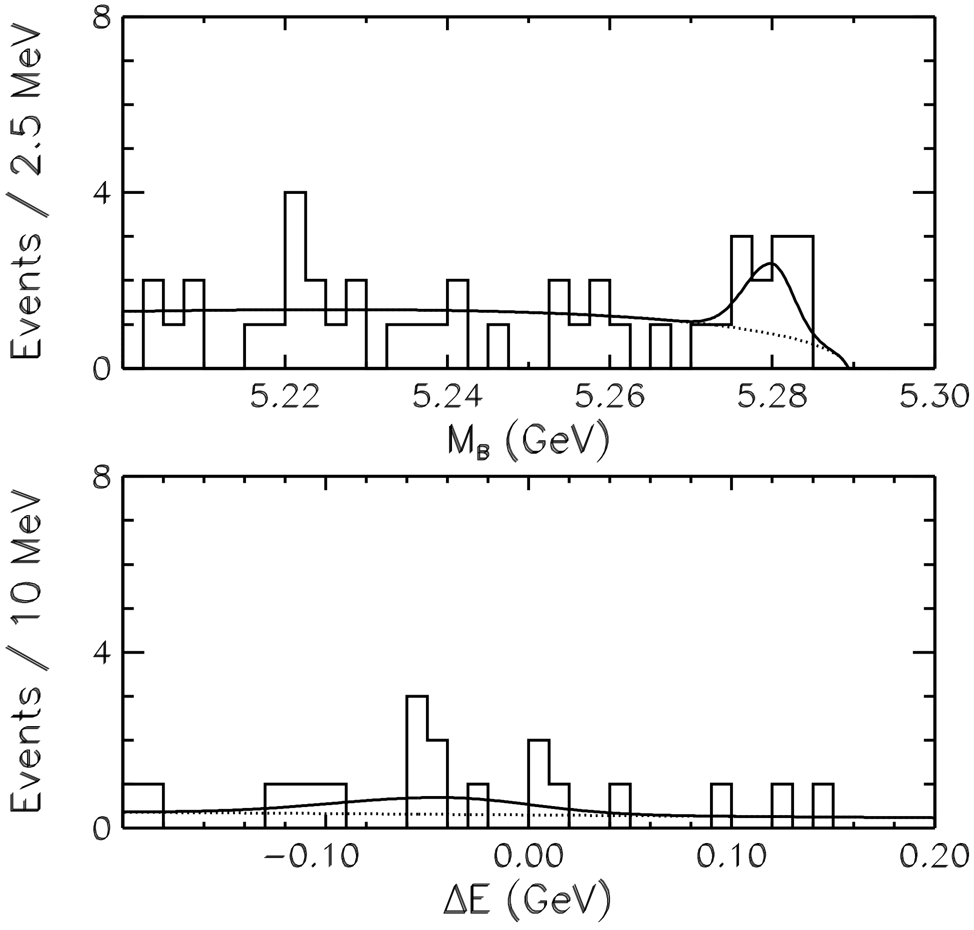

Figure 4.14: Projections of the ML fit sample onto M_B and ΔE variables for the $K^+\pi^0$ decay mode. Scaled ML fit predictions are overlayed.

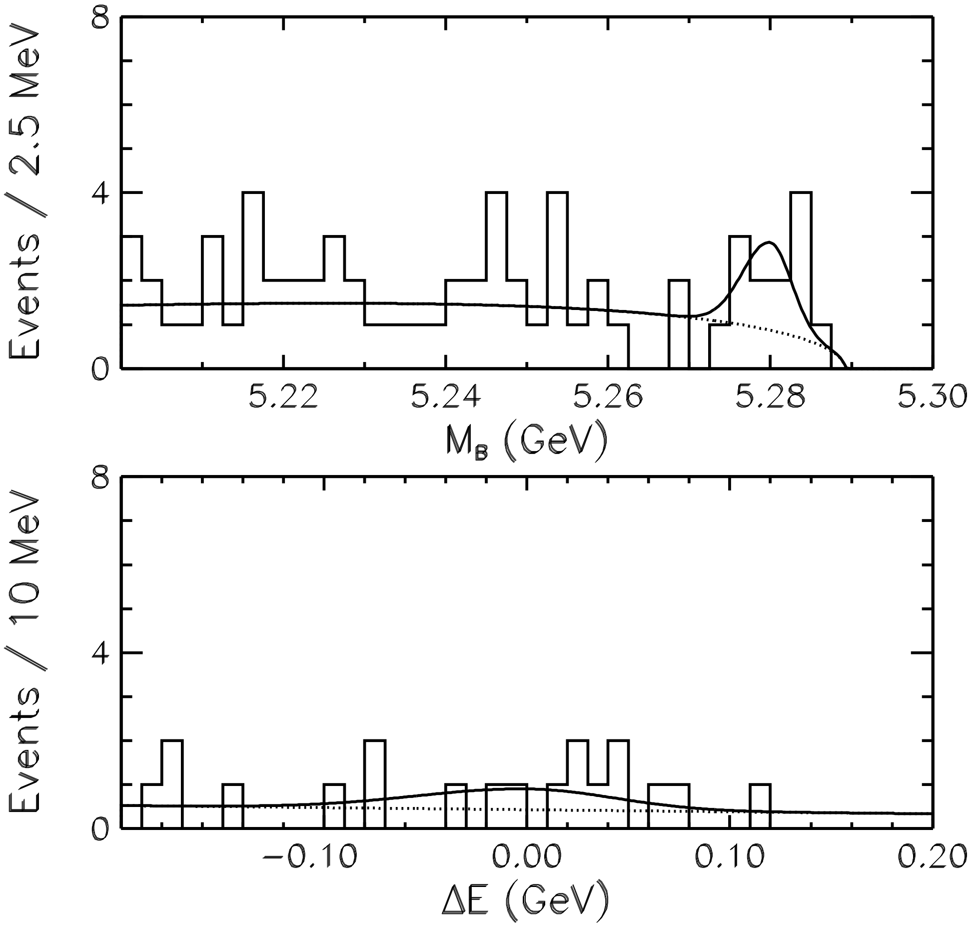

Figure 4.15: Projections of the ML fit sample onto M_B and ΔE variables for the $\pi^+\pi^0$ mode. Scaled ML fit predictions are overlayed.

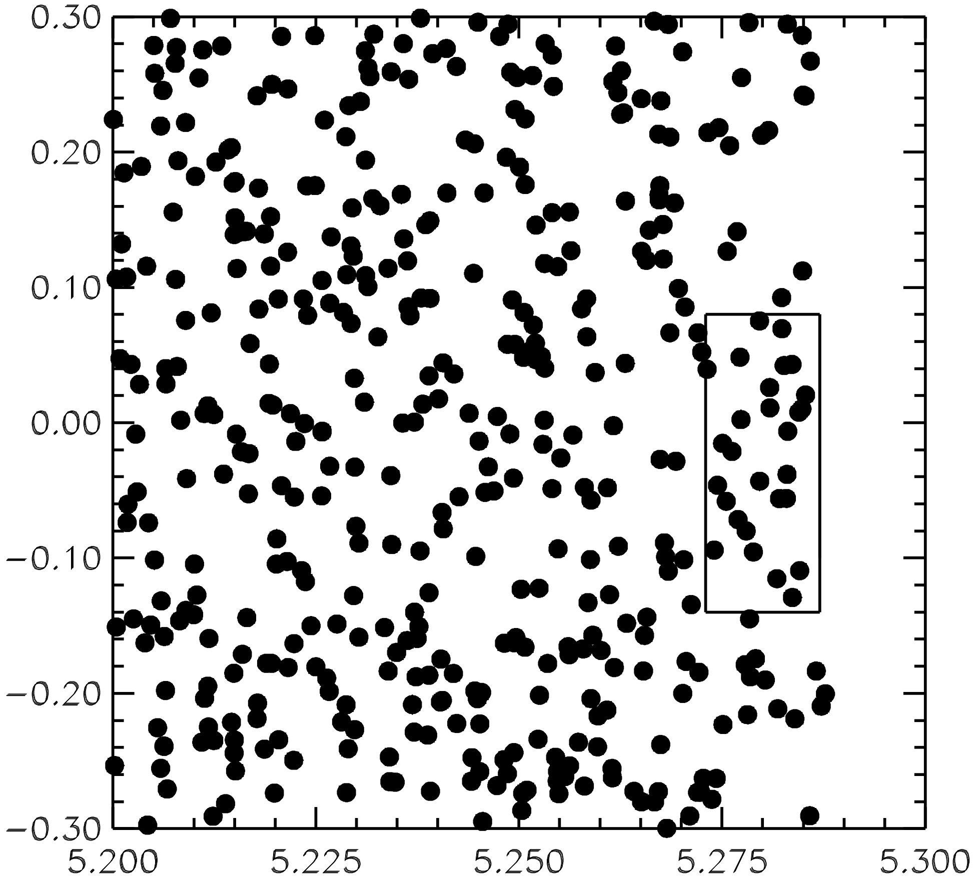

Figure 4.16: M_B - ΔE scatter plot for events used in the $B^+ \rightarrow h^+\pi^0$ analysis. The $\mathcal{F} < 0.6$ cut was applied.

- $N_{h\pi^0} = 16.9^{+5.9}_{-5.0}$, 6.0σ .

For the $|cos\Theta_{sph}| < 0.9$ cut (4326 events) the fit gives:

- $N_{K\pi^0} = 12.5^{+7.1}_{-5.8}$, 2.8σ
- $N_{\pi\pi^0} = 11.9^{+7.8}_{-6.5}$, 2.1σ
- $N_{h\pi^0} = 24.4^{+8.8}_{-7.7}$, 4.8σ .

Fisher discriminant tails

The long standing issue in the $h^+\pi^0$ analysis is the presence of several events in the tail of the Fisher discriminant distribution, shown in Figure 4.17. 7 events are found with Fisher discriminant value below 0.4 . In our previous publication [76] the same 7 events in the tail were present, but we had only 10 signal events in the $h^+\pi^0$ mode. At that time we felt very strongly that having 7 out of 10 events in the tail is very unlikely and quoted only the branching fraction upper limit.

Now, with the addition of new data and relaxing of the cuts, we have 20 signal events with the same 7 events in the tail of the Fisher discriminant distribution. We examined all of the events in the tail in great detail and found no outstanding problems. In fact, in one of the events, shown in Figure 4.18, we were able to reconstruct the other B meson. The reconstructed decay chain for the second B meson in the event is $B^- \to D^{*0}\mu^-\nu, D^{*0} \to D^0\gamma, D^0 \to K^-\pi^+$. The neutrino is reconstructed by the missing invariant mass of the event. Detailed characteristics of this event are given in the Appendix B.

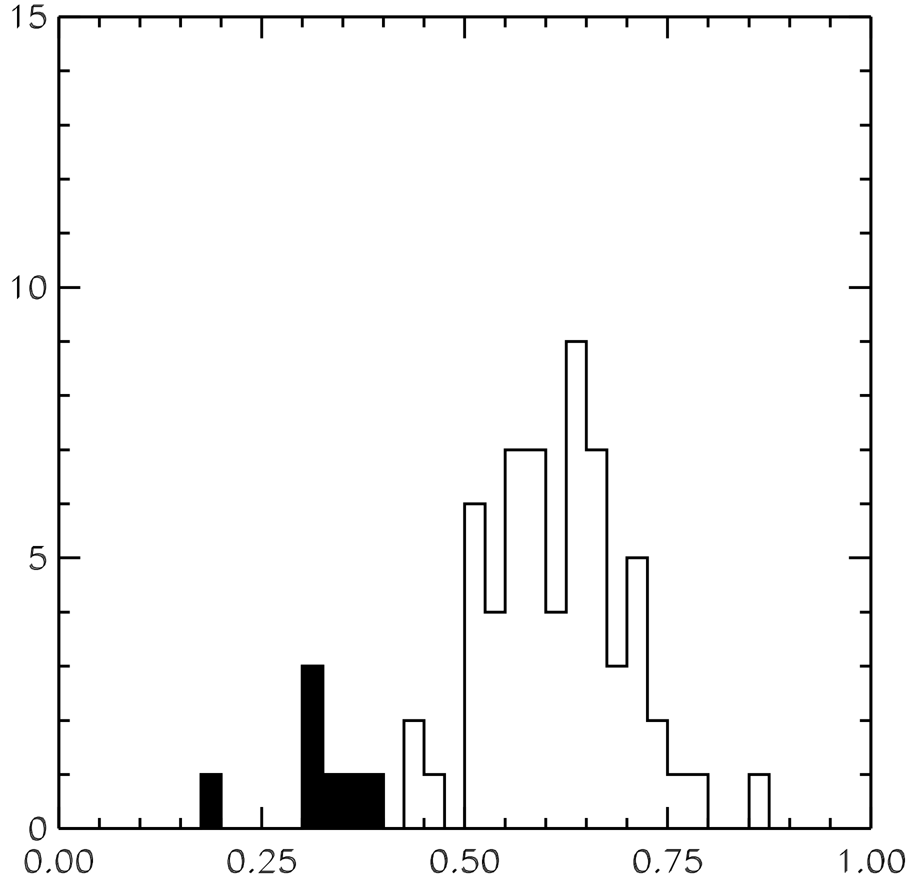

Figure 4.17: Distribution of the Fisher discriminant output for events in the signal region in the $h^+\pi^0$ mode.

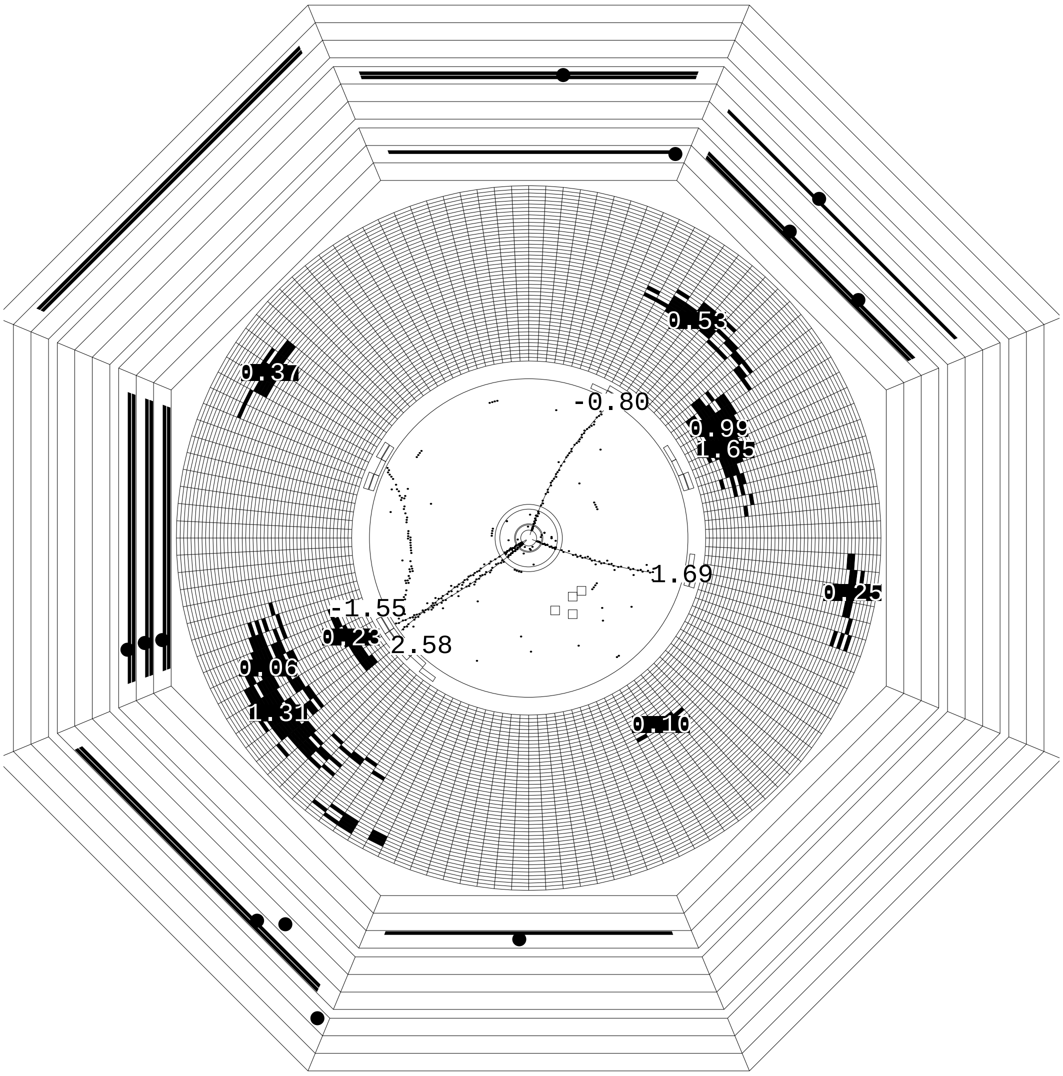

Figure 4.18: CLEO event display of the $h^+\pi^0$ event candidate where the other B meson was also reconstructed.

4.3.2 Systematic errors for the $h^+\pi^0$ analysis

The systematic errors of the ML fit are summarized in the Table 4.4.

Table 4.4: Change in the signal yield ($h^+\pi^0$) and upper limits for systematic variations of the fit parameters.

Mode	M_B^C	$\mathcal{F}^C$	Δ_E^S	M_B^S	$\mathcal{F}^S$	dE/dx	Total
$h^+\pi^0$	± 1.2	$+2.8/-1.4$	± 0.2	$+0.2/-0.4$	$+0.6/-0.8$	± 0.2	$+3.2/-2.0$
$K^+\pi^0$	0.5	1.3	0.5	0.2	0.4	0.8	1.7
$\pi^+\pi^0$	1.	1.8	0.2	0.2	0.6	0.8	2.3

As a final check of our result we varied all shapes simultaneously to minimize the overall signal yield. Under these "extreme" conditions the $h^+\pi^0$ signal still has 4.6σ significance.

4.3.3 Final results

We have measured the branching fraction of the decay $B^+ \to h^+\pi^0$, where h stands for K or π, to be $(1.6^{+0.6+0.3}_{-0.5-0.2} \pm 0.1) \times 10^{-5}$. We see evidence for the exclusive decays $B^+ \to K^+\pi^0$ (2.7σ) and $B^+ \to \pi^+\pi^0$ (2.8σ) and place 90% C.L. upper limits

- $Br(B^+ \to K^+\pi^0) < 1.6 \times 10^{-5}$
- $Br(B^+ \to \pi^+\pi^0) < 2.0 \times 10^{-5}$.

4.4 $B^+ \to \pi^+ K^0_S / K^+ K^0_S$

This analysis is very similar to the previous, with K^0_S replacing π^0 in the final state. 409 events enter the fit producing the following result:

- $N_{KK^0_S} = 0.6^{+3.8}_{-0.6}$, 0.2σ
- $N_{\pi K^0_S} = 9.2^{+4.3}_{-3.8}$, 3.2σ
- $N_{hK^0_S} = 9.8^{+4.5}_{-3.7}$, 4.4σ .

The corresponding likelihood contour plot is shown in Figure 4.19. The M_B and ΔE projection plots are in Figure 4.20.

We plot events used in the fit and satisfying $\mathcal{F} < 0.6$ in the $M_B - \Delta E$ plane. The resulting scatter plot is shown in Figure 4.21. The clustering of the events inside the signal box is quite evident.

We calculate branching fractions and upper limits (statistical errors only).

- $N^{UL}_{KK^0_S} = 6.9$
- $Br(B^+ \to \pi^+ K^0) = 2.3^{+1.1}_{-1.0} \times 10^{-5}$
- $Br(B^+ \to h^+ K^0) = 2.4^{+1.1}_{-0.9} \times 10^{-5}$.

4.4.1 Consistency checks

Fit without KK^0_S

The decay $B^+ \to K^+ K^0_S$ ($b \to dg$ transition) should be strongly suppressed with respect to $B^+ \to \pi^+ K^0_S$ ($b \to sg$ decay), as discussed in Chapter 1. In fact, in our

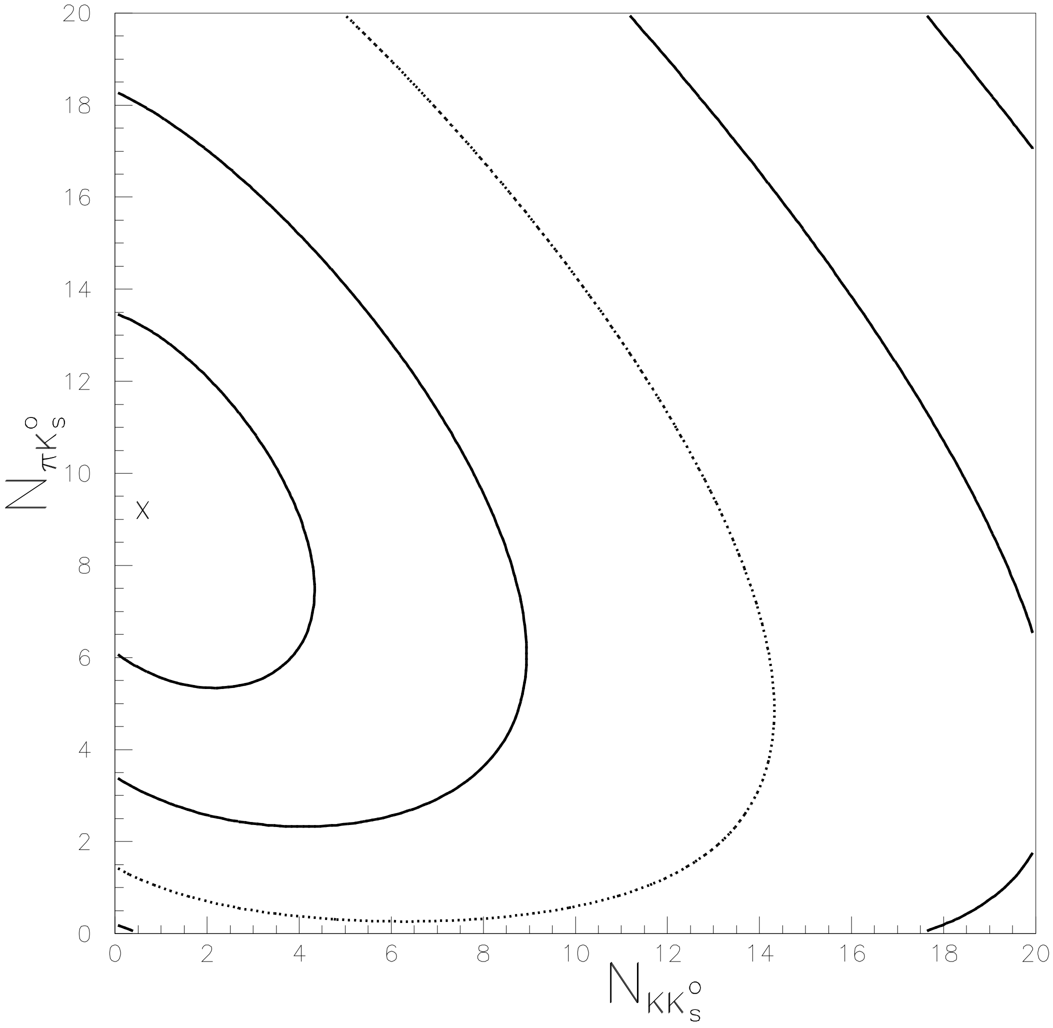

Figure 4.19: Likelihood contours for the fit to $N_{KK^0_S}$ and $N_{\pi K^0_S}$.

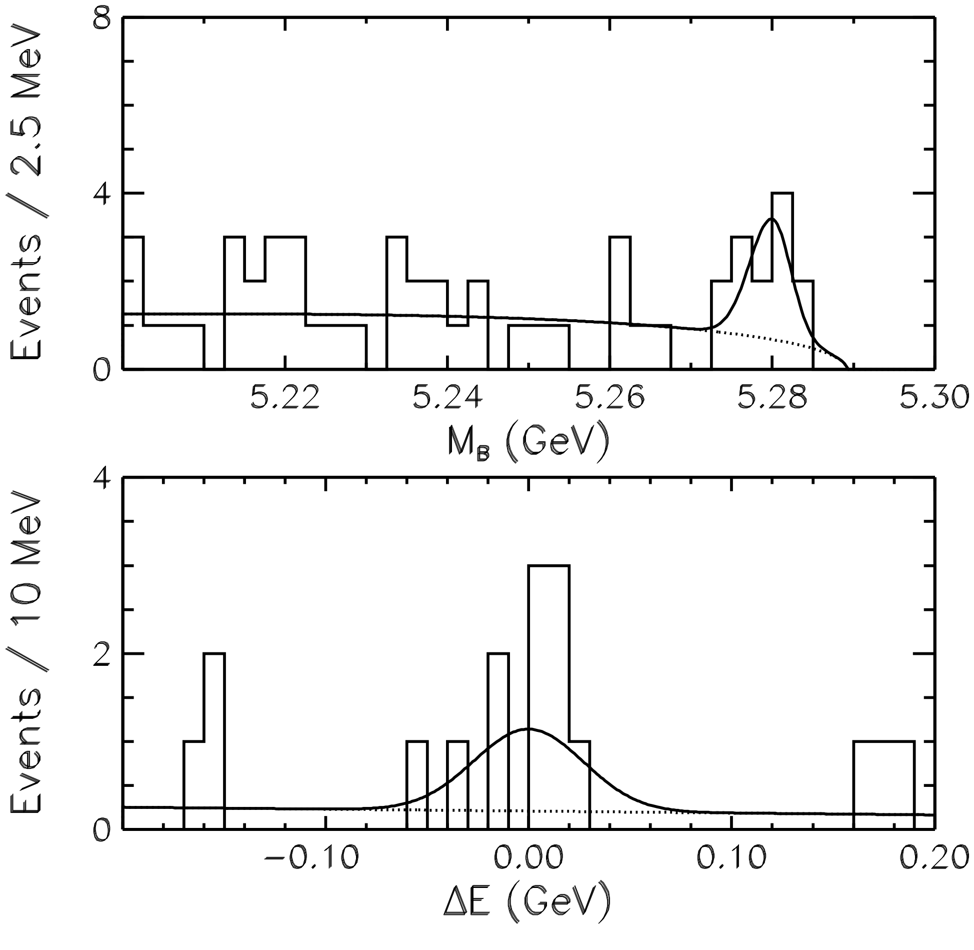

Figure 4.20: M_B and ΔE projections for the $h^+K_S^0$ mode.

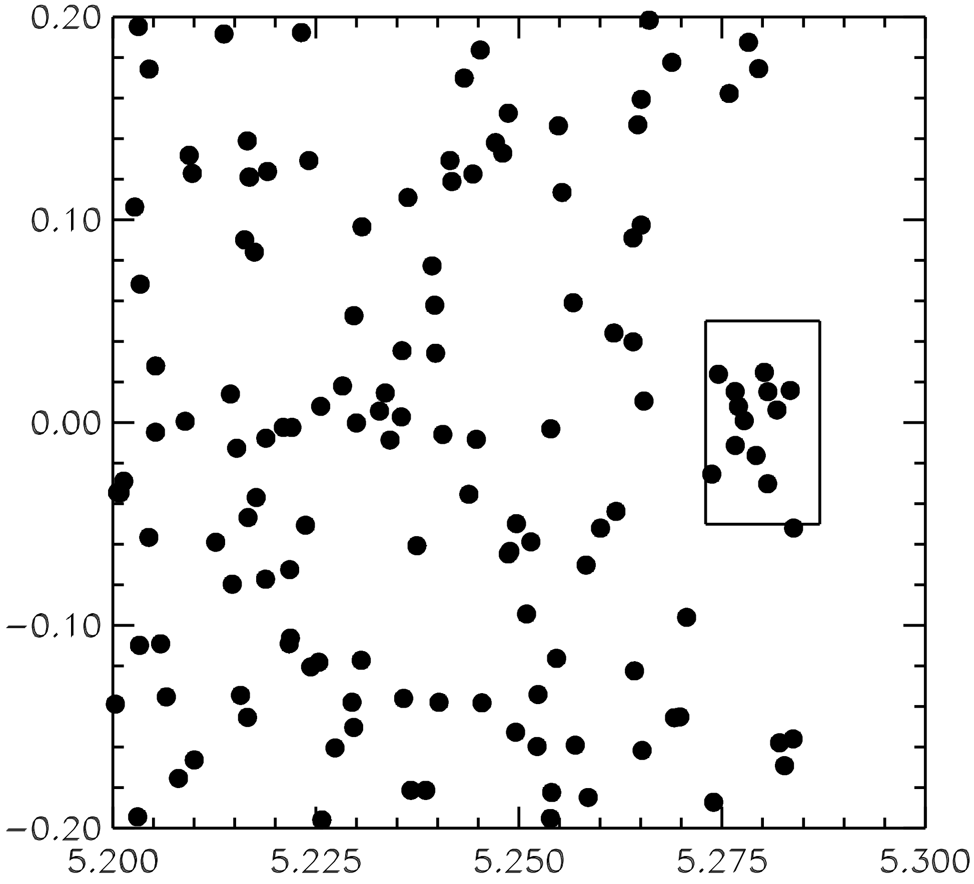

Figure 4.21: Events from the $h^+K^0_S$ analysis in the $M_B - \Delta E$ plane after the $\mathcal{F} < 0.6$ cut. The overlayed signal box corresponds to 2σ cuts on M_B and ΔE.

previous analysis [76] $K^+K^0_S$ was not even included in the fit. Excluding $K^+K^0_S$ signal fraction from the fit we find

- $N_{\pi K^0_S} = 9.5^{+4.1}_{-3.4}$, 4.4σ .

$|cos\Theta_{sph}|$ **dependence**

We varied the value of the $|\cos\Theta_{sph}|$ cut to check stability of the signal. For the $|cos\Theta_{sph}| < 0.7$ (242 events) we find

- $N_{KK^0_S} = 2.0^{+3.9}_{-2.0}$, 0.6σ
- $N_{\pi K^0_S} = 8.5^{+4.3}_{-3.6}$, 3.1σ
- $N_{hK^0_S} = 10.5^{+4.5}_{-3.7}$, 4.6σ .

Using the $|cos\Theta_{sph}| < 0.9$ cut (872 events) we obtain

- $N_{KK^0_S} = 0.8^{+4.4}_{-0.8}$, 0.2σ
- $N_{\pi K^0_S} = 9.3^{+4.7}_{-4.0}$, 3.0σ
- $N_{hK^0_S} = 10.1^{+5.0}_{-4.1}$, 4.0σ .

4.4.2 Systematic errors for the $h^+K^0_S$ analysis

Systematic errors due to the fitting procedure are listed in the Table 4.5.

Again we change all shapes to minimize the overall signal yield and find that the $h^+K^0_S$ ($\pi^+K^0_S$) signal still remains significant at the 3.9 (2.9) σ level.

Table 4.5: Change in the signal yield and upper limits for systematic variations of the fit parameters in the hK_S^0 analysis.

Mode	M_B^C	$\mathcal{F}^C$	Δ_E^S	M_B^S	$\mathcal{F}^S$	dE/dX	Total
$h^+K_S^0$	$^{+0.6}_{-0.7}$	$^{+0.5}_{-0.3}$	$^{+0.5}_{-0.4}$	±0.1	$^{+0.4}_{-0.5}$	±0.2	±1.0
$\pi^+K_S^0$	±0.2	±0.1	$^{+0.4}_{-0.6}$	$^{+0.1}_{-0.3}$	$^{+0.2}_{-0.3}$	$^{+1.1}_{-1.2}$	$+1.2/-1.4$
$K^+K_S^0$	0.2	0.1	0.6	–	0.1	0.4	0.7

4.4.3 Final results

We have measured the branching fraction of the decay $B^+ \to h^+K^0$, where h stands for K or π to be $(2.4^{+1.1+0.2}_{-0.9-0.2} \pm 0.2) \times 10^{-5}$. We find this decay to be dominated by the π^+K^0 final state which has statistical significance of 3.2σ when $K^+\bar{K}^0$ mode is allowed and 4.4σ when $K^+\bar{K}^0$ is excluded from the fit. Given that result is stable and $K^+\bar{K}^0$ mode is strongly suppressed we feel that π^+K^0 component of the signal is statistically significant on its own.

- $Br(B^+ \to K^+\bar{K}^0) < 2.1 \times 10^{-5}$
- $Br(B^+ \to \pi^+K^0) = (2.3^{+1.1+0.3}_{-1.0-0.3} \pm 0.2) \times 10^{-5}$
- $Br(B^+ \to h^+K^0) = (2.4^{+1.1+0.2}_{-0.9-0.2} \pm 0.2) \times 10^{-5}$.

4.5 $B^0 \to K_S^0\pi^0$ and $\pi^0\pi^0$

These final states are the simplest to analyze, since there is only one signal fraction to fit for. We therefore combine them in one section.

For the $K_S^0\pi^0$ mode we select 137 events for the ML fit. We find

- $N_{K_S^0\pi^0} = 4.1^{+3.1}_{-2.4}$ 2.2σ
- $N^{UL}_{K_S^0\pi^0} = 8.9$.

The contour plot in this case degenerates into a one-dimensional plot of the likelihood function, shown in Figure 4.22. M_B and ΔE projections are given in Figure 4.23. The scatter plot in the $M_B - \Delta E$ plane is shown in Figure 4.24. Again, the $\mathcal{F} < 0.6$ cut was made.

The $\pi^0\pi^0$ sample consists of 252 events and yields

- $N_{\pi^0\pi^0} = 2.7^{+2.7}_{-1.7}$, 2.4σ
- $N^{UL}_{\pi^0\pi^0} = 7.2$.

The likelihood function is shown in Figure 4.25. Figure 4.26 has M_B and ΔE projections. The scatter plot is shown in Figure 4.27.

4.5.1 Systematic errors for the $K_S^0\pi^0$ and $\pi^0\pi^0$ analyses

The summary of the systematic errors for these two modes is given in Table 4.6.

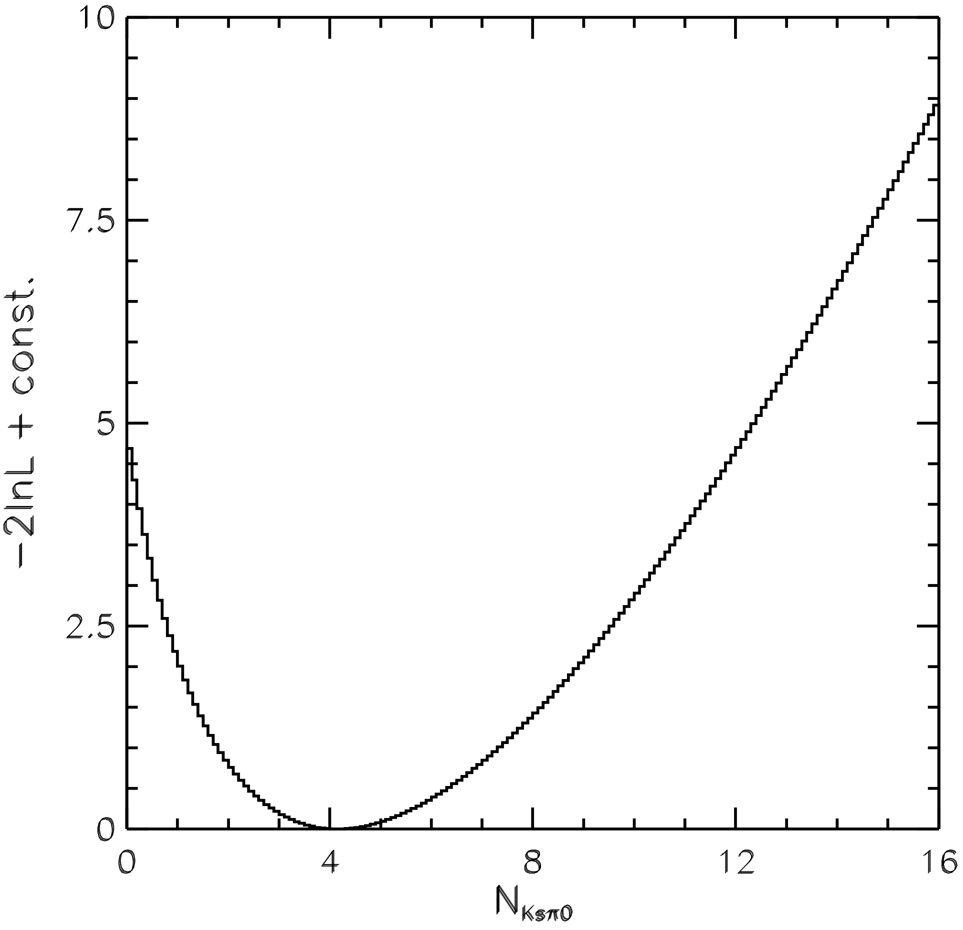

Figure 4.22: $-2ln\mathcal{L}$ plot for the $K_S^0\pi^0$ mode.

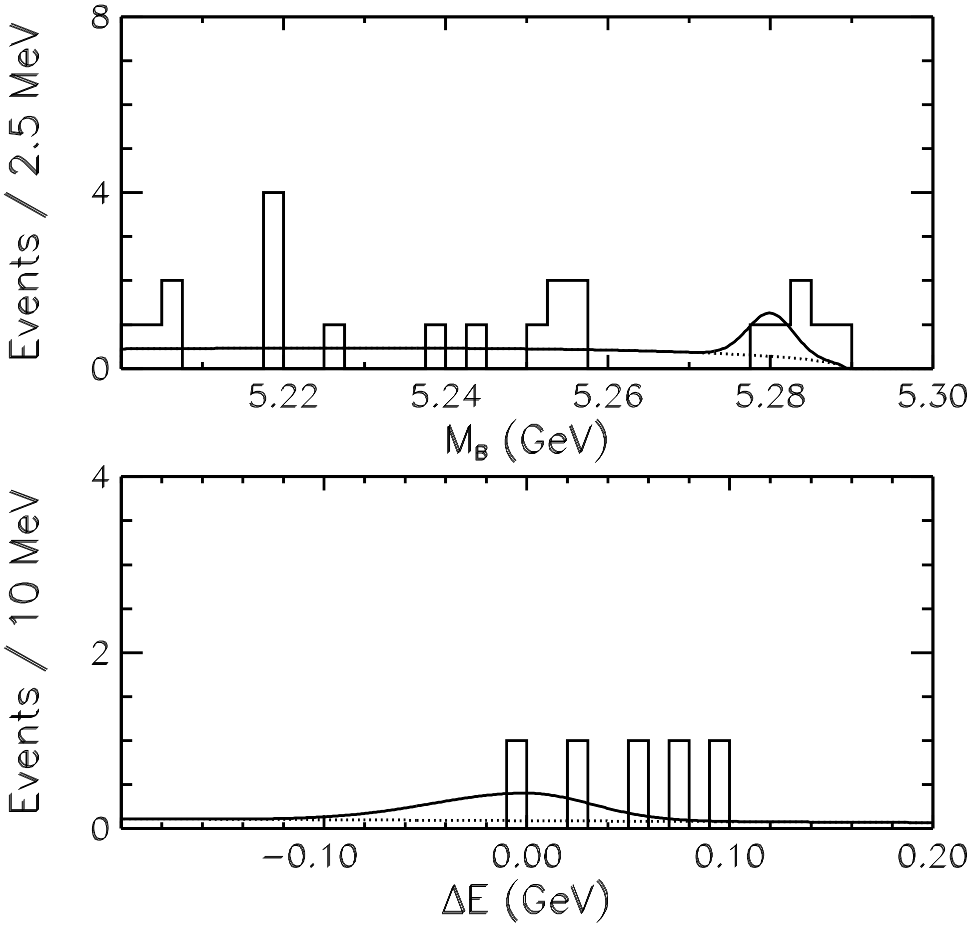

Figure 4.23: M_B and ΔE projections for the $K_S^0\pi^0$ mode.

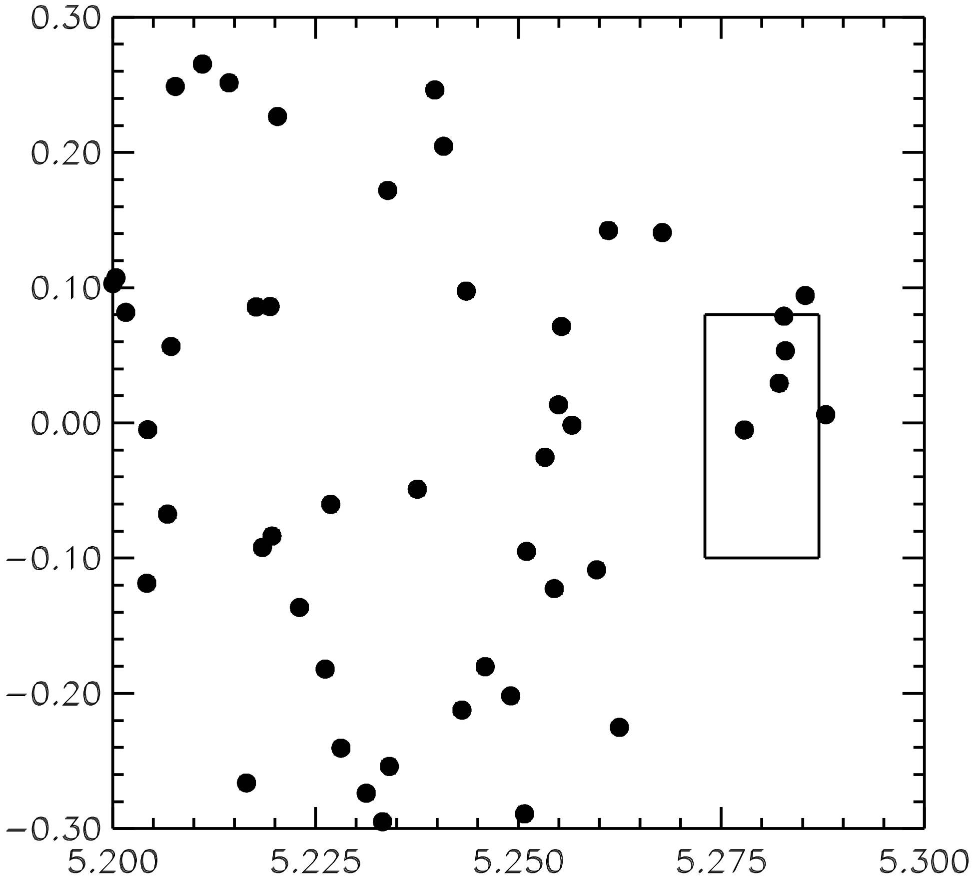

Figure 4.24: Scatter plot for the $K^0_S\pi^0$ mode after the $\mathcal{F} < 0.6$ cut.

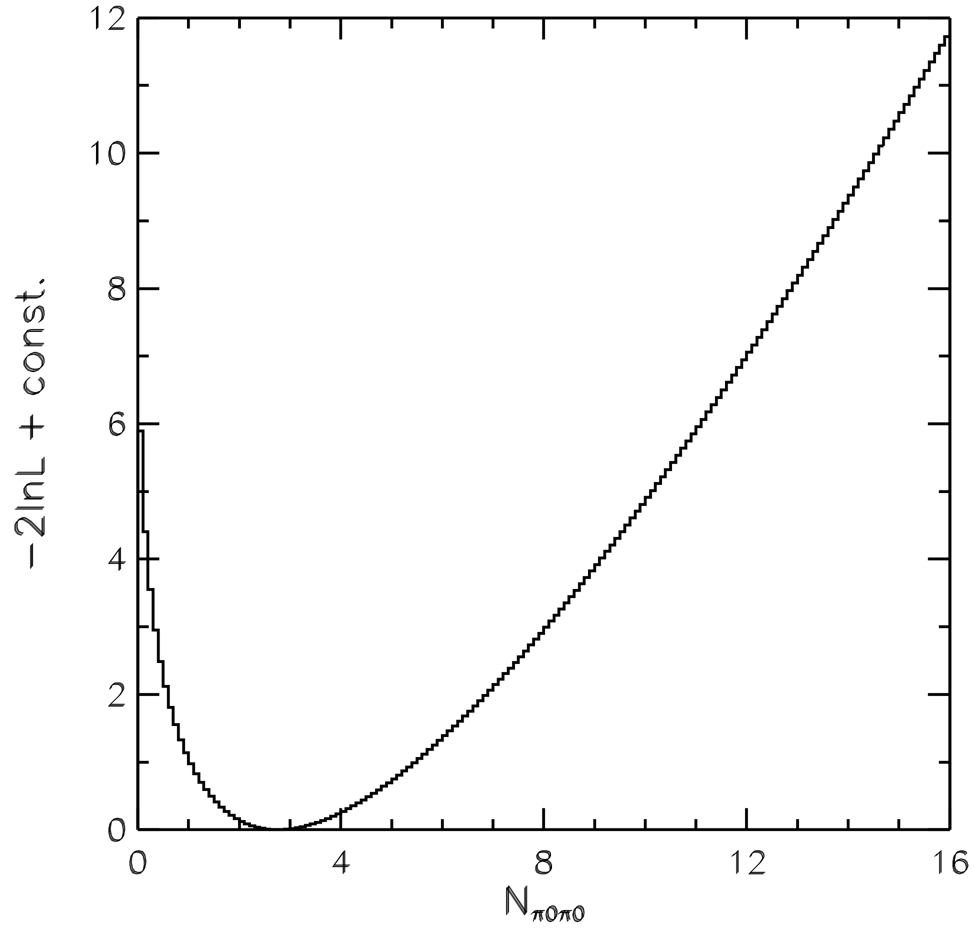

Figure 4.25: $-2ln\mathcal{L}$ plot for the $\pi^0\pi^0$ mode.

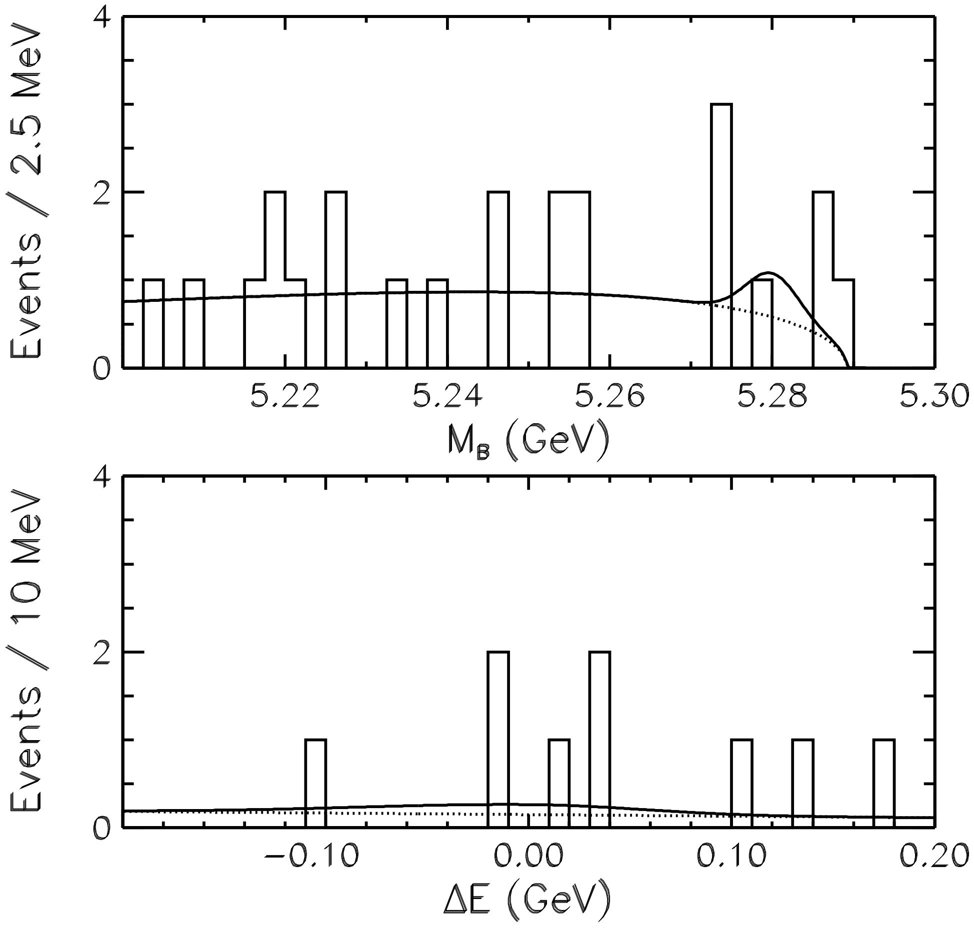

Figure 4.26: M_B and ΔE projections for the $\pi^0\pi^0$ mode.

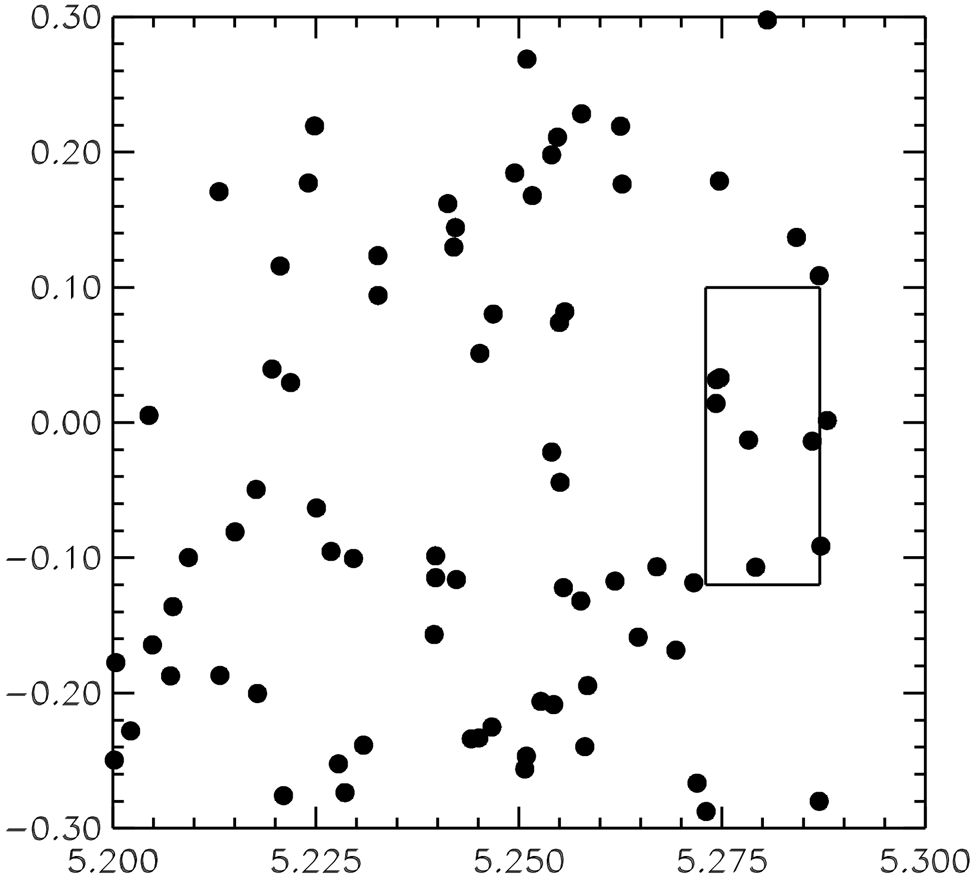

Figure 4.27: Scatter plot for the $\pi^0\pi^0$ mode after the $\mathcal{F} < 0.6$ cut.

Table 4.6: Change in upper limits for systematic variations of the fit parameters for the $K_S^0\pi^0$ and $\pi^0\pi^0$ analyses.

Mode	M_B^C	$\mathcal{F}^C$	Δ_E^S	M_B^S	$\mathcal{F}^S$	Total
$K_S^0\pi^0$	0.6	0.2	0.2	0.4	0.4	0.8
$\pi^0\pi^0$	0.5	0.4	0.1	0.2	0.2	0.7

4.5.2 Final results

After taking into account systematic errors, we calculate 90% C.L. upper limits for our decays:

- $Br(B^0 \to K^0\pi^0) < 4.1 \times 10^{-5}$
- $Br(B^0 \to \pi^0\pi^0) < 0.93 \times 10^{-5}$.

4.6 Conclusions

We have searched for rare two-body charmless decays of B meson into the $K\pi, \pi\pi$, and KK final states. We have made the first observation of the exclusive decays $B^0 \to K^+\pi^-$ and $B^+ \to \pi^+K^0$, as well as the semiexclusive decay $B^+ \to h^+\pi^0$, where h stands for K or π. We obtained new upper limits for the remaining modes. Our results are summarized in the Table 4.7. Let us briefly discuss our results and their implications.

Table 4.7: Summary of $B \to K\pi, \pi\pi$ results.

Mode	Eff (%)	Yield	Significance	Br (10^{-5}) This work	Br (10^{-5}) Old results [76]
$K^+\pi^-$	44	$21.6^{+6.8}_{-6.0}$	5.6σ	$1.5^{+0.5+0.1}_{-0.4-0.1} \pm 0.1$	< 1.7
$K^+\pi^0$	37	$8.7^{+5.3}_{-4.2}$	2.7σ	< 1.6	< 1.4
$K^0\pi^+$	12	$9.2^{+4.3}_{-3.8}$	3.2σ	$2.3^{+1.1+0.3}_{-1.0-0.3} \pm 0.2$	< 4.8
$K^0\pi^0$	8	$4.1^{+3.1}_{-2.4}$	2.2σ	< 4.1	< 4.0
$\pi^+\pi^-$	44	$9.9^{+6.8}_{-6.0}$	2.2σ	< 1.5	< 2.0
$\pi^+\pi^0$	37	$11.3^{+6.3}_{-5.2}$	2.8σ	< 2.0	< 1.7
$\pi^0\pi^0$	29	$2.7^{+2.7}_{-1.7}$	2.4σ	< 0.93	< 0.91
K^+K^-	44	$0.0^{+1.3}_{-0.0}$	0.0σ	< 0.43	< 0.4
$K^+\bar{K}^0$	12	$0.6^{+3.8}_{-0.6}$	0.2σ	< 2.1	-
$h^+\pi^-$	44	$31.5^{+8.4}_{-7.3}$	7.8σ	$2.2^{+0.6}_{-0.5}$	$1.8^{+0.6}_{-0.5}$
$h^+\pi^0$	37	$20.0^{+6.8}_{-5.9}$	5.5σ	$1.6^{+0.6+0.3}_{-0.5-0.2} \pm 0.1$	-
h^+K^0	12	$9.8^{+4.5}_{-4.0}$	4.4σ	$2.4^{+1.1+0.2}_{-0.9-0.2} \pm 0.2$	-

$K\pi$ vs. $\pi\pi$

From the observed signals in $B^0 \to K^+\pi^-$, $B^+ \to \pi^+K^0$ decay modes, as well as recent CLEO measurements of $B^+ \to \eta' K^+$, ωK^+ [83] we can conclude that $b \to sg$ penguins are likely to dominate over the $b \to u$ tree amplitude. We still have not observed statistically significant evidence for the exclusive B decay into the $\pi\pi$ final state. To illustrate the dominance of the $b \to sg$ transition we add together M_B and ΔE projection plots for all $K\pi$ modes. The resulting distributions are shown in Figure 4.28. The similar plot for the $\pi\pi$ modes is shown in Figure 4.29.

The large $b \to sg$ probably means that the $b \to dg$ penguin is also larger than previously thought. This makes the proposed extraction of α via $B^0 \to \pi^+\pi^-$ more complicated. First, the branching fraction for the $B^0 \to \pi^+\pi^-$ can be lower than expected - the central value of our measurement implies a central value of $B^0 \to \pi^+\pi^-$ branching fraction of $0.75^{+0.4}_{-0.35} \times 10^{-5}$. Also, the potential background from $B^0 \to K^+\pi^-$ becomes larger. Second, it appears that "penguin pollution" in this measurement cannot be neglected and has to be dealt with.

Large $B^+ \to \pi^+K^0$

As we discussed earlier, this decay mode provides a very good measurement of the $b \to sg$ penguin amplitude. Theoretical predictions for this decay were on the order of $0.9 - 1.2 \times 10^{-5}$, while we observe almost a factor of 2 larger value (although errors are quite large at the moment). It will be interesting to see whether it will stay at this level as more data become available.

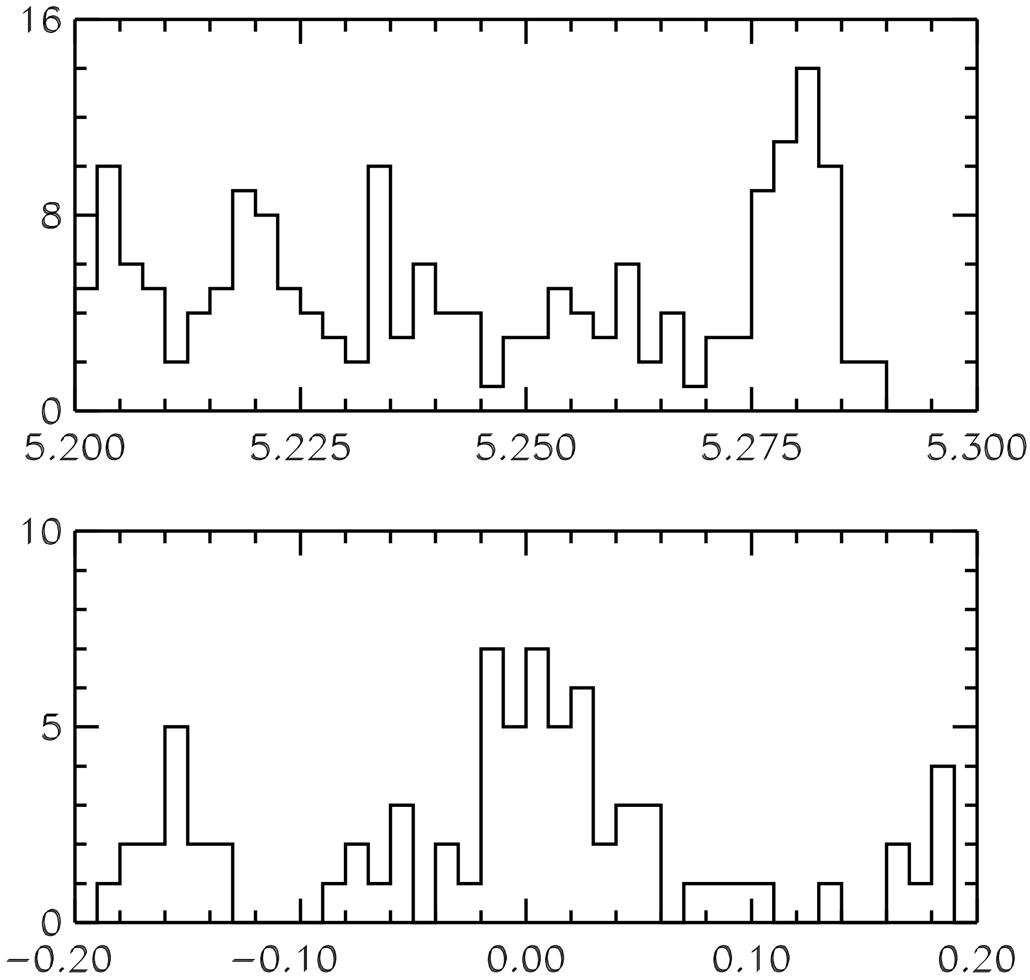

Figure 4.28: M_B (top) and ΔE (bottom) projections for the “inclusive” $B \to K\pi$ decays. ΔE was recalculated to be centered at 0 for all modes.

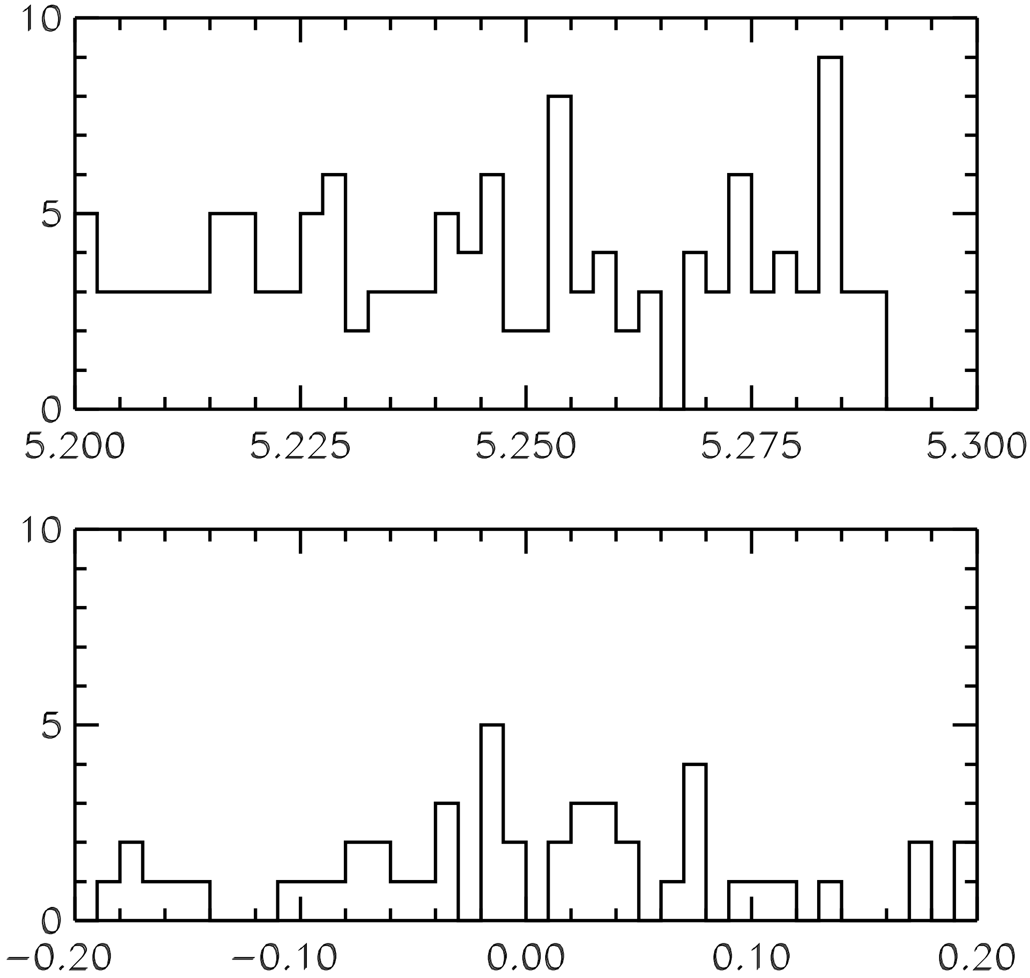

Figure 4.29: M_B (top) and ΔE (bottom) projections for the "inclusive" $B \to \pi\pi$ decays.

$B^0 \to \pi^0\pi^0$

While large $b \to dg$ penguins are bad news for the $B^0 \to \pi^+\pi^+$ decay, they can actually help to boost the $B^0 \to \pi^0\pi^0$ branching fraction. Remember that the dominant contributions to this decay are the color suppressed tree and the penguin. Our currently observed yield of 2.7 events is not very significant at the moment, but it will be an interesting surprise if the current central value for the branching fraction 2.8×10^{-6} will turn out to be true.

4.6.1 Recent theoretical results and ideas

Finally, we would like to describe some recent theoretical results and ideas, related to the experimental results presented in this work.

Ciuchini et al. [84] performed a new analysis of the exclusive charmless B decays. They used our results for $B^0 \to K^+\pi^-$ and $B^0 \to \pi^+\pi^-$ as a benchmark to constrain the parameter space of their model. Predicted branching fractions are listed in the Table 4.8.

Table 4.8: Predictions for some rare charmless B decays from Ciuchini *et al.* [84].

Mode	$B^0 \to \pi^+\pi^-$	$B^0 \to \pi^0\pi^0$	$B^+ \to \pi^+K^0$	$B^0 \to K^+\pi^-$
$Br \times 10^{-5}$	0.3-1.5	0.01-0.1	0.8-1.7	1.1-1.8

Fleischer and Mannel [85] proposed a very interesting way of constraining the angle γ of the unitarity triangle using only the combined branching fractions $B^{\pm} \to \pi^{\pm}K^0$ and $B \to K^{\pm}\pi^{\mp}$. The idea is to note that the $B^+ \to \pi^+K^0$ decay is dominated by the penguin amplitude, while $B^0 \to K^+\pi^-$ contains also the tree contribution

$$A(B^+ \to \pi^+K^0) = P' \tag{4.7}$$

$$A(B^0 \to K^+\pi^-) = -(P' + T') \tag{4.8}$$

The tree amplitude carries the nontrivial CKM phase γ. Computing the ratio of the charge-averaged branching fractions gives

$$R \equiv \frac{|A(B \to K^{\pm}\pi^{\mp})|}{|A(B^{\pm} \to \pi^{\pm}K^0)|} = 1 - 2r\cos\delta\cos\gamma + r^2 \ , \tag{4.9}$$

where $r = |T'|/|P'|$ and δ is the strong phase difference between tree and penguin amplitudes. We can rewrite the last equation in the form

$$\cos\delta\cos\gamma \equiv C = \frac{1-R}{2r} + \frac{r}{2} \ , \tag{4.10}$$

which implies the following allowed range for γ

$$0^\circ \leq \gamma \leq \gamma_0, \quad 180^\circ - \gamma_0 \leq \gamma \leq 180^\circ \ , \tag{4.11}$$

where $\gamma_0 = \cos^{-1}(|C|)$. This constraint is in principle complementary to the existing favored values of γ in the (ρ, η) plane [86]

$$40^\circ \leq \gamma \leq 140^\circ \ . \tag{4.12}$$

Figure 4.30 shows γ_0 dependence on the value of r for different values of R. One can conclude that the current central value of $R = 0.65$ implies $\gamma_0 < 54^\circ$. This

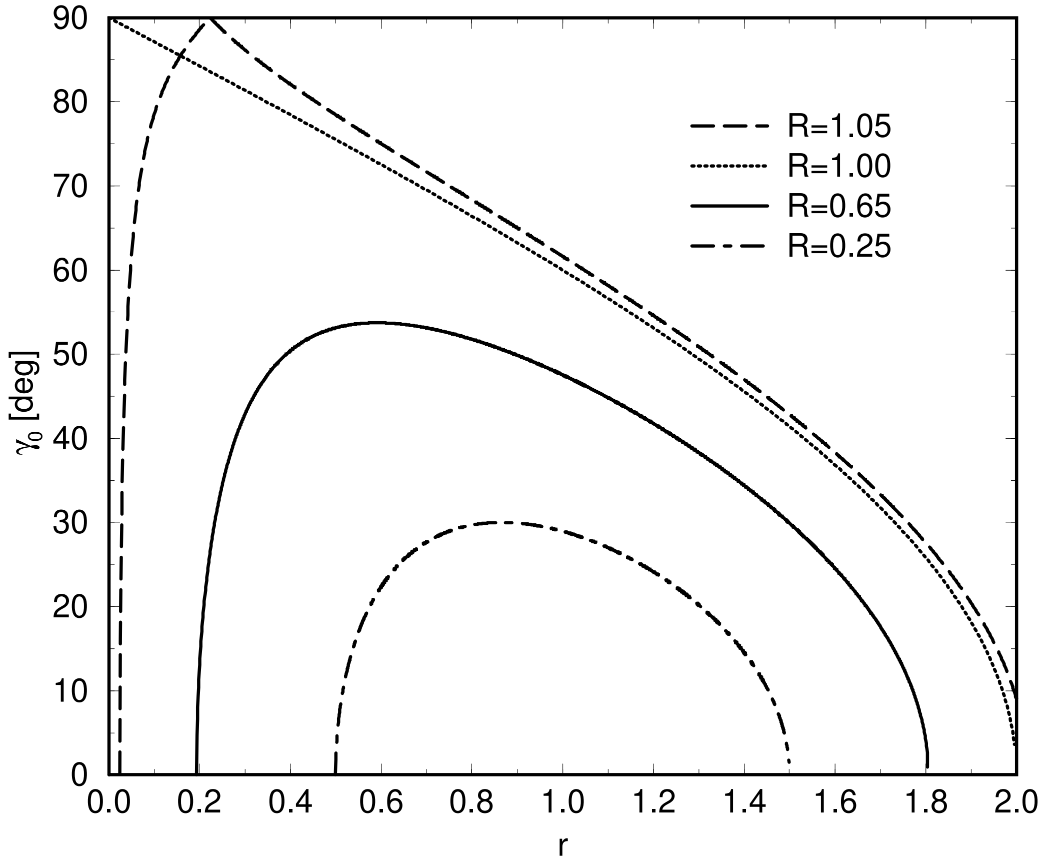

Figure 4.30: Dependence of γ_0 on R and r.

limit may become even more restrictive if we use the measured $Br(B^+ \to \pi^+ K^0) = 2.3 \times 10^{-5}$ and upper limit for the $Br(B^+ \to \pi^+\pi^0) < 2.0 \times 10^{-5}$ to place upper limit $r \leq 0.35$ with the help of

$$|T'| = \lambda \frac{f_K}{f_\pi} \sqrt{2} |A(B^\pm \to \pi^\pm \pi^0)| \ . \tag{4.13}$$

In this case $\gamma_0 < 48°$. To be realistic, the current 1σ experimental errors do not allow any restrictive limit on the γ_0. However, if we establish that R is indeed less than 1 and obtain a better estimate for r, this method can prove to be very promising for constraining the angle γ. Fleischer and Mannel even suggested that these measurements could put the Standard Model to a test and might indicate a window to “New Physics”. For more detailed discussion and possible “New Physics” scenarios see [87].

Ali and Greub recently performed a theoretical analysis of the charmless rare B decays [88], including those considered here. Their predictions are summarized in the Table 4.9. Since they quote branching fractions for several values of (ρ, η), and their result is dependent on the phenomenological factor $\xi = 1/N_c$ we've decided to list their predictions for $(\rho, \eta) = (0.05, 0.36)$ only. Ali and Greub also studied

Table 4.9: Predictions for some rare charmless B decays from Ali and Greub [88]. The range of values is due to variation in $\xi = 1/N_c$.

Mode	$\pi^+\pi^-$	$\pi^0\pi^0$	$\pi^+\pi^0$	π^+K^0	$K^+\pi^-$
$Br \times 10^{-5}$	0.6-1.2	0.06-0.3	0.3-1.2	0.9-2.2	1.0-2.2

the sensitivity of the R ratio to the values of (ρ, η). They found that it is not particularily sensitive to η, but has some sensitivity for ρ, as can be seen in Figure 4.31. Overall, Ali and Greub conclude that the SM can account for all current measurements of the rare charmless decays.

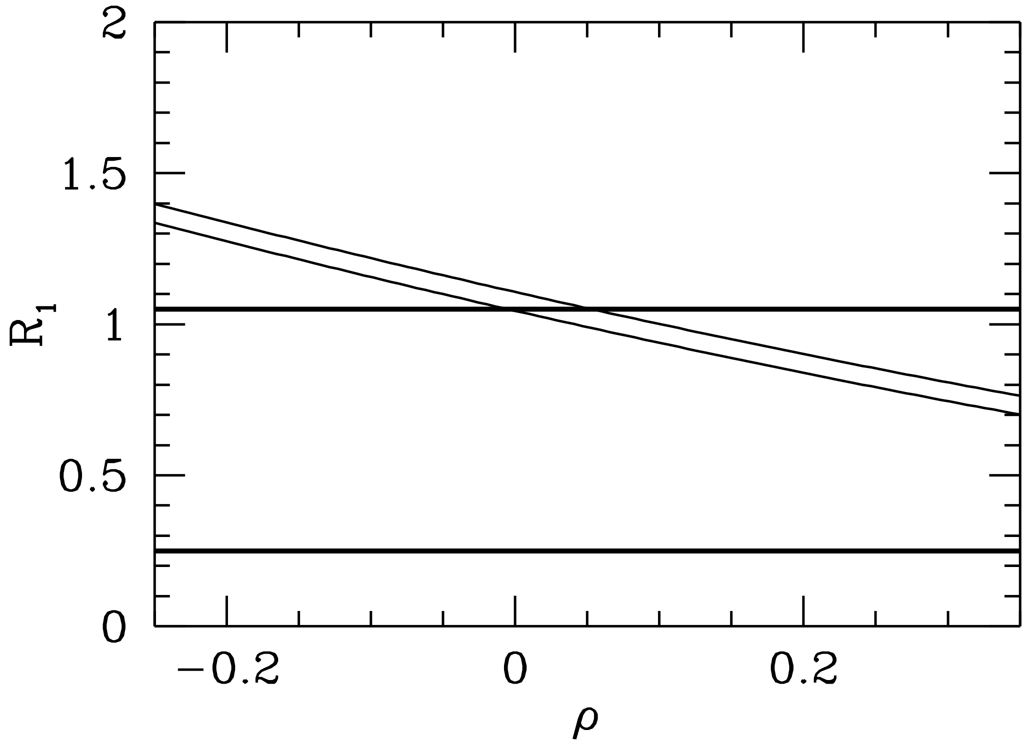

Figure 4.31: The ratio R as a function of the Wolfenstein parameter ρ, for $\eta = 0.25$ (lower curve) and $\eta = 0.52$ (upper curve) for $\xi = 0$. Solid horizontal lines correspond to our measurement (with 1σ errors).

With the addition of the CLEO II.V data, we can expect improved measurements for the existing signals and observation of new exclusive rare B decays in the immediate future. It is reasonable to assume that observation of the decays $B^+ \to K^+\pi^0,\ \pi^+\pi^0$ and $B^0 \to K^0\pi^0,\ \pi^+\pi^-$ will happen soon. As more and more results become available, we will be able to start putting limits on CP violation in B decays and will attempt to constrain the angle γ as well. The coming years promise to be very interesting for the rare B decays !

APPENDIX A

EVENT SELECTION CUTS

In this appendix we summarize all cuts used in this analysis for the future reference.

A.1 Global criteria

- KLASGL=10 or 11, or EVCLAS=10 (Hadronic class)
- $NTRKCD \geq N_{cand} + 3$ (Charged multiplicity)
- 4SNARROW: $5.285 < E_{beam} < 5.295$
- Datasets: 4s1 - 4sG .

A.2 Candidate selection

A.2.1 Tracks

- KINCD=0
- TNG $\geq$ 0 (TRKMAN cut)
- RESICD $\leq$ 500 μm (Average residuals)

- $|\text{Z0CD}\sin\theta| < 4$ cm (Impact parameter in $r - z$ plane)
- $|\text{DBCD}| < 1$ mm (Impact parameter in $r - \phi$ plane)
- Hit Fraction > 0.5 (Number of hits on tracks)
- IQALDI > 0 (dE/dx quality)
- $ZESCAPE = 0 \;\; (\; JBYT(KBITCD(ICD,\ 5),\ 28,\ 3) = 0\ )$
- $DREDGE = 0 \;\; (\; JBIT(KBITCD(ICD,\ 5),\ 3) = 0\ )$

A.2.2 Missed distance cuts for the h^+h^- analysis

- $|DBCD(1) + DBCD(2)| < 750\mu m$
- $|Z0CD(1)\sin\theta(1) - Z0CD(2)\sin\theta(2)| < 1$ cm

A.2.3 Lepton veto

- R2ELEC < 2
- DPTHMU < 5 or MUQUAL $\neq 0$

A.2.4 π^0 selection

- $|\cos\theta_{dec}| < 0.97$, θ_{dec} is the decay angle.
- $E9E25U(\gamma_1) + E9E25U(\gamma_2) \geq 1.83$
- $|M_{\gamma\gamma} - 0.135| \leq 0.02$

A.2.5 K_S^0 selection

- $CHISQ \leq 20$
- $RBMTX \geq 3$ mm
- $|M_{\pi\pi} - 0.49767| \leq 0.01$

A.3 Event shape

- $|\cos\Theta_{sph}| < 0.8$. Θ_{sph} is the angle between the major sphericity axis of the candidate and the major sphericity axis of the rest of the event.
- $|\cos\Theta_{can}| < 0.8$. Θ_{can} is the angle between the major sphericity axis of the candidate and the z-axis of the detector.

A.4 Filter for the $\cos\Theta_{sph}$ calculation.

A.4.1 Track filtering.

- $|PQCD| \leq 5.3$
- TNG ≥ 0
- RESICD ≤ 1 mm
- Hit Fraction ≥ 0.4
- DREDGE=0

and at least two of the following:

- RESICD $\leq 600\ \mu m$
- $|Z0CD| < 5$ cm
- $|DBCD| < 5$ mm

A.4.2 Shower filtering.

Accept all good showers with $E_\gamma > 50$ MeV not matched to the tracks. Reject showers with $E_\gamma < 100$ MeV near the candidate tracks (cosine of the angle between the track and shower axes larger than 0.97).

APPENDIX B

CHARACTERISTICS OF THE FULLY RECONSTRUCTED $B^+ \to H^+\pi^0$ EVENT.

In this appendix we provide detailed information of the fully reconstructed B^+B^- event.

Candidate side: most likely $B^+ \to \pi^+\pi^0$ event.

- $M_B = 5.278$ GeV, $\Delta E = -0.08 \;\; GeV/c^2$, $\mathcal{F} = 0.31$
- $\sigma_K = 1.89$, $\sigma_\pi = 0.29$
- $|\cos\Theta_{sph}| = 0.18$, $|\cos\Theta_B| = 0.7$
- $M_{\gamma\gamma} = 0.1357 \;\; GeV/c^2$, $E_{\gamma 1} = 1.635$ GeV, $E_{\gamma 2} = 0.985$ GeV

The "other" B:

- $D^0 \to K^-\pi^+$
  - $P_K = -0.801$ GeV/c, $P_\pi = 1.687$ GeV/c
  - $M_{D^0} = 1.860 \;\; GeV/c^2$
- $D^{*0} \to D^0\gamma$

  - $E_\gamma = 0.094$ GeV
  - $M_{D^{*0}} = 1.994 \;\; GeV/c^2$
  - $M_{D^{*0}} - M_{D^0} = 0.134 \;\; GeV/c^2$

- $B^- \to D^{*0}\mu^-\nu$
  - $P_\mu = -1.55$ GeV/c, $DPTHMU = 4.3$
  - $E_\nu = 0.997$ GeV, $P_\nu = 0.977$ GeV/c
  - $M_\nu^2 = 0.04 \;\; (GeV/c^2)^2$.

In order to check how reasonable these values are, we generated 4000 Monte Carlo B^+B^- events with B mesons decaying as described above. Resulting distributions are shown in Figure B.1, with arrows indicating the values we observed. We conclude that our event is quite typical in all aspects and most likely is indeed a true B^+B^- event.

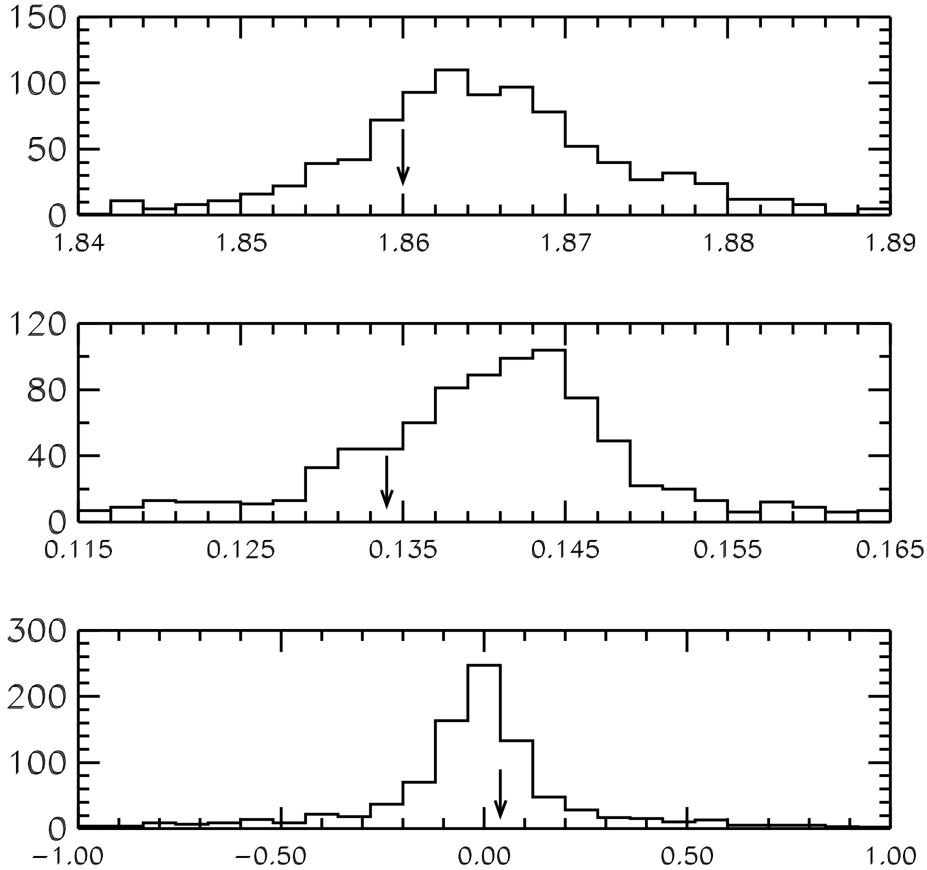

Figure B.1: Distributions of the M_{D^0} (top), $M_{D^{*0}} - M_{D^0}$ (middle), and M_ν^2 (bottom) for the decay $B \to D^{*0}\mu\nu$. Arrows indicate values of these variables for our fully reconstructed event.

References

[1] See for example C. Quigg, "Gauge Theories of the Strong, Weak, and Electromagnetic Interactions", Addison-Wesley, 1993; non-technical description of the Standard Model physics can be found in Steven Weinberg, "The Discovery of Subatomic Particles", W. H. Freeman 1984.

[2] J. H. Christenson, J. W. Cronin, V. L. Fitch and R. Turlay, *Phys. Rev. Lett.* **13**, (1964) 128.

[3] A. D. Sakharov, *ZhETF Pis. Red.* **5**, (1967) 32 (in Russian); *JETP Lett.* **5**, (1967) 24.

[4] A. V. Rubakov and M. E. Shaposhnikov *Phys.Usp.* **39**, (1996) 461.

[5] M. Kobayashi and K. Maskawa, *Prog. Theor. Phys.* **49**, (1973) 652.

[6] L. Wolfenstein, *Phys. Rev. Lett.* **51**, (1983) 1945.

[7] S. Stone, "Prospects for B-physics in the Next Decade", Syracuse University preprint, HEPSY 96-01 .

[8] A. J. Buras and R. Fleischer, "Quark Mixing, CP Violation and Rare Decays After the Top Quark Discovery", in "Heavy Flavors", eds. A. J. Buras and M. Lindner, 2nd ed., World Scientific, to be published.

[9] R. M. Barnett *et al.*, *Phys. Rev.* **D54**, (1996) 1.

[10] I. I. Bigi, V. A. Khoze, N. G. Uraltsev, and A. I. Sanda, in "CP violation" edited by C. Jarlskog, World Scientific (1989).

[11] M. Bander, D. Silverman, and A. Soni, *Phys. Rev. Lett.* **43**, (1979) 242.

[12] L.-L. Chau and H.-Y. Cheng, *Phys. Rev. Lett.* **59**, (1987) 958; N. Deshpande and J. Trampetic, *Phys. Rev.* **D41**, (1990) 2926; J. M. Gerard and W. S. Hou, *Phys. Rev.* **D43**, (1991) 2909; H. Simma, G. Eilam and D. Wyler, *Nucl. Phys.* **B352**, (1991) 367.

[13] M. Gronau, *Phys.Rev.Lett* **63**, (1989) 1451.

[14] M. Gronau, O. F. Hernandez, D. London, and J. L. Rosner, *Phys. Rev.* **D50**, (1994) 4529.

[15] M. Gronau, O. F. Hernandez, D. London, and J. L. Rosner, *Phys. Rev.* **D52**, (1995) 6374.

[16] R. Fleischer, *Int. J. Mod. Phys.* **A12**, (1997) 2459.

[17] K. G. Wilson, *Phys. Rev.* **179**, (1969) 1499.

[18] G. Buchalla, A. Buras, and M. Lautenbacher, *Rev. Mod. Phys.* **68**, (1996) 1125.

[19] J. Bjorken, *Nucl. Phys.* **B11** (Proc. Suppl.), (1989) 325.

[20] A. Abada *et al.*, *Nucl.Phys.* **417**, (1994) 675.

[21] J. Flynn, *Nucl.Phys.* **53** Proc. Suppl., (1997) 168.

[22] V. M. Belyaev, A. Khodjamirian, and R. Ruckl, *Z. Phys.* **C60**, (1993) 349; V.M.Belyaev, V. M. Braun, A. Khodjamirian, and R. Ruckl, *Phys.Rev* **D51,** (1995) 6177.

[23] A. Deandrea, N. Di Bartolomeo, R. Gatto, and G. Nardulli, *Phys.Lett.* **B318**, (1993) 549.

[24] R. Casalbuoni, A. Deandrea, N. Di Bartolomeo, F. Feriglio, R. Gatto, and G. Nardulli, *Phys.Rept.* **281**, (1997) 145.

[25] M. Bauer, B. Stech, and M. Wirbel, *Z.Phys.* **C34**, (1987) 103.

[26] N. Isgur, D. Skora, B. Grinstein, and M. B. Wise, *Phys.Rev.* **D39**, (1989) 799.

[27] M. Neubert, V. Rieckert, B. Stech, and Q. P. Xu, in *"Heavy Flavors"*, eds. A. J. Buras and M. Lindner, World Scientific, Singapore (1992).

[28] D. Ebert, R. N. Faustov, and V. O. Galkin, *Phys.Rev.* **D56**, (1997) 312.

[29] D. Du and L. Guo, *Z. Phys.* **C75**, (1997) 9.

[30] L.-L. Chau, H.-Y. Cheng, W. K. Sze, H. Yao, and B. Tseng, *Phys. Rev.* **D43**, (1991) 2176.

[31] N. G. Deshpande and J. Trampetic, *Phys. Rev.* **D41**, (1990) 895.

[32] G. Kramer, W. F. Palmer, and H. Simma, *Phys. Rev.* **D52**, (1995) 6411.

[33] M. Gronau and D. London, *Phys. Rev. Lett.* **65**, (1990) 3381.

[34] J. P. Silva and L. Wolfenstein, *Phys. Rev.* **D49**, (1994) 1151; R. Aleksan *et al.*, *Phys.Lett.* **B356**, (1995) 95; C. Hamzaoui and Z. Z. Xing, *Phys. Lett.* **B360**, (1995) 131; F. DeJongh and P. Sphicas, *Phys. Rev.* **D53**, (1996) 4930; R. Fleischer and T. Mannel, *Phys. Lett.* **B397**, (1997) 269.

[35] D. Zeppenfeld, *Z.Phys. C* **8**, (1981) 77.

[36] M. Gronau, J. L. Rosner, and D. London, *Phys. Rev. Lett* **73**, (1994) 21; M. Gronau, O. F. Hernandez, D. London, and J. L. Rosner, *Phys. Rev. D* **50**, (1994) 4529.

[37] M. Gronau, O. F. Hernandez, D. London, and J. L. Rosner, *Phys. Rev.* **D52**,(1995) 6356.

[38] N. G. Deshpande and X.-G. He, *Phys. Rev. Lett.* **74**, (1995) 26.

[39] N. G. Deshpande and X.-G. He, *Phys. Rev. Lett.* **75**, (1995) 3064.

[40] A. S. Dighe, *Phys. Rev.* **D54**, (1996) 2067. A. S. Dighe, M. Gronau, and J. L. Rosner, *Phys. Lett.* **B367**, (1996) 357.

[41] R. Fleischer, *Phys. Lett.* **B365**, (1996) 399.

[42] R. Fleischer, *Phys. Lett.* **B321**, (1994) 259.

[43] G.'t Hooft, *Phys. Rev. Lett* **37**, (1976) 8.

[44] R. D. Peccei and H. Quinn, *Phys. Rev. Lett* **38**, (1977) 1440; *Phys. Rev.* **D16**, (1977) 1791.

[45] P. H. Frampton and S. L. Glashow, *Phys. Rev.* **D55**, (1997) 1691 and references therein.

[46] M. Gronau and D. London, *Phys. Rev.* **D55**, (1997) 2845.

[47] Y. Grossman, Y. Nir, and R. Rattazzi, “CP Violation Beyond the Standard Model”, in “Heavy Flavors” , eds. A. J. Buras and M. Lindner, 2nd ed., World Scientific, to be published.

[48] Y. Kubota *et al.*, *Nucl.Instr. and.Meth.* **A320**, (1992) 66.

[49] W. R. Leo, "Techniques for Nuclear And Particle Physics Experiments", Springer-Verlag, 1992.

[50] F. Sauli , "Principles of Operation of Multiwire Proportional and Drift Chambers", CERN Report No. CERN 77-09(unpublished).

[51] F. Würthwein and J. P. Alexander, "Momentum Resolution at 2.6 GeV/c", CBX 93-39(unpublished).

[52] C. Bebek *et al.*, *Nucl. Instr. Meth.* **A302**, (1991) 261.

[53] D. Bortoletto *et al.*, *Nucl. Instr. Meth.* **A320**, (1992) 114.

[54] Hamamatsu Photonics, K.K., 1126 Ichino-Cho, Hamamatsu City, 435 Japan.

[55] H. Becker *et al.*, *IEEE Trans. Nucl. Sci.* **38**, (1988) 246; W. Buttler *et al.*, *Nucl. Inst. and Meth.* **A315**, (1992) 420.

[56] J. P. Alexander *et al.*, *Nucl. Inst. and Meth.* **A337**, (1993) 171.

[57] Denis J. Dumas, "Retractable Radiation Shields for the CLEO II Silicon Vertex Detector", CBX 95-106 (unpublished).

[58] D. Miller *et al.* (CLEO Collaboration), "The CLEO III Detector: Design and Physics Goals", Cornell Report CLNS 94-1277.

[59] D. Boutigny *et al.* (BaBar Collaboration), "Technical Design Report", SLAC Report SLAC-R-95-457, 1995.

[60] M. T. Cheng *et al.* (BELLE Collaboration), "Technical Design Report", KEK Report 95-1, 1995.

[61] "The CDF II Detector Technical Design Report", FERMILAB-Pub-96/390-E .

[62] "The D0 Upgrade", FERMILAB-Pub-96/357-E .

[63] P. Krizan *et al.* (HERA-B Collaboration), *Nucl. Instr. Meth.* **A351**, (1994) 111.

[64] S. Stone, "The BTeV program", Syracuse University preprint HEPSY 97-01.

[65] W. W. Armstrong *et al.* (ATLAS), "Technical Proposal", CERN/LHCC/94-43, 1994.

[66] G. L. Bayatian *et al.* (CMS), "Technical Proposal", CERN/LHCC/94-38, 1994.

[67] K. Krisebom *et al.* (LHC-B), "Letter of Intent", CERN/LHCC/95-5, 1995.

[68] CLEO starts new data set every time detector pole tips are opened for the maintenance.

[69] S. Roberts, L. Gibbons, and E. Thorndike, "Trkman the Next Generation: the quest for track quality", CBX 96-103 (unpublished).

[70] C. O'Grady, "Electron identification with CLEO II", CBX 91-82 (unpublished).

[71] B. K.Heltsley, "Muon identification efficiencies", CBX 92-117 (unpublished).

[72] F. Würthwein and J. P. Alexander, "Details on continuum suppressions as used in the analysis of $B^0 \to K^+\pi^-$ and $B^0 \to \pi^+\pi^-$", CBX 93-40 (unpublished).

[73] F. Würthwein, Cornell University PhD Thesis, 1995 (unpublished).

[74] G. Fox and S. Wolfram, *Phys. Rev. Lett.* **41**, (1978) 1581.

[75] R. A. Fisher, *Annals of Eugenics* **7**, (1936) 179.

[76] D. M. Asner *et al.*, *Phys. Rev.* **D53**, (1996) 1039.

[77] We use CLEOG, a GEANT based computer program, to simulate CLEO II events. We thank the CERN computer staff for maintaining the GEANT detector simulation code (version 3.14, CERN DD/EE/84-1, R. Brun *et al.*)

[78] K. Lingel, "Search for $B \to K^*\pi,\ K\rho,\ \pi\rho$", CBX 94-48; "Search for rare hadronic B decays in modes which include K_S^0", CBX 95-24 (unpublished).

[79] J. Rodriguez, "B momenta and the beam energy shifts", CBX 97-45 (unpublished).

[80] A. G. Frodesen, O. Skeggestad, and H. Tøfte, *Probability and Statistics in Particle Physics*, Universitetsforlaget Bergen-Oslo-Tromsø, 1979.

[81] M. Battle *et al.*, *Phys. Rev. Lett.***71**, (1993) 3922.

[82] We would like to thank Abi Soffer for providing us with the sample of tagged D^0 decays.

[83] J. Smith (CLEO collaboration), talk presented at the 1997 Aspen Winter Conference on Particle Physics, Aspen, Colorado, 1997.

[84] M. Ciuchini *et al.*, “Charming penguins in B decays”, CERN preprint CERN-TH/97-30.

[85] R. Fleischer and T. Mannel, “Constraining the CKM angle γ and penguin contributions through combined $B \to \pi K$ branching ratios”, Univ. of Karlsruhe preprint TTP 97-17.

[86] A. Ali and D. London, *Nucl.Phys.Proc.Suppl.* **54A** (1997) 297.

[87] R. Fleischer and T. Mannel, “New physics in penguin dominated $B \to \pi K$ decays”, Univ. of Karlsruhe preprint TTP 97-22.

[88] A. Ali and C. Greub, “An analysis of two-body non-leptonic B decays involving light mesons in the Standard Model”, DESY preprint DESY 97-126.